Development of a System for Optical Atom Chip Experiments with Rubidium

Alexander Bunting

PhD

Physics
University of York

February 2019

Abstract

This work reports on the development and characterisation of a double MOT system designed for cold atom experiments with Rubidium. The whole system was designed and constructed from scratch and is capable of trapping atoms in a crossed optical dipole trap. During the course of this project, a new compact LVIS chamber was designed and characterised, which provides a high atom flux of atoms with low velocities and without the need to heat the Rubidium reservoir. The vacuum chamber also includes a fused silica prism, the surface of which is suspended above the trapped atoms. This enables future studies into trapping atoms close to a dielectric surface, which is an area of study that is crucial for the realisation of all-optical atom chips. The optical dipole trap was successfully demonstrated, however, no BEC was produced as of yet. Reasons for this are discussed. Part II of this thesis aims to revise results obtained from observations of matter-wave propagation in a continuous distributed Bragg splitter based on optical waveguides in free-space and provides additional explanations for the observed dynamics, as well as discussing ongoing and future improvements to its operation.

Declaration

I hereby declare that except where specific reference is made to the work of others, the contents of this dissertation are original and have not been submitted in whole or in part for consideration for any other degree or qualification in this, or any other university. This dissertation is my own work and contains nothing which is the outcome of work done in collaboration with others, except as specified in the text and Acknowledgements. This dissertation contains fewer than 65,000 words including appendices, bibliography, footnotes, tables and equations and has fewer than 150 figures.

Alexander Bunting
February 2019

Acknowledgements

Firstly, I would like to thank my supervisor Prof. Yuri Ovchinnikov for his guidance during my PhD, as well as his patience and never-ending stream of ideas. I would like to express my gratitude to my academic supervisor, Prof. Tim Spiller, for providing me with support and advice throughout my PhD journey.

I would also like to thank my family, Iolanta, Anastasia, Katy, Frederick and Richard. Their continuous encouragement and emotional support has been invaluable every step of the way. For their unwavering belief in me I am immensely grateful.

I would like to thank Jerry and Catriona, for supporting me during my thesis write-up, providing me with an endeless supply of McVitie's biscuits and frequent reminders to practice the saxophone.

Lastly, I would like to thank my partner Steph - I simply couldn't have done this without you. Thank you for being there when I needed you most.

Table of contents

List of figures

List of tables

PART I

TOWARDS ALL OPTICAL ATOM CHIPS

Chapter 1

Introduction

The development of laser cooling and trapping of atoms in the 1970s [1–3] helped to propel the study of single isolated systems from the theoretical to the experimental realm. Cooling atoms down to micro-kelvin temperatures suppresses the classical noise and allows us to physically observe many quantum phenomena. Laser cooling gave rise to the next generation of atomic clocks [4, 5] and high precision tests of fundamental physics [6–8]. The field continues to thrive with many studies ranging from attempts to trap macroscopic molecules [9] to quantum inertial sensing for navigation and quantum information processing (QIP) for quantum computing [10, 11].

One area of particular interest is the realisation of compact inertial navigation devices based on atom interferometry [12]. Combined with the high accuracy of atomic clocks, cold atom-based inertial navigation systems have the potential to significantly outperform current classical and laser-based devices [13]. Accurate and reliable inertial sensing is highly desired for both civic and military applications.

Interferometry is a measurement technique which exploits the interference of waves. In a typical interferometer, a wave is first split into two parts using some sort of splitter. Then, the two resulting waves are made to travel along two different paths. Finally, the two waves are recombined and superimposed. If the two partial waves have different relative phases when superimposed, an interference pattern is observed. The relative phase difference can be determined from the interference pattern and can be used to quantify whatever mechanism resulted in the phase shift. Depending on their configuration, interferometers can be used to

measure displacements, rotations, changes of refraction index, and any other effect that can result in the relative change of the optical path lengths in the interferometer.

In 1887, during the famous "Failed Experiment", A. Michelson and E. Morley intended to detect the flow of “Luminiferous Aether” using interferometry [14]. While failing its intended purpose, the Michelson interferometer provided the opportunity to accurately measure distances by observation of interference fringes. The basic geometry of a Michelson interferometer is illustrated in Figure 1.1(a). A large-scale Michelson interferometer was used in 2017 to detect gravitational waves for the first time [15].

In 1891, L. Mach and L. Zehnder proposed a different interferometer similar to Michelson, but where each separated light path is traversed only once [16, 17], as presented in Figure 1.1(b). This means the two interfering waves travel in parallel routes instead of orthogonal, making the Mach-Zehnder interferometer more robust against environmental perturbations [18]. The enclosed area produced by the optical paths makes it well suited for measuring rotations and topological phase shifts [19]. Additionally, the physical separation of input and output ports is favourable for applications that incorporate circuits or networks. Mach-Zehnder interferometers are used primarily in optical communications for modulation of phase and amplitude of light.

In 1913, still fuelled by the pursuit of the Luminiferous Aether, Georges Sagnac performed an experiment using his own interferometer and observed the correlation of angular velocity and phase shift [20], see Figure 1.1(c). The Sagnac interferometer has seen a great deal of progress following the invention of lasers and optical fibres, which led to the development of the ring laser gyroscope (RLG) [21] and subsequently the fibre optic gyroscope (FOG) [22]. The RLG and FOG based gyroscopes are used primarily as a part of an inertial navigation system (INS) on board of aircraft, spacecraft as well as ships and submarines. While these devices offer high accuracies they are subject to small bias drift errors which compound over time. Therefore applications requiring long periods of operation require integration with external navigation systems like GPS. Atom interferometers, by comparison, have negligible bias drift, making them favourable in GPS-denied environments.

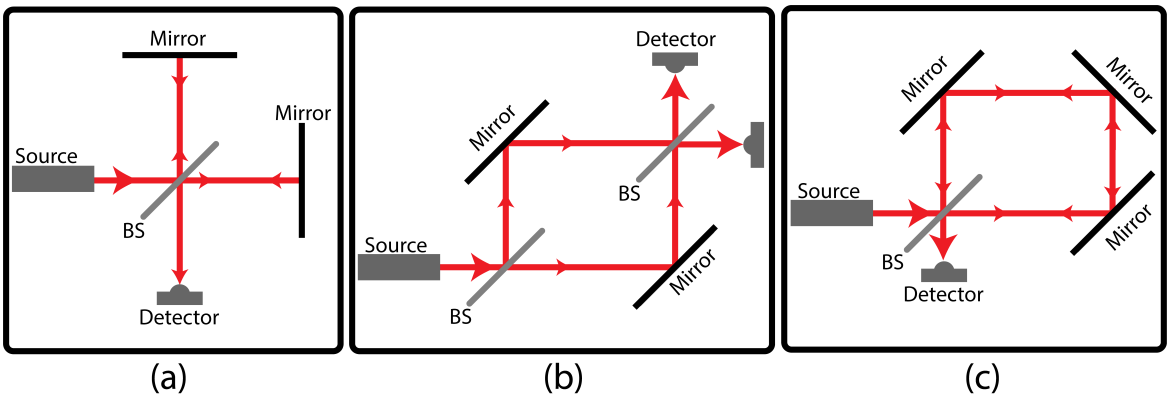

Fig. 1.1 Interferometer Geometries. (a) Michelson Interferometer. (b) Mach-Zehnder Interferometer (c) Sagnac interferometer

1.1 Atom Interferometry

One of the obvious advantages of using cold atoms instead of light sources for inertial measurements is their high sensitivity to inertial forces, due to the fact that atoms have mass. This can be demonstrated by considering the following. For a gyroscope utilising the Sagnac effect [23] to measure a rotation rate, Ω, the phase shift between the two paths of the interferometer can be written as:

$$\Phi_{Sagnac} = \frac{4\pi E}{hc^2}\mathbf{A}\cdot\Omega, \tag{1.1}$$

where A is the area enclosed by the Sagnac loop and E is the energy of the particle. $E = \hbar\omega$ for photons and $E = Mc^2$ for particles with rest mass M. Therefore, gyroscopes based on matter-wave interferometers will have a larger Sagnac phase by a factor of $Mc^2/\hbar\omega$. When comparing Rubidium atoms and visible light the scale factor of the phase shift is in the order of 10^{10}. Light-based interferometers, such as FOGs, counteract the reduced sensitivity by sending light around the loop many times using optical fibres and by increasing the path length. Naturally, lasers also provide much higher fluxes than typical atom beam sources.

Atom and light-based interferometers can operate no better than the standard quantum limit (SQL). SQL dictates that the sensitivity scales as $1/\sqrt{N}$, where N is the number of detected atoms (or photons). This presents a problem, as typical atom sources have low fluxes, especially compared to photons. There is great interest in creating atom interferometers that

can bypass the SQL. This can be achieved by generating squeezed atomic states by mapping the quantum state of squeezed light to an atomic field [24]. Interferometer sensitivity can be improved to scale as $1/N$, which is the absolute limit imposed by the Heisenberg uncertainty principle, by preparing quantum correlations between the atoms.

The first modern atom interferometers were demonstrated in 1991. One, was analogous to Young's double-slit experiment [25], while the other atom interferometer was based on three mechanical gratings [26]. Later experiments utilised laser beam pulses in order to split and deflect the matter waves [27, 28].

Light-pulse atom interferometers have been demonstrated to have high sensitivity in measurements of acceleration [29, 30] and rotation [31, 32], as well as the combination of the two in three-dimensions [33]. Cold atom inertial sensors can achieve higher long term stabilities and sensitivities than their electro-mechanical and laser-based counterparts [34], however, their dynamic range is significantly limited. Since the output of an atom interferometer is periodic, accelerations large enough to result in a shift higher than π rad from the central fringe of the output signal spoil the measurement. To overcome this issue, hybridisation techniques [35] are employed to combine conventional accelerometers with and atom interferometers and extend their dynamic range. Typically, a MEMS accelerometer is used to measure the acceleration of the reference mirror to re-centre the output of the atom interferometer to the central fringe, post-measurement [36] and in real-time [37]. This extends the dynamic range of cold atom interferometer to that of the conventional sensors.

However, cold atom interferometers typically require the use of bulky ultra-high vacuum (UHV) chambers, multiple lasers and numerous electronics. This means that most proposed devices are bulky and sensitive to environmental effects such as vibrations and temperature fluctuations. While some cold atom absolute gravimeters have already been made available commercially [38], the majority of the technological potential is still confined to the lab.

Atom interferometry with free-falling atoms is significantly limited by short interrogation times (typically several 100 μs). Interferometers based on atomic fountains increase these interrogation times, but only by a factor of $\sim$4. Interferometry with atoms guided in magnetic or optical waveguides [39] aims to increase the interrogation times and sensitivities by suspending the atoms against gravity and accurately controlling their paths.

1.2 Atom Chips

Atom chips are micro-fabricated devices with integrated optical, magnetic and electric structures that are used to trap and manipulate cold atoms close to the chip surface. Atom chips allow of precise control of the geometry of the atom interferometer. For atom chips utilising magnetic waveguides the close proximity of atoms to the magnetic fields allows for the application of much stronger forces.

Atom chips have been used to produce Bose-Einstein Condensates (BECs) in the lab [40, 41], and recently in microgravity in space [42]. In on-chip atom interferometry atoms can be guided either using magnetic [43] or optical waveguides [44]. In magnetic chip interferometers, the matterwaves are split and recombined using current-induced magnetic fields. However, interactions between atoms and wires have proved common and detrimental to coherent manipulation [45].

1.2.1 Towards All-Optical Atom Chips

Coherent splitting of BECs using all-optical means has been demonstrated using linear optical waveguides [44] and Y-shaped waveguides with a small opening angle [46]. All-optical configurations present several advantages over their magnetic counterparts. Optical dipole traps are able to trap atoms in magnetically insensitive states, which is beneficial for improving robustness from decoherence due to environmental magnetic fields. The "smoothness" of magnetic waveguide potentials is limited by the roughness of the nano-wires which results in decoherence [45, 47, 48]. Guiding potentials in optical waveguides are "smooth" and the absence of detrimental atom-wire interactions is of great benefit to coherent manipulation of matterwaves. Additionally, atom chips based on optical waveguides dissipate less power than atom chips based on magnetic nanowires.

An important stepping stone towards the realisation of all-optical atom chips is the ability to trap atoms close to the surface of the chip using all-optical means, as this would allow for precise control of the initial position of the matter-wave and subsequent loading of surface waveguides. Gravito-optical surface traps (GOSTs) have been experimentally demonstrated [49–51] to effectively suspend atoms above the dielectric surface of a prism using the combination of gravity combined with the repulsive potential produced by the evanescent field of a blue detuned optical dipole beam. A bi-chromatic evanescent wave (EW) surface

trap was proposed in 1991 [52], based on the evanescent fields of two lasers beams totally internally reflected at a dielectric surface. Just like in the case of optical dipole traps, far detuned EWs can produce either an attractive or repulsive dipole potential depending on the sign of the detuning of the light with respect to the atomic resonance. The advantage of this type of surface trap is that atoms can be trapped regardless of the direction of gravity, as well as in microgravity. The basic concept of a bi-chromatic EW surface trap is illustrated in Figure 1.2. The blue detuned evanescent field provides a repulsive potential that holds the atoms away from the attractive Van der Waals forces of the surface, while the red-detuned field provides the confining potential. In theory, atoms could be trapped on the order of $\lambda/2\pi n$ away from the surface, although this strongly depends on the surface smoothness. The bi-chromatic evanescent-wave trap was successfully demonstrated in 2002 with caesium atoms trapped $\sim$200 μm above the surface of a prism [53].

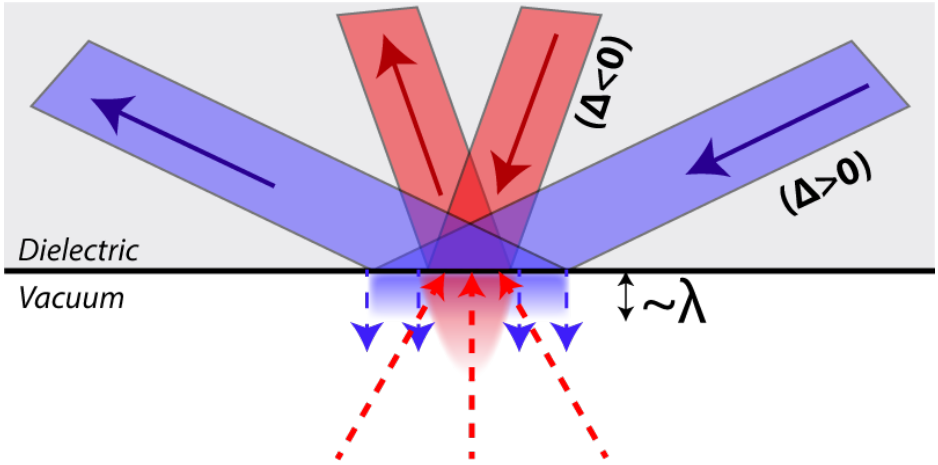

Fig. 1.2 The trapping potential is formed by the attractive red detuned potential and repulsive blue detuned potential. Note the different penetration depths of both evanescent fields, set by the incident angle.

Bi-chromatic EW fields have been the basis of several proposals for optical waveguides above a dielectric surface [54, 55]. However, experimental demonstration of such waveguides is still in the early stages. The work presented in this thesis is motivated by the realisation of all-optical waveguides for atoms at the surface of an atom chip based on bi-chromatic evanescent fields. The first step towards this is the realisation of effective loading and trapping of a bi-chromatic EW surface trap. In this thesis we describe the development of a new cold-atom apparatus at NPL, utilising a super-polished fused silica prism for the demonstration and further development of a bi-chromatic EW surface. Theoretical work is currently underway in the atom interferometry group at NPL to further study the practical

realisation of integrated all-optical waveguides based on bi-chromatic EW fields [56]. It is intended that in the near future the system developed during the course of this PhD will be used as a platform to experimentally demonstrate such waveguides.

Recently, a novel way to coherently and continuously deflect atoms by a large and arbitrary angle has been proposed [57]. The distributed Bragg splitter based on the crossing of two interfering optical waveguides promises coherent control and splitting of guided matterwaves. The atoms initially propagating in one linear waveguide are either transmitted, or deflected by the lattice formed at the crossing region and directed into the second waveguide which intercepts the first at an angle 2α. The basic scheme is illustrated in Figure 1.3. Such a splitter could potentially be used in the realisation of coherent atom circuits for area enclosed inertial sensors [44] as well as in the emerging field of atomtronics [58, 59]. The first experimental demonstration of this splitter has been conducted in our group at NPL, using a BEC of ^{87}Rb atoms and all-optical waveguides produced by free-space optical dipole beams [60]. While the current free-space demonstration offers a valuable proof of concept, the operation of the splitter could be substantially improved by realising it using all-optical atom chips based on optical waveguides. In Part II of this thesis, we discuss in detail the behaviour of atoms in this splitter and the limitations of the current free-space configuration.

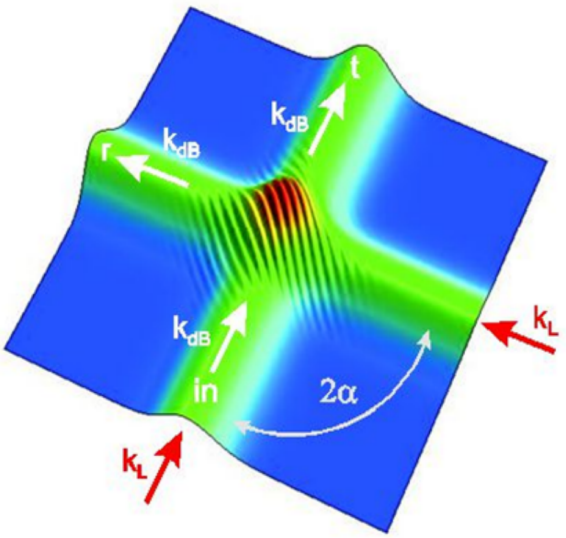

Fig. 1.3 Beam splitter for matter waves based on waveguide diffraction of crossed interfering beams. Atoms are diffracted at the optical lattice in the crossing region of the beams and are split between the two waveguides. k_L and k_{dB} are the wavevectors of the laser beams and the matter-wave respectively. The waveguides into which the atoms are either reflected or transmitted are labelled respectively with an r and t. The illustration is taken from [57]

Figure 1.4(a) illustrates a basic concept for a potential scheme for recreation of the distributed Bragg splitter from [60] but using planar waveguides instead of free-space beams. BEC atoms will be produced by all-optical means at some distance away from the prism surface, and subsequently transported and loaded into the bi-chromatic evanescent wave surface trap. Here, the surface trap is formed using free-space beams totally internally reflected at the surface of the prism, which produces a bi-chromatic EW surface trap. This set-up assumes the production of an all-optical BEC using free-space means above the chip surface. The BEC can then be transported to the surface trap using all-optical means [61] Here, the optical waveguides can be realised on a chip using integrated structures, such as Bragg coupling gratings mounted on a Si_3N_4 guiding layer. The optical waveguides can be formed by the coupling of light into the microfabricated channel of a substrate at the surface of the prism using tapered or Bragg couplers [62]. Atoms are confined and guided by the resulting evanescent fields. Figures1.2(b) illustrates how a Mach-Zehnder geometry could be realised using curved optical waveguides based on bi-chromatic beams and the aforementioned distributed Bragg splitter.

1.3 Thesis Structure

This thesis is divided into two parts. Part I focuses on the ongoing development of a new cold-atom apparatus designed to cool and trap atoms in a crossed optical dipole trap, with the intention of transporting the atoms to a surface trap formed at the dielectric surface of a fused silica prism. This would lay the groundwork for future demonstrations of integrated optical waveguides on a substrate of the prism. Since this is a novel endeavour at NPL, the apparatus needed to be designed and built from the ground up. This involved designing and constructing the ultra-high vacuum system, as well as the optical systems for laser cooling in a MOT and all-optical production of BEC using optical dipole traps (ODTs).

A total of three UHV chambers were constructed. A brand custom LVIS chamber was designed to achieve a robust yet compact design, which additionally yielded a high flux of atoms without the need to apply heat to the Rubidium reservoir. This is a desirable feature for experiments requiring ultra-high vacuum, as well as applications that have a limited budget on power consumption. The chamber features a super polished fused silica prism, which is positioned approximately 8mm above the centre of the MOT. An optical dipole trap was successfully formed below the prism, using a single beam and crossed beam configurations.

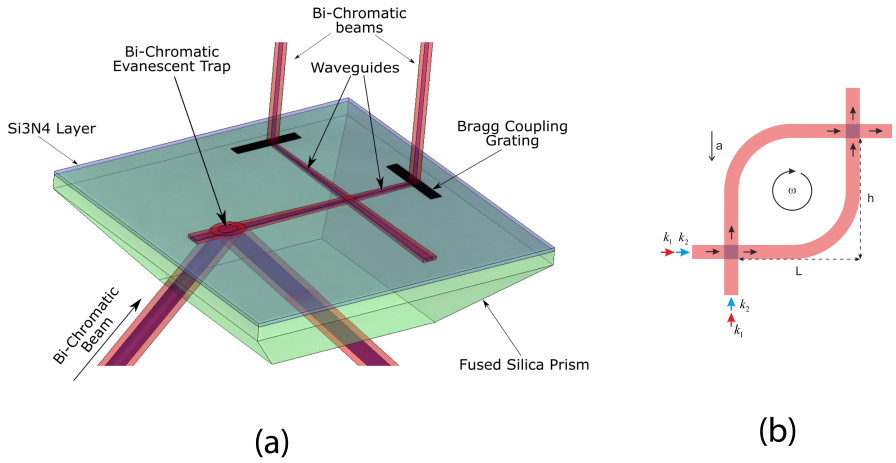

Fig. 1.4 (a) Concept of a basic scheme for realising the distributed Bragg splitter using planar EW waveguides on the surface of a chip. The BEC atoms are produced at some point above the prism and transported to the surface of the chip using all-optical methods. The BEC can be loaded into a bi-chromatic surface trap, realised by the total internal reflection of two free-space beams. The surface trap can then be relaxed and the atoms loaded into the bichromatic waveguide which corresponds to the input of the matter wave-splitter, like in Figure 1.3. Bi-chromatic beams are coupled into integrated channels in the silicon nitride layer, producing planar EW waveguide potentials above the surface. (b) Concept for a Mach-Zehnder interferometer geometry using curved bi-chromatic EW waveguides. $k1$ and $k2$ refer to the wave-vector of the red-detuned and blue-detuned optical dipole beams. The matterwaves are split and recombined using two distributed Bragg splitters.

The intent will be to use the prism in conjunction with two far-off resonance laser beams, to produce a bi-chromatic evanescent wave trap, capable of trapping BEC atoms above the surface of the prism. Additionally, a focusing lens mounted on an air-bearing stage will be used to move the focus of the dipole trap upwards towards the surface of the prism, in order to load the atoms into the evanescent wave trap.

Chapter 2 discusses the theory of laser cooling as well as optical dipole trapping. Chapters 3-5 cover the practical aspects of building the experiment. Chapter 3 reports on the design and construction of the UHV chambers while Chapter 4 details the optical systems and lasers. Chapter 5 discusses the common experimental techniques that were used, as well as a few novel techniques that were developed during the course of this experiment. Chapters 6 and 7 present the results which consist of the characterisation of the improved LVIS chamber and the optical dipole trap. Finally, Chapter 8 discusses the results and provides the next steps towards trapping the atoms close to the surface of the prism. The technical drawings of our LVIS chamber design can be found in the Appendix.

Part II of the thesis is based on the work conducted on the realisation of the continuous waveguide Bragg splitter produced by Gaussian laser beams in free space. The details and results of this experiment can be found in [60], as well as the PhD thesis of Richard Moore [63]. In Part II of this thesis, we provide additional discussion of results and provide additional explanations for the atom dynamics observed in the splitter. Finally, we discuss the improvements that should be implemented in order to improve the performance of the splitter.

Chapter 2

Laser Cooling and Trapping

Laser cooling refers to a set of techniques by which gaseous atoms are slowed down (and therefore cooled) using laser fields. The idea of laser cooling relies on the fundamental concept that the temperature of a gas is directly proportional to the kinetic energy of the molecules within the gas. This can be expressed using equipartition, by equating the average kinetic energy of the molecules $\langle E_k \rangle$ to their thermal energy:

$$\langle E_k \rangle = \frac{1}{2} m \langle v^2 \rangle = \frac{3}{2} k_B T. \tag{2.1}$$

For a gas at room temperature the velocity profile will follow a Boltzmann distribution with the average velocity of the atoms being $\sim$300 ms^{-1}. Laser cooling techniques are routinely used to slow down the motion of gaseous atoms and cool them to near absolute zero effective temperatures.

This chapter covers some of the core concepts of laser cooling and trapping of neutral atoms, which are relevant throughout this thesis. There are two primary forces which are exploited for the purpose of slowing atomic motion and the manipulation of atoms: the scattering force, which results from the momentum transfer when an atom absorbs radiation and the optical dipole force, which manifests when an atom interacts with detuned light. There is also a third force, the polarisation gradient force, which is a hybrid of the spontaneous scattering and dipole forces.

In the following sections, we discuss how these forces are utilised in atom cooling, as well as describe the theory of magneto-optical traps (MOTs) and optical dipole traps (ODTs).

2.1 Doppler Cooling

We start by considering a simple atom-photon interaction. Consider a laser beam incident on an atom, with velocity v, moving in the opposite direction to the stream of photons. When the atom absorbs a photon, it is excited from the ground to the excited state, and the combined velocity becomes $v-(\hbar k)/m$. After a short time, the atom will decay back to the ground state, emitting the photon in a random direction. Since the direction is random, the momentum contribution of the emitted photon averages to zero. This is illustrated in Figure 2.1 below. With each absorption and re-emission, the atom receives a small momentum kick in the direction of the laser beam, effectively decelerating the atom.

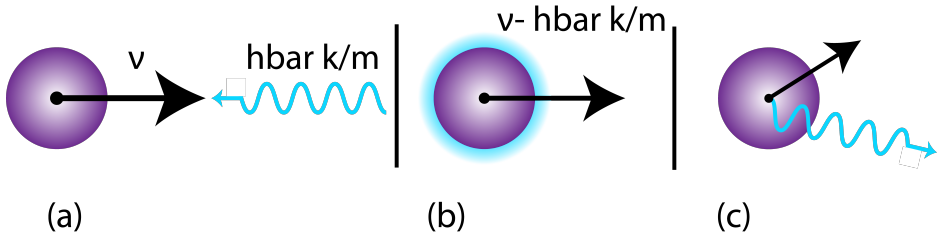

Fig. 2.1 Two-Level Atom Photon Interaction. (a) Photon is moving towards atom. (b) Photon is absorbed by atom, exciting it to a higher state. (c) Photon is emitted in random direction, atom velocity has been reduced.

Atoms in a real gas move in random directions. To slow down these atoms, we can employ a configuration of three counter-propagating pairs of laser beams aligned along the three directional axes. For efficient absorption of photons, the incident light has to be in resonance with the atomic transition. However, an atom moving towards a photon will perceive the wavelength of the photon as shorter, or blue-shifted. The opposite is true for an atom moving in the same direction as the photons. This means that our laser can only significantly affect the sample of atoms with a specific velocity, selected by the detuning of the laser. By setting the detuning of the laser below the atomic resonance frequency, the atoms travelling in the opposite direction to the beam will experience the light as being closer to resonance due to the Doppler shift, increasing the rate of scattering from this beam. By the same effect, the atoms travelling in the same direction as the beam will perceive the photons as being shifted further away from resonance and have a reduced chance of scattering. The result is that an atom propagating in any direction will experience an imbalance of forces that damps its motion. For the case of a stationary atom, the scattering force from all directions is balanced. This is known as Doppler cooling.

One complication arises from the reality that atoms are not two-level, but are many-level systems. For example, the D2 transition of a Rubidium atom has two ground hyperfine levels (F=1,2), and four excited hyperfine levels (F'=0,1,2,3). The resonant excitation from F=2 to F'=3 is the one used for cooling. This is known as a "closed" transition, as the only allowed decay is back to the F=2 ground state, meaning the atoms are "recycled". In practice, this recycling is hindered by non-resonant excitation from the ground state to the F'=2 and F'=1 levels, from which the atom can decay to either F=2 or F=1 state. If the atom decays to the F=1 state, it will become "dark" to the laser, as the separation between the two ground states is larger than the linewidth of the laser. Atoms that decay to the F=1 state are effectively removed from the cooling process. To solve this problem, a second "repumper" laser is used with the frequency to pump atoms from the F=1 to the F'=2 state, recovering the lost atoms. This process is illustrated in Figure 4.3.

However, it is not possible to achieve arbitrary low temperatures using Doppler cooling. The continuous absorption and re-emission of near-resonant photons that is responsible for cooling is also the source of heating. The heating is produced by the fluctuation of momentum from the recoil of the spontaneously emitted photons, resulting in a random walk of the atoms in velocity space. The Doppler cooling limit is defined as the equilibrium of these two opposing processes, and is expressed by

$$k_B T_{min} = \frac{\hbar \Gamma}{2} \tag{2.2}$$

where Γ is the natural linewidth of the cooling transition [64]. Typical Doppler temperatures are $\sim$100 μK for atoms with allowed optical transitions.

While this limit was derived in 1977, it wasn't until 1985 that this 3D Doppler cooling was demonstrated by Chu *etal*. [65]. In their paper, they referred to this form of optical confinement as "optical molasses', due to the slow, diffusive motion of atoms while inside the beams. It should be noted that while atoms appear to be contained within optical molasses, they are not trapped as there is no restoring force present [66].

2.2 Sub-Doppler Cooling

Soon after the first demonstration of optical molasses, temperatures an order of magnitude lower than the Doppler limit were reported. In 1991, Phillips et al. achieved a temperature of

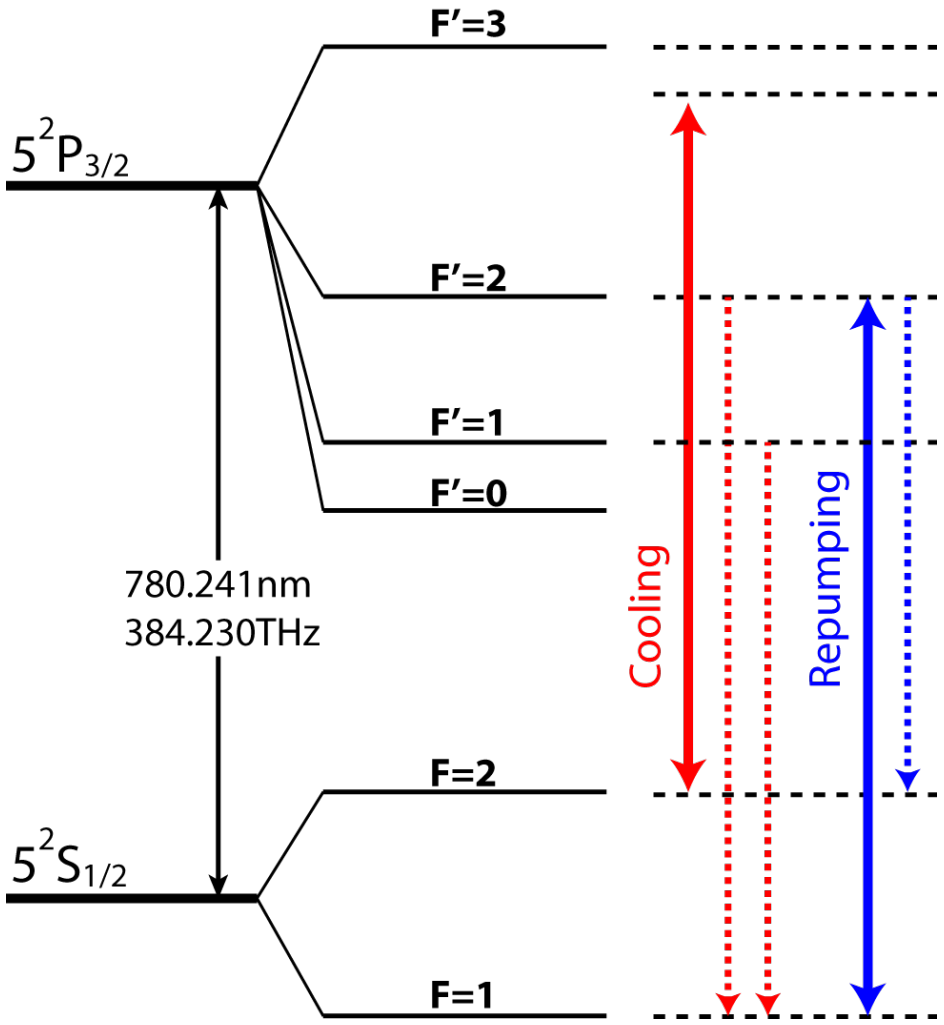

Fig. 2.2 ^{87}Rb D_2 line hyperfine structure. The cooling transition (red bold line) excites atoms from the F=2 state to the F'=3. Due to non-resonant excitation, some atoms are excited into F'=2 and F'=1, from which they can sometimes decay to the "dark" F=1 state (red dotted line). A repumping beam (blue line) is used to "recycle" the atoms to F=2 via excitation to F'=2 from F=1.

just $2.5 \pm 0.6\ \mu K$ for Cs atoms in 3D molasses [67]. The mechanisms for this sub-Doppler cooling were explained in detail by J. Dalibard and C. Cohen-Tannoudji in 1989, using known ideas about optical pumping, light shifts and polarisation gradients [68], and compared with experimental data [69].

Counter-propagating beams in 3D molasses produce polarisation gradients. The lin-perp-lin configuration denotes the case for orthogonal beams with linear polarisations, while $\sigma^+ - \sigma^-$ denotes the case for orthogonal beams with opposite circular polarisation. The lin-perp-lin configuration creates an ellipticity that varies in space. This produces a light-shift of energies of the magnetic sub-levels that oscillates in space. An atom at rest and in equilibrium will be pumped to the most light-shifted state. A moving atom, however, could start at the bottom of a potential "valley" and travel up the potential "hill", before being pumped to the potential valley of the other sublevel. This means that the atom spends a finite amount of time climbing the potential hill before being pumped to the other ground-state sublevel. Because of this time-lag, the atom tends to always climb potential hills, trading its kinetic energy for potential energy. This process is illustrated in Figure 2.3. The potential energy is radiated away during each cycle because photons are emitted at a higher frequency than they were absorbed. This process is analogous to the Greek myth of Sisyphus, cursed to spend eternity pushing a boulder up a hill only to watch it roll back down, and is referred to as Sisyphus Cooling.

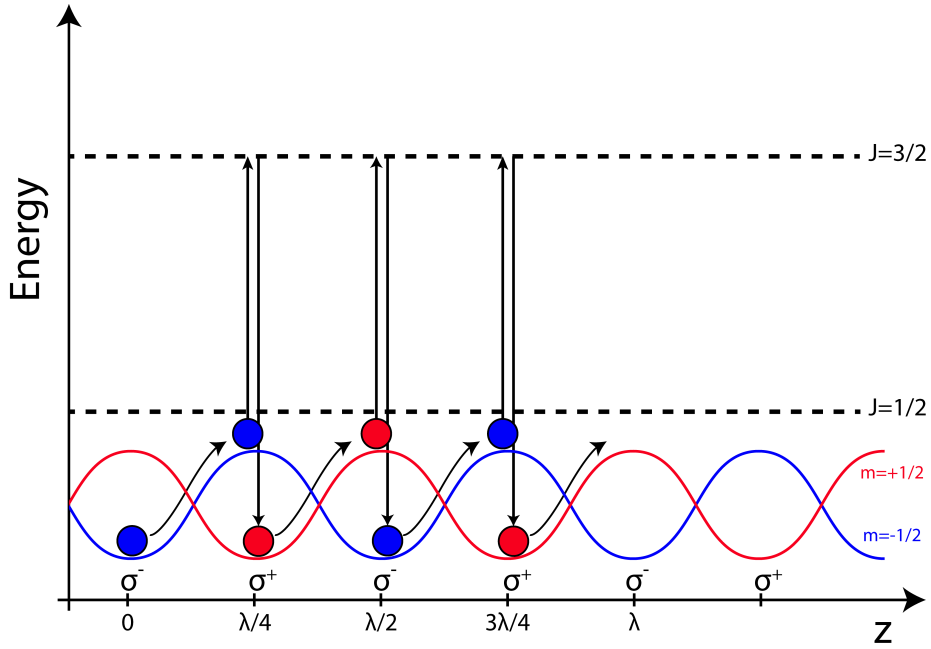

Fig. 2.3 Sisyphus Cooling in the lin-perp-lin configuration

The $\sigma^+ - \sigma^-$ configuration, however, does not produce any potential gradients, and is a lot more challenging to illustrate. For a comprehensive explanation of this type of sub-Doppler cooling, we direct the reader to the paper by J. Dalibard and C. Cohen-Tannoudji [68].

Since sub-Dobbler cooling also relies on momentum transfer between a photon and an atom, the fundamental limit for achievable temperatures can be defined. The velocity change of an atom that absorbed or emitted a photon is known as the recoil velocity, $v_r = (\hbar k)/m$. Therefore the minimum velocity of the atom which one expects to achieve is $v = v_r$. This limit is known as the recoil limit, and expressed as

$$k_B T_R = \frac{\hbar^2 k^2}{M}, \tag{2.3}$$

which is calculated to be 361.96 nK for ^{87}Rb [70].

2.3 Magneto-Optical Trap (MOT)

As the name suggests, the Magneto-Optical Trap is a hybrid trap that utilises both a magnetic field and the optical radiation pressure force to cool and trap neutral atoms. In contrast to optical molasses, there is a restoring force that qualifies this as a trap. The first MOT was demonstrated in 1987 with Sodium atoms [71]. A typical MOT consists of three pairs of red-detuned laser beams, in a $\sigma^+ - \sigma^-$ polarisation arrangement, providing cooling. The trapping is created by a quadrupole magnetic field, produced by a pair of coils in the anti-Helmholtz configuration. The magnetic field produces a Zeeman shift in the sub-levels of the atom, which increases with distance from the centre of the trap. Therefore, the atomic resonance of an atom not at the centre of the trap shifts and is closer to resonance with the beam. This means that the further the atom is from the centre of the trap, the more likely it is to receive photon kicks that push it towards the centre, where the magnetic field is zero. This is further illustrated in Figure 2.4.

While the polarisations of the MOT beams follow the $\sigma^+ - \sigma^-$ arrangement, lin-perp-lin Sysiphus cooling also occurs. Both sub-Doppler cooling processes occur because in practice, the MOT is formed using a 3-dimensional arrangement of beams, and so the atoms are also free to move in all three directions.

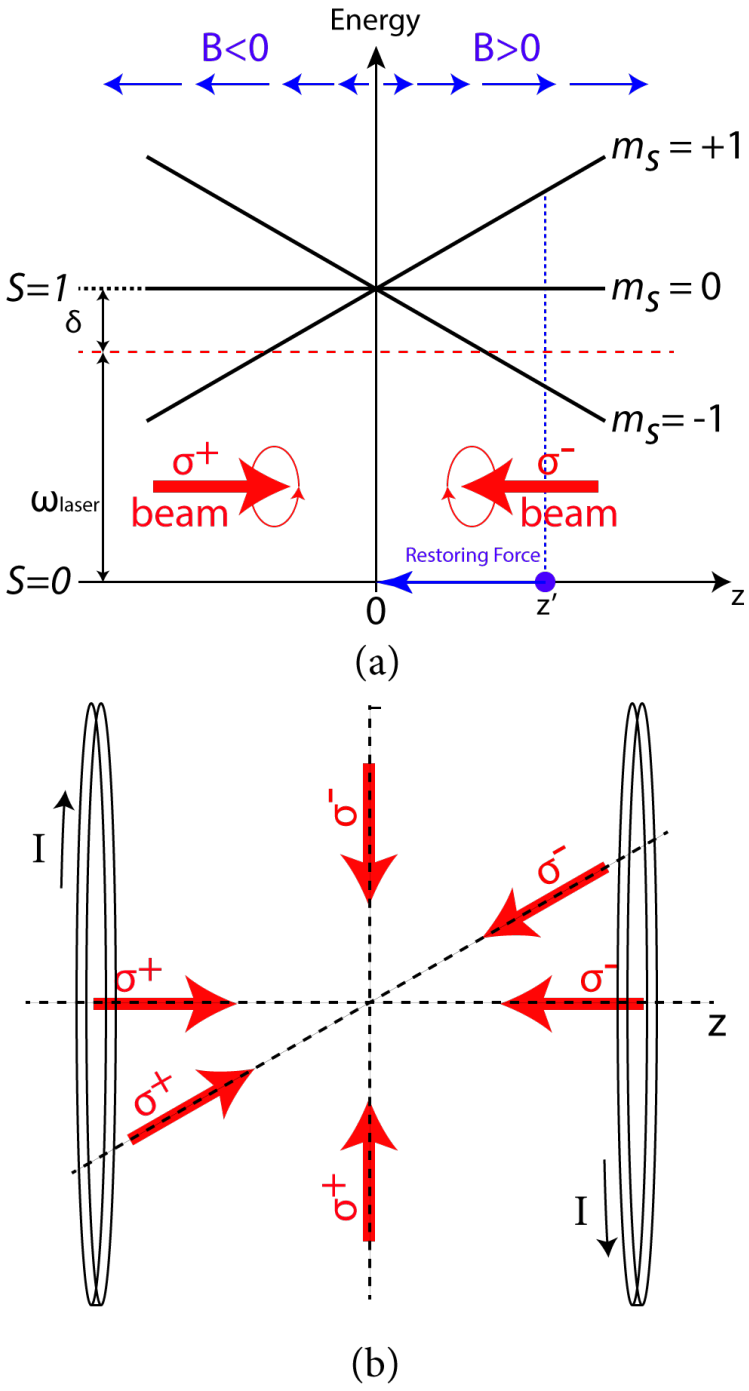

Fig. 2.4 (a) MOT configuration in 1D. Two counter-propagating laser beams with opposite circular polarisation, detuned by frequency, δ, below resonance are shown. In the presence of a magnetic field B_z, the energy sub-levels of the atom are Zeeman split. Due to this, the hypothetical atom at position z' is closer to resonance with the σ^- beam than the σ^+ beam, and experiences a net force towards the centre of the trap. (b) MOT configuration extended to 3D. Three counterpropagating pairs of beams are used in conjunction with a magnetic quadrupole field produced by a pair of anti-Helmholtz coils.

2.4 Optical Dipole Traps

In the next few sections of this chapter, we will introduce some of the critical concepts of optical dipole traps relevant to this work. For further reading we also direct the reader to the extensive review of optical dipole traps [72].

2.4.1 Dipole Potential For 2-Level Atoms

As mentioned in the introduction to this chapter, there are two main types of atom-light interaction. So far, we have been discussing laser cooling concepts involving the radiation pressure from near-resonant light. However, another, weaker force arises when an atom is placed in a laser beam. In the classical approach, the electric field of the light $\tilde{E}$, induces a dipole moment $\tilde{p}$ in the atom and can be expressed as

$$\tilde{p} = \alpha \tilde{E}, \tag{2.4}$$

where α is the complex polarisability of the atom. The interaction potential can be expressed as:

$$U_{dip} = -\frac{1}{2}\left\langle \vec{p} \cdot \vec{E} \right\rangle = -\frac{1}{2\varepsilon_0 c} Re(\alpha) I. \tag{2.5}$$

Considering the laser beam as a stream of photons $\hbar\omega$, the atom will experience cycles of absorption and spontaneous remission. The rate at which the atom gains momentum via this process is called the scattering rate and is expressed as

$$\Gamma_{sc}(\mathbf{r}) = \frac{1}{\hbar\varepsilon_0 c} \mathrm{Im}(\alpha) I(\mathbf{r}). \tag{2.6}$$

For a two-level atom, the polarizability can be expressed in the form:

$$\alpha = 6\pi\varepsilon_0 c^3 \frac{\Gamma/\omega_o^2}{\omega_0^2 - \omega^2 - i(\omega^3/\omega_0^2)\Gamma}, \tag{2.7}$$

where the damping rate, Γ, corresponds to the spontaneous decay of the excited level and is derived using the dipole matrix element between the ground and excited state,

$$\Gamma = \frac{\omega_0^3}{3\pi\varepsilon_0\hbar c^3}|\langle e|\mu|g\rangle|^2. \tag{2.8}$$

Substituting the expression for polarizability into equations (2.5) and (2.6) gives the expressions for the dipole potential and scattering rate:

$$U_{dip}(r) = -\frac{3\pi c^2}{2{\omega_0}^3}\left(\frac{\Gamma}{\omega_0-\omega}+\frac{\Gamma}{\omega_0+\omega}\right)I(r), \tag{2.9}$$

$$\Gamma_{sc}(r) = \frac{3\pi c^2}{2\hbar{\omega_0}^3}\left(\frac{\omega}{\omega_0}\right)^3\left(\frac{\Gamma}{\omega_0-\omega}+\frac{\Gamma}{\omega_0+\omega}\right)^2 I(r). \tag{2.10}$$

When using laser frequencies that have relatively small detuning from resonance, ($\omega/\omega_0 \approx 1$), these equations can be simplified using the rotating wave approximation [73] to:

$$U_{dip}(r) = -\frac{3\pi c^2}{2{\omega_0}^3}\left(\frac{\Gamma}{\Delta}\right)I(r), \tag{2.11}$$

$$\Gamma_{sc}(r) = \frac{3\pi c^2}{2\hbar{\omega_0}^3}\left(\frac{\Gamma}{\Delta}\right)^2 I(r), \tag{2.12}$$

where Δ is the detuning, $\Delta = \omega - \omega_0$.

These expressions provide us with two fundamental observations of dipole trapping: the sign of the detuning determines whether the dipole potential is attractive (red-detuned) or repulsive (blue detuned). The scattering rate, which is responsible for heating, scales as I/Δ^2, while the dipole potential scales as I/Δ. This means that the most efficient way to minimise heating in dipole traps is to use large detunings and high-intensity beams.

2.4.2 Dipole Potential For Multi-level Atoms

When calculating the trapping potential of an optical dipole trap, the 2-level approach is insufficient. This is because real alkali atoms are many-level systems with a complex substructure.

In the work presented in this thesis we utilise a far-off-resonance trap (FORT), produced by a 1064 nm laser beam, to trap ^{87}Rb atoms. In this scheme, the detuning of the laser from the atomic transition frequency is much larger than the splitting of the hyperfine ground and excited states and the fine structure splitting, ($|\Delta| \gg \Delta_{HFS}, \Delta'_{HFS}, \Delta'_{FS}$). Under these conditions, the $D_2(5^2S_{1/2} \rightarrow 5^2P_{3/2})$ and $D_1(5^2S_{1/2} \rightarrow 5^2P_{1/2})$ transitions are responsible for the largest contribution to the dipole potential. We can calculate the trapping potential by summing the contributions of the D_2 and D_1 transitions (for linearly polarised light) [72]:

$$U_{dip}(\vec{r}) = \frac{\pi c^2}{2}\frac{\Gamma_{D1}}{\omega_{D1}^3}\left(\frac{1}{\omega-\omega_{D1}}+\frac{1}{\omega+\omega_{D1}}\right)I(\vec{r}) + \frac{\pi c^2}{2}\frac{\Gamma_{D2}}{\omega_{D2}^3}\left(\frac{2}{\omega-\omega_{D2}}+\frac{2}{\omega+\omega_{D2}}\right)I(\vec{r}) \tag{2.13}$$

For an even more accurate calculation, one must consider the frequency-dependent polarisability of the ground state of the atoms by taking into account all the electronic states of the atom. A detailed analysis for the calculation of the polarisability for different atoms and wavelengths was performed by Safronova [74]. For 1064 nm laser wavelength, the frequency-dependent polarisability is given (in atomic units) as $\alpha_0 = 686.9a_0^3$, where a_0 is the Bohr radius. We convert to SI units using $\alpha_0(SI) = 4\pi\varepsilon_0 a_0^3 \alpha_0(AU)$. The potential depth of a single beam dipole trap is then:

$$U_0 = -2\pi I\alpha/c, \tag{2.14}$$

where I is the intensity of the beam.

In our set-up, the optical dipole trap is formed using a 1064 nm laser beam with an optical power of $\sim$20 W and a beam waist of 70 μm. For comparison, we provide the values of the potential depth calculated by:

- using the two-level model,

	$D_2(5^2S_{1/2} \rightarrow 5^2P_{3/2})$	$D_1(5^2S_{1/2} \rightarrow 5^2P_{1/2})$
Frequency, ω_0	$2\pi \cdot 384.230\,484\,468\,5$ THz	$2\pi \cdot 377.107\,463\,5$ THz
Decay Rate, Γ	$38.11 \times 10^6 s^{-1}$	$36.10 \times 10^6 s^{-1}$

Table 2.1 Frequency and Decay Rate of the D_2 and D_1 transitions of ^{87}Rb [70].

- by considering the contributions of the D_2 and D_1 transitions,
- using the precise values of polarisability provided in [74].

Using the two-level model, we calculate the potential depth of a single beam to be $U_0 = 336.4$ μK. Using equation 2.13 and the known values of the frequency and decay rates of the D_2 and D_1 transitions of ^{87}Rb, see Table 2.1, the trapping depth of the beam is calculated as $U_0 = 389.7$ μK. Finally, using the exact value of polarisability, we calculate $U_0 = 400.8$ μK.

In comparison to the precise value, the 2-level approximation gives an error of $\sim 16\%$. This is a significant error, despite the fact that the fine splitting of the excited state of Rb is ~ 15 nm and the frequency detuning of our laser is ~ 280 nm, which is close to a two-level system. Taking into account the contributions of the D_2 and D_1 transition provides a much better estimate with an error of $\sim 2.8\%$.

2.4.3 Optical Dipole Traps

The simplest way to to create an optical dipole trap is to use an intense Gaussian beam tuned far below the atomic resonance. The focus of the beam will form the region of highest intensity, towards which the atoms will be attracted due to the gradient force. The radius of the beam along the axis of its path is expressed by:

$$w(z) = w_0 \sqrt{1 + (\frac{z}{z_R})^2}, \tag{2.15}$$

where w_0 is the beam waist and $z_R = \pi w_0^2 / \lambda$ is the Rayleigh length.

The intensity of the Gaussian beam is:

$$I(\vec{r},t) = \frac{2P}{\pi w(z)^2} exp\left(-\frac{2r^2}{w^2(z)}\right). \tag{2.16}$$

Atoms with thermal energies much lower than the trapping depth of the ODT will occupy the bottom of the trap. Near the bottom of this trap the harmonic approximation can be applied which provides an estimate for the trap frequencies in the radial and axial directions:

$$\omega_r = \sqrt{\frac{4U_0}{m\omega_0^2}} \quad \text{and} \quad \omega_z = \sqrt{\frac{2U_0}{mz_R^2}}, \tag{2.17}$$

where ω_r and ω_z are trapping frequencies in the radial and axial direction respectively. As expected, in a single beam, the confinement along the axis of propagation is much weaker than in the radial direction. This results in a shallow potential along the axis of propagation, with a lot of atoms populating the "wings" of the trap. This becomes an issue when attempting to cool atoms further via forced evaporation, where maintaining high atom density is crucial. Crossed-beam configurations are typically used in order to achieve deep potentials with strong confinement in all directions.

2.4.4 Crossed Optical Dipole Traps and Evaporative Cooling

Crossed ODT are created by crossing two beams with orthogonal polarisation. Typically this is done by recirculating the beam, and re-focusing it so that the foci are superimposed. This configuration provides tight trapping in all directions, being fully symmetrical in all directions when crossed at 90°. The effective volume of the trap can be increased by reducing the crossing angle. A larger volume trap can trap more atoms while still maintaining high densities, which is vital for producing an all-optical BEC via forced evaporation[75]. The resulting optical potential for a crossed ODT $2\theta = 20°$ is illustrated in Figure 2.5. Here the z-axis is the axis of symmetry, and the angle between it and each beam is θ. The crossing angle between both beams is, therefore, 2θ. The illustration also shows that while the potential depth at the crossing region is $2U_0$, the effective potential depth is U_0, as atoms with higher energies, are able to leave the trap along one of the beams.

The trapping frequencies at the centre of the crossed dipole trap are derived via harmonic approximation of the trap centre:

$$\omega_z(\theta) = \sqrt{\frac{4U_0}{M}}\sqrt{\frac{cos^2\theta}{z_r^2} + \frac{2sin^2\theta}{w_0^2}}, \tag{2.18}$$

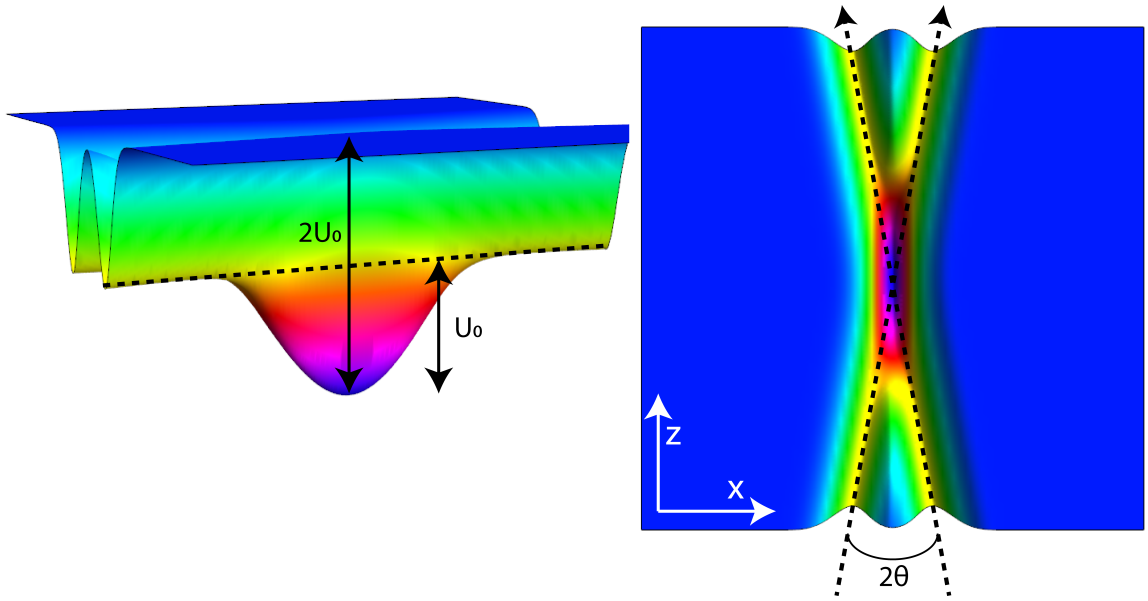

Fig. 2.5 Illustration of the resulting dipole potential at the crossing of two beams at $2\theta = 20°$. Left: Side view. Right: Top down view.

$$\omega_x(\theta) = \sqrt{\frac{4U_0}{M}}\sqrt{\frac{2cos^2\theta}{w_0^2} + \frac{sin^2\theta}{z_r^2}}, \tag{2.19}$$

$$\omega_y(\theta) = \sqrt{\frac{8U_0}{Mw_0^2}}. \tag{2.20}$$

Evaporative cooling is the technique used to cool atoms past the limits of laser cooling. The first Bose-Einstein Condensate (BEC) was produced using magnetic evaporation in 1995 [76], followed by the first all-optical evaporation to BEC in 2001 [77]. Instead of momentum transfer, evaporative cooling is based on the preferential removal of the hottest atoms from a sample. In optical dipole traps, forced evaporation is performed by lowering the depth of the trap to allow the most energetic atoms to escape. The remaining atoms re-thermalise due to elastic collisions. This results in runaway evaporation, as the atoms sink lower in the potential as they get colder, further increasing the density and the thermalisation rate.

2.4.5 Gravity Sag

So far, we have ignored the presence of gravity when considering the trapping potential of optical dipole traps. For a horizontally aligned beam, the effect of gravity results in a "sag" of the potential in the vertical radial direction by $\sim Mgw_0$. The effect of gravity sag on the trapping potential at the waist of a single beam dipole trap is illustrated in Figure 2.6.

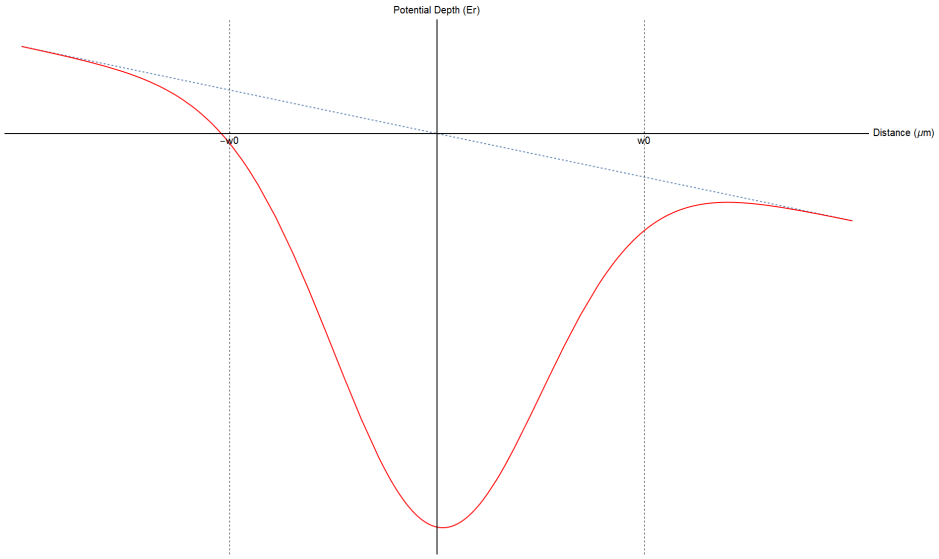

Fig. 2.6 Optical dipole potential in the presence of gravity in the radial direction of a horizontal beam. The solid red line represents the trapping potential, while the dashed blue represents the gravitational potential. The $1/e^2$ beam waist is labeled as w_0 and is 75 μm for this case.

Practically, this means that even for arbitrarily cold atoms, there is a minimum trapping power that is required to hold atoms against the force of gravity. As evaporation in an optical dipole trap requires turning down the intensity of the trapping beams, it is useful to know this limit. We can compute the minimum power of the laser beam, in terms of its waist, by writing the total potential as:

$$U(x) = U_0 e^{-2x^2/w^2} - mgx, \tag{2.21}$$

then differentiating to determine x for the maximum force such that:

$$\frac{\mathrm{d}^2U}{\mathrm{d}^2x} = \frac{\mathrm{d}F}{\mathrm{d}x} = 0. \tag{2.22}$$

To compute the minimum power required, we substitute the calculated value of x and solve $dU/dx = F(x) > 0$. This gives us the expression for the minimum trapping power, P_{min}, in terms of the beam waist, w_0:

$$P_{min} = \frac{e^{0.5}\omega_0^3\Delta}{6c^2\Gamma} mgw_0^3. \tag{2.23}$$

The relationship between the beam waist and minimum trapping power is illustrated in Figure 2.7, for the relevant case of Rubidium atoms trapped using a single 1064 nm beam with a waist radius of 75 μm.

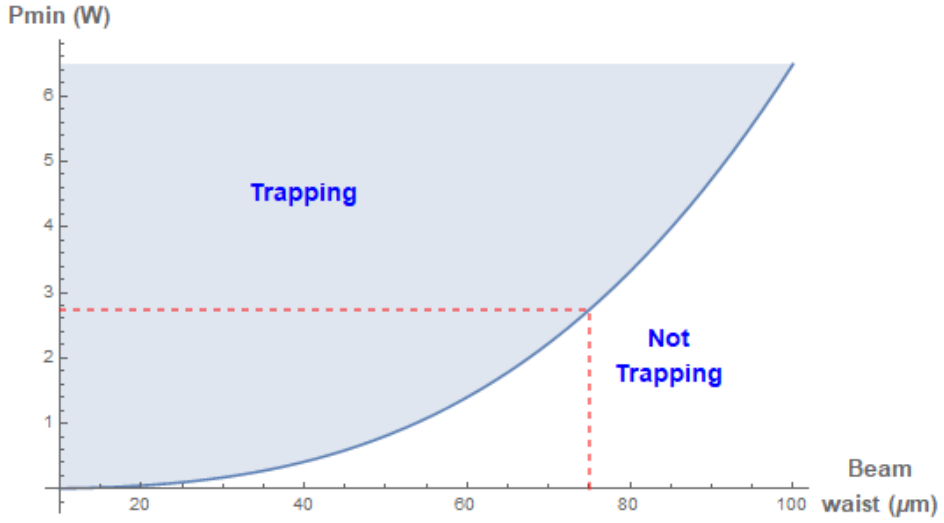

Fig. 2.7 Minimum Trapping Power to Support Against Gravity. For a beam with $w_0 = 75$ μm, the minimum trapping power, $P_{min} = 2.7\ W$.

Chapter 3

Design and Construction of the Apparatus

3.1 Introduction

This section documents the nuts and bolts of the experiment, such as the UHV chambers and components as well as the procedures we used to achieve UHV conditions. I became involved with the project before any of the apparatus was designed or assembled. Throughout my PhD, I was heavily engaged in the design and construction of the UHV chambers and optical systems needed for trapping and cooling of rubidium atoms. The development of a suitable UHV chamber took the most amount of time by far. We designed several vacuum chambers using the SolidWorks 3DCAD software package. While a total of three designs were realised, it was only possible to build and test one chamber at a time due to us having access to just one set of vacuum pumps. In this chapter, we discuss the experimental needs that our chamber designs had to accommodate and present the successes and failures of each chamber when put into practice.

During testing of the preliminary chamber designs, we also discovered several design shortcomings of the LVIS chamber, which was designed before my involvement in the project. We were unable to saturate this "old" LVIS chamber with Rubidium, and so I was given the responsibility to redesign the LVIS chamber. In the second half of this chapter we discuss how the materials used in the initial LVIS chamber compromised its performance, and

we present the improved LVIS chamber design. In Chapter 6, we evaluate the performance of our LVIS and its advantages over other LVISs from literature.

The main design parameters of the UHV chambers were as follows:

- A double MOT system (LVIS and MOT) for the accumulation of a sufficient number of atoms for BEC. A double MOT system typically consists of two connected chambers at different partial pressures of Rubidium (or any other chosen atom). The first chamber produces a high flux of atoms while the second chamber maintains an ultra-high vacuum ($<5 \times 10^{-10}$mbar). Better vacuum conditions allow for longer lifetimes of trapped atoms and the intense atomic flux ensures a high number of atoms trapped in the MOT - both necessary starting conditions for producing a BEC.
- The science chamber should have maximal optical access for all the NIR and visible laser beams.
- The science chamber should incorporate a fused silica prism, which will be used to produce an initial evanescent wave (EW) trap for atoms near the surface of the prism. It should also be possible to substitute the prism with another prism containing an atom chip at a later point.
- A small volume chamber design is prefered as it makes it easier to achieve and maintain ultra-high vacuum conditions. Additionally, reducing the size of the science chamber also allows us to use smaller magnetic coils for the MOT and simplifies the alignment of the laser beams.

In practice, this meant that each chamber we designed comprised of the following:

- A double MOT system (LVIS and 3D-MOT), with excellent optical access to both chambers.
- An ion and getter pumps to maintain UHV conditions which would otherwise be compromised due to outgassing. The demanded vacuum is $< 10^{-10}$mbar, which the ion pump is capable of achieving under the right conditions. The getter is used to primarily pump out hydrogen, which is not efficiently pumped by the ion pump. A SAES Getters, NEXTorr D 100-5 combination ion/getter pump was used for all chamber iterations. The pump doesn't have any moving parts and therefore, does not produce mechanical vibrations, which is essential for BEC production.

- A Rb reservoir, to house a solid sample of Rubidium. This comprised of a DN16CF full nipple flange, with one end terminated by a blank flange.
- A fused silica prism in close proximity ($\sim$1 cm) to the MOT in the main chamber, for the study of EW surface traps and atom chips.

3.2 Preliminary Chamber Designs

An all-glass chamber design was considered prior to my involvement with the project. A large, fused silica prism was coupled to a glass chamber using an indium seal. While providing maximum optical access, this design proved to be unsuccessful in practice. This was due to the glass chamber not being rigid enough to withstand the pressure of clamping the prism, required to maintain the seal. This section details the next two chambers that were designed and built.

Prior to the final chamber design, (see later), two other chambers were designed and constructed. The first chamber comprised of an octagonal steel vacuum cell, manufactured by Kimball Physics, which we modified to allow for a fused silica prism to be indium sealed to it. DN16CF viewports placed at each flat surface of the octagon, in addition to the prism, provided desirable optical access. The double MOT system was formed by the LVIS chamber and the octagonal science cell, connected together using a tube. The "old" LVIS chamber, which was designed prior to my involvement, featured a glass cell indium sealed to a steel port. We will refer to this chamber as the “octagon chamber”. The 3D design, as well as a photograph of the assembled system, are presented in Figure 3.1.

The chamber was successfully baked, and UHV vacuum was achieved. However, we experienced issues while attempting to saturate the LVIS chamber with Rb vapour. Usually, this is performed by opening the valve between the chamber and the reservoir in which a Rb sample is stored. The tube is then heated using heating tapes, at 50°-90°C, thus increasing the rubidium pressure and letting it diffuse into the LVIS chamber. However, we were not able to observe any Rb in the LVIS chamber via absorption spectroscopy. We tried swapping out the Rb sample in the reservoir, as well as applying heat to accelerate the process. After two weeks no rubidium was detected in the chamber. More importantly, the vacuum conditions became compromised due to a partial failure of the indium seal between the prism and the

octagonal cell. A clamp was manufactured to compress the prism to the cell, but this could not be a permanent solution as it denied essential optical access.

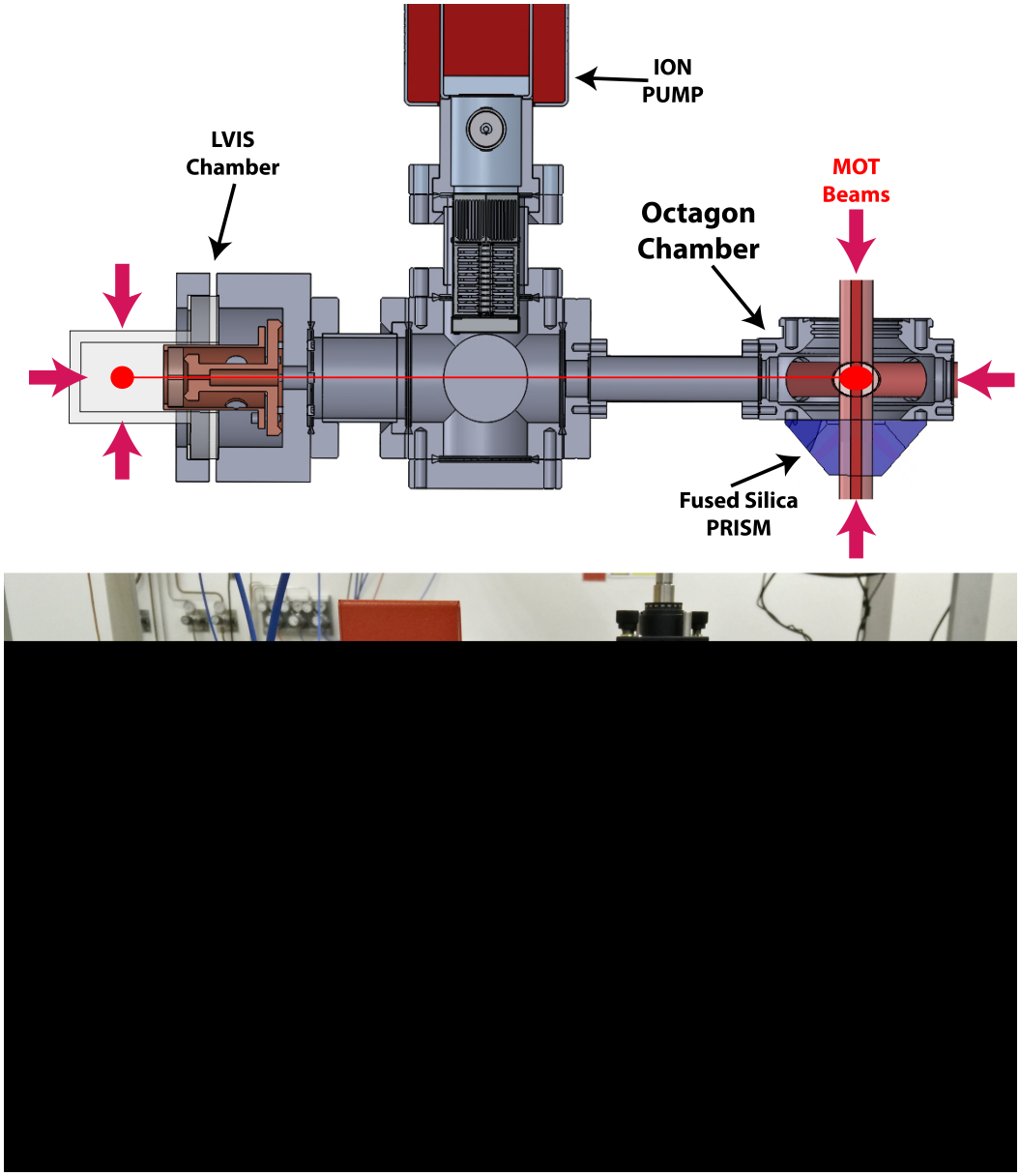

Fig. 3.1 Octagon Chamber. Top: 3D design of the chamber. Bottom: Assembled octagon chamber after UHV baking.

The second design improved on the first. The notable feature of this chamber was the science cell, which consisted of a glass cube with its top face replaced by a fused silica prism. We will refer to this chamber as the "glass house" chamber. The glass chamber would provide the maximum optical access, while its small size (40x40 mm) meant that we could use smaller magnetic coils. We opted to use Epotek glue to attach the prism to the cell, due to the higher

recommended baking temperature than that of indium, which should provide a better vacuum and reduce outgassing.

We also decided to use this opportunity to redesign the LVIS chamber, which will be discussed in detail later in this Chapter. The improved design had several advantages, but due to delays in manufacturing we were forced to use the old LVIS chamber again. We suspected that the poor performance of the old LVIS chamber was due to the mirror clamp, which was made from copper and had a large surface area, which absorbed Rubidium and prevented saturation. To test this theory, we swapped out the copper mirror clamp with a steel one. The assembled "glass house" chamber is shown in Figure 3.2.

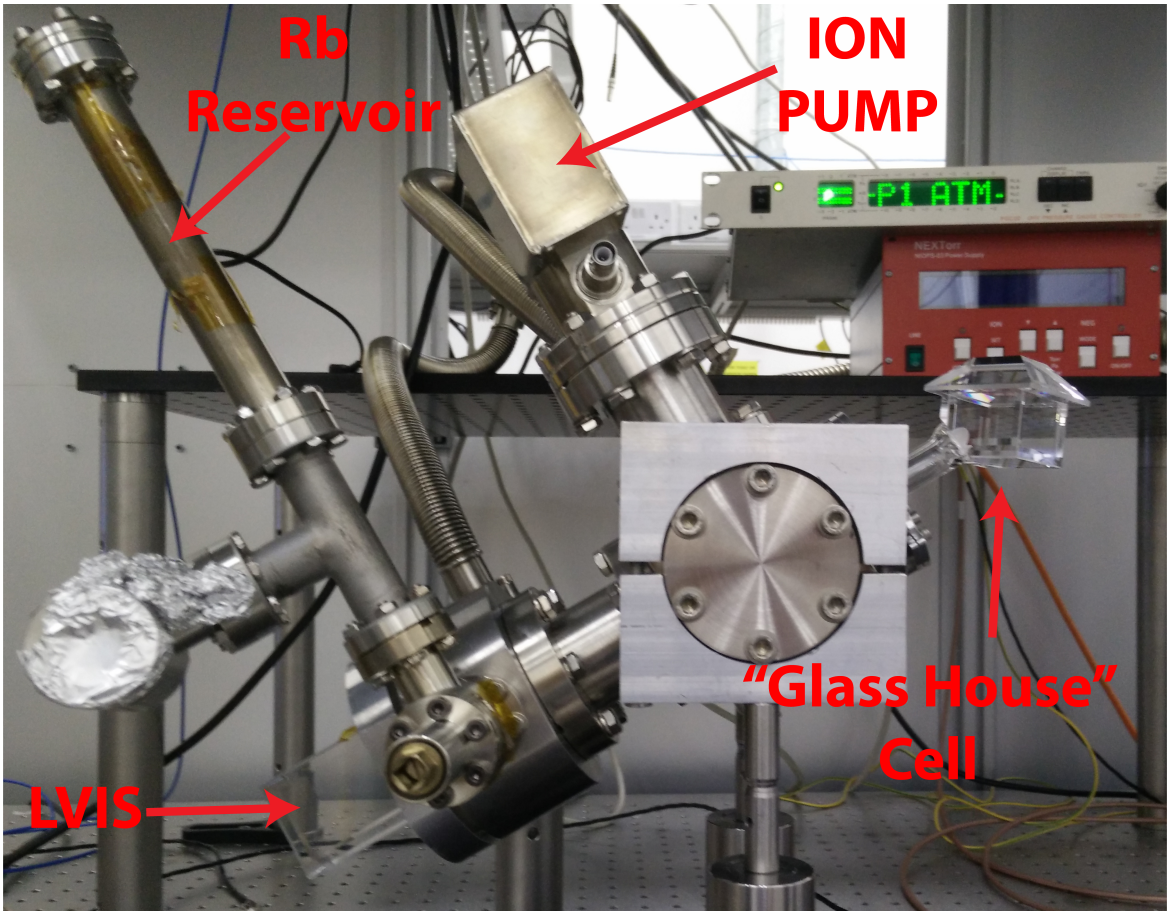

Fig. 3.2 Assembled glass house chamber.

The chamber was baked, and UHV of 10^{-11} mbar was achieved. Rubidium was detected in the LVIS after less than a day of heating the Rb tube at 60°C. Since the LVIS chamber remained virtually unchanged, other than the mirror clamp, this suggests that the large copper parts were indeed absorbing the Rubidium and preventing saturation in the previous

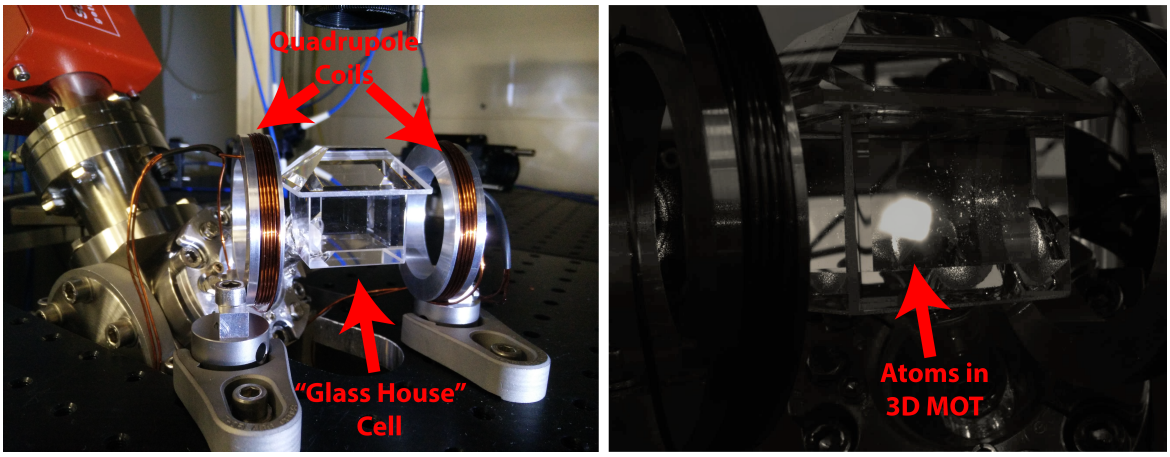

Fig. 3.3 Glass House Chamber. Left: Glass house cell and quadrupole coils for MOT. Right: Fluorescence of atoms trapped in the MOT in the glass house.

design. The glass house chamber was used to produce a working 3D-MOT of rubidium atoms, see Figure 3.3, as well as trap rubidium atoms in the 1064 nm dipole trap. However, a disappointingly low lifetime of trapped atoms within the dipole trap was measured. This is shown in Figure 3.4.

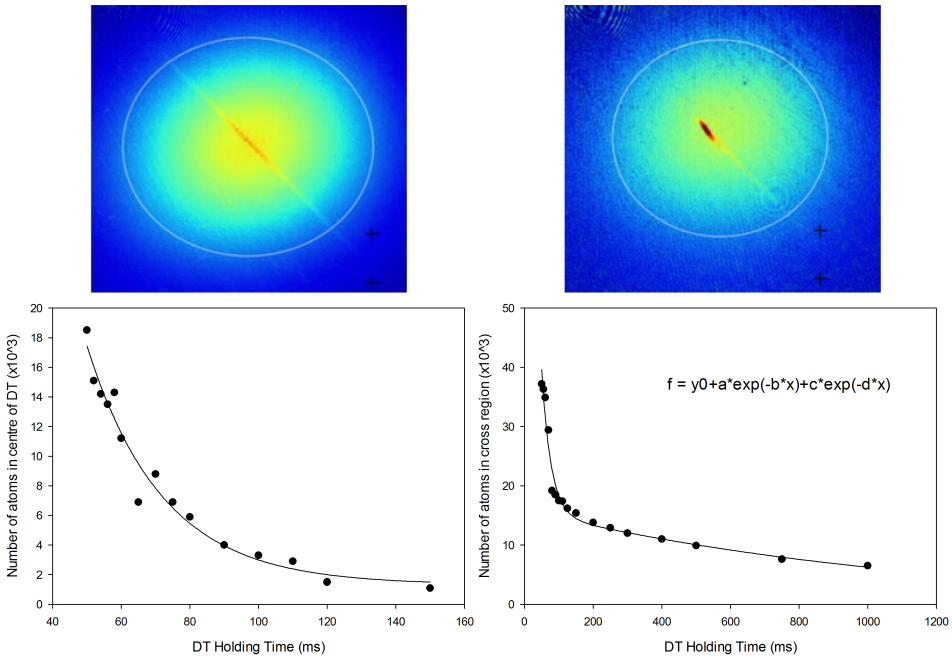

Fig. 3.4 Lifetime of atoms trapped in crossed dipole trap formed by a single beam (left) and crossed beams (right) within the Glass House Chamber. The 1/e lifetimes are 78 ms and 150 ms respectively.

The 1/e lifetime of the crossed dipole trap was just 150 ms. Considering that to evaporate an atom sample to BEC typically takes between 3 and 10 seconds, the observed lifetime is far too short and is indicative of poor vacuum conditions. It is suspected that there was a leak at the junction where the prism was glued to the glass cell using Epotek glue. At this point, we decided to redesign the chamber entirely and opt for a more robust, albeit larger design as well as implement the improved LVIS chamber.

3.3 Final Chamber Design

The final vacuum chamber we designed and built avoided the failures of the previous two designs. We settled for a robust, reliable design that eliminated the need for indium seals and glues completely. The science cell comprised of a large volume spherical cube chamber, manufactured by Kimball Physics. We will refer to this chamber as the "globe chamber", the design of which is illustrated in Figure 3.5. It featured 6×DN63CF, 8×DN40CF, and 12×DN16CF ports. We attached the improved LVIS chamber to the science chamber via a DN40CF port and a short tube. Another DN40CF port was used to attach the NEXTorr combination ion/getter pump. All of the remaining ports were fitted with glass viewports for maximum optical access.

The large volume of the science chamber allowed us to place the fused silica prism inside the chamber, eliminating the need for glue or indium seals. The prism had to be placed near the centre of the chamber, in order to have the optical access to couple the 532 nm and 1064 nm beams at proper angles for the future study of bichromatic evanescent wave traps. A stainless steel holder was designed to hold the prism and suspended it ∼7.5 mm above the intended position of the centre of the MOT. This would allow for sufficient clearance of the 15 mm 3D-MOT beams while keeping the surface of the prism as close to the atoms as possible. The steel holder was attached to the inside ridges of the top DN63CF port prior to sealing the chamber for baking. This was performed inside a negative pressure enclosure to avoid contaminating the prism surface with dust particles. The holder clamps the prism and attaches to the chamber mechanically using set screws. This allows us to swap out different prisms and atom chips in the future without damaging these components, as opposed to the previous case when using glue or indium.

Even though the globe chamber was significantly larger in volume than its predecessors, we were able to bake it at a higher temperature, (due to the absence of glue, indium and large

glass surfaces), and were able to achieve a vacuum of $\sim 10^{-11}$mbar. However, a significant disadvantage of using a large chamber is that the magnetic coils required for the MOT end up being placed far away from the trap centre ($\sim$11 cm). This results in the need for larger magnetic coils with more turns and liquid cooling. We discuss the issue of magnetic coils in detail in Chapter 5.

Using this chamber, we were able to characterise the new LVIS chamber successfully, produce a large 3DMOT of $>4\times10^9$ atoms and demonstrate optical dipole trapping using a 1064 nm laser (see results in Chapters 6 and 7).

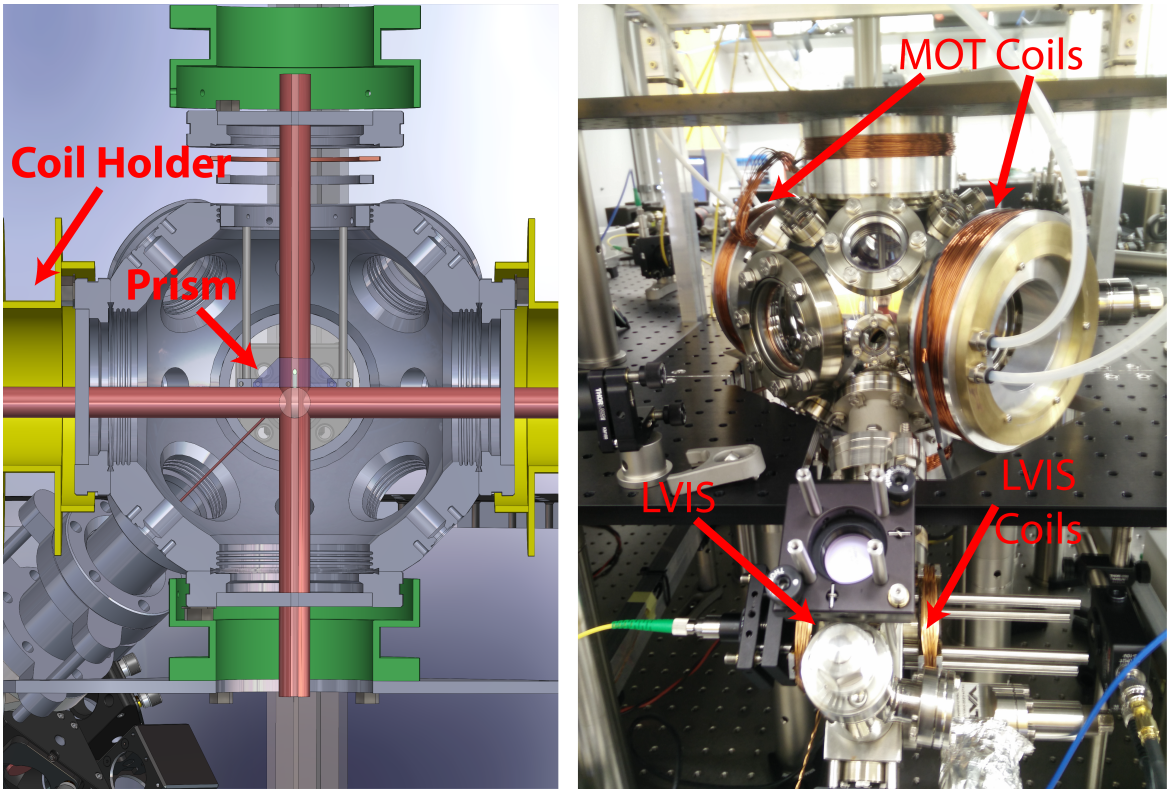

Fig. 3.5 Globe Chamber. Left: 3D mockup in Solidworks. Right: Fully assembled chamber after baking.

3.4 LVIS Chamber Design

The first Low-Velocity Intense Source of Atoms (LVIS) was demonstrated in 1996 [78] and became quickly adopted due to its advantages over other cold atom sources, such as the Zeeman slower [79]. While the Zeeman slower can produce significantly higher fluxes of

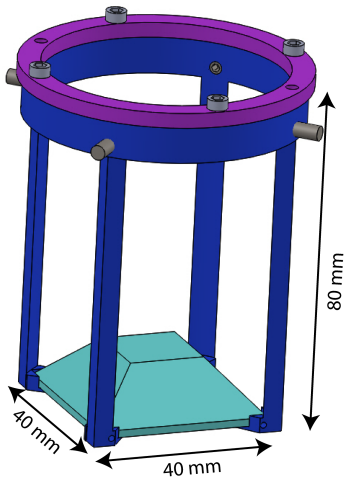

Fig. 3.6 3D Design of the prism holder. Set screws at the top of the holder were used to suspend it from the top port of the vacuum chamber.

atoms (10^{11} atoms/s), the LVIS is able to produce a collimated beam of atoms, with fluxes of up to 10^{10} atoms/s but with lower velocities and a much better proportion of slow vs thermal atoms. In addition to the LVIS, there are other MOT-based cold atom sources such as the 2D-MOT [80] and 2D$^+$-MOT [81]. The LVIS was chosen for our experiment as it uses a quadrupole magnetic field which is easy to set up using a single pair of magnetic coils while performing much better than the 2D-MOT and comparably to the 2D$^+$-MOT [82].

A typical LVIS functions a lot like a 3D-MOT. It has three pairs of counter-propagating beams and a magnetic quadrupole field. Unlike a 3D-MOT, one of the beams, counter-propagating to the “push” beam, has a dark channel created by using a mirror with a hole in it. Atoms within the dark channel feel a net force in the direction of the “push” beam and are pushed through the hole. This scheme is illustrated in Figure 3.7. The magnitude of the flux of atoms produced by the LVIS depends on several factors:

- the diameter of the "exit" hole,
- the partial pressure of Rubidium inside the LVIS chamber,
- the precision of the alignment of the cooling beams,
- and balance of intensity between beam pairs.

Typically, a flux of 8×10^9 atoms/s with an average atom velocity of $\sim$8 m/s is expected [82].

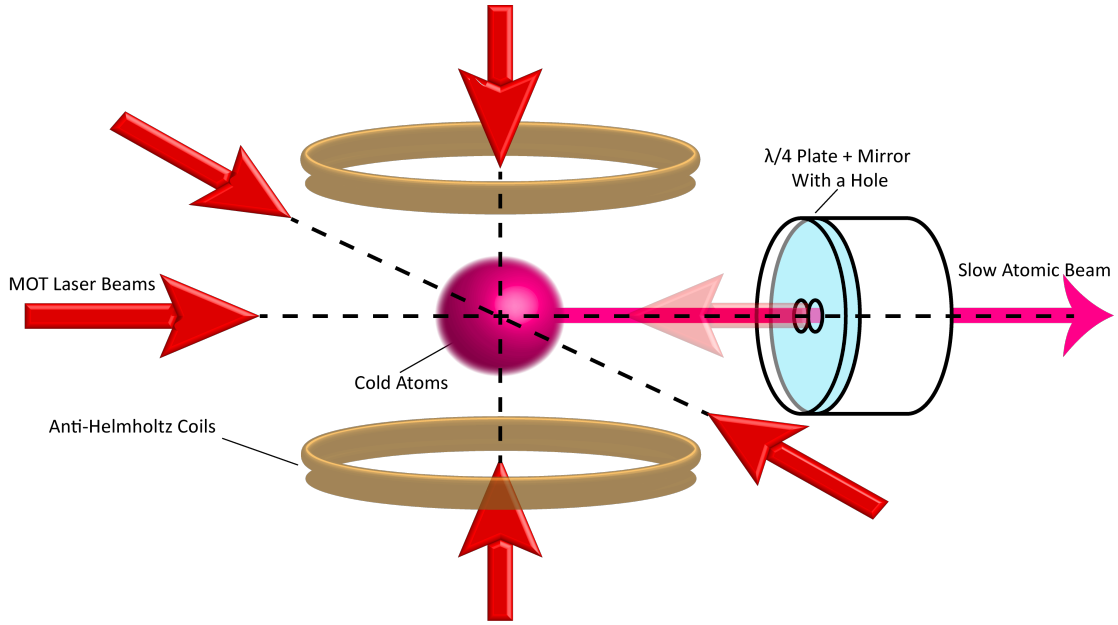

Fig. 3.7 Typical LVIS Configuration. Similar to a 3D-MOT, the LVIS is set up using three pairs of counter-propagating beams and a magnetic quadrupole field produced by a pair of magnetic coils in an anti-Helmholtz configuration. A mirror and a $\lambda/4$ waveplate is used to produce a retro-reflected beam and rotate its polarisation by π. A small aperture through the centre of the waveplate and mirror produces a "dark" channel in the retro-reflected beam. Atoms entering this channel will experience a net force in the direction of the "push" beam and will be subsequently extracted through the hole in the mirror in the form of a slow atomic beam.

The "old" LVIS design, used in the first two of our chambers, consisted of two parts - a large glass cell and a steel chamber indium-sealed together. The retro-reflective mirror was internally clamped using a large copper clamp. This design is illustrated in Figure 3.8. The glass cell offered the advantage of high optical accessibility. However, the indium seal made this design less robust and restricted the baking temperature to 150°C. As mentioned earlier, we had difficulties with saturating the old LVIS chamber with rubidium. Initially, we thought the problem was caused by our handling of the rubidium sample before baking. The rubidium sample comes in a small glass cell, that must remain sealed during the baking progress. If the cell became damaged during insertion into the reservoir, the rubidium sample would quickly oxidise during baking. However, even after exchanging the rubidium sample for a new one and repeating the procedure with care, we were still unable to detect rubidium in the chamber using absorption spectroscopy. We concluded that the large surface area of the copper clamp, and possibly the glass, contributed to the lack of free rubidium in the cell through absorption. When we removed the copper clamp and replaced it with a steel version, we were able to saturate the chamber after just a few days, while heating the Rb reservoir at 60°C.

By the time we got the old LVIS chamber functioning, we have already committed to producing a new design and having it manufactured. I was given the responsibility of producing a viable design that improved on the old LVIS chamber. This involved the use of 3D CAD software package, Solidworks, as well as corresponding with a vacuum parts manufacturer, “Hositrad”, to ensure that our design was feasible. The new design aimed to improve on the old LVIS chamber in the following ways:

- The volume should be kept to a minimum. This would improve the vacuum conditions, while also making it easier to saturate the smaller volume with rubidium after baking.
- Avoid indium seals. This meant getting rid of the large glass cell and opting for several strategically placed viewports. Absence of the indium seal would result in a much more robust chamber and lower the risk of leaks. Reducing the glass surface area should improve rubidium saturation, as the glass can adsorb rubidium.
- Use stainless steel instead of copper for internal parts. This should have a big impact on the saturation of rubidium in the chamber, as we concluded during the use of the old LVIS chamber.

Using these specifications, we designed the new LVIS chamber, which consisted of an entirely custom-made steel vacuum chamber. The 3D design, mocked up in Solidworks, is illustrated in see Figure 3.9. The steel chamber was manufactured by "Hositrad", in

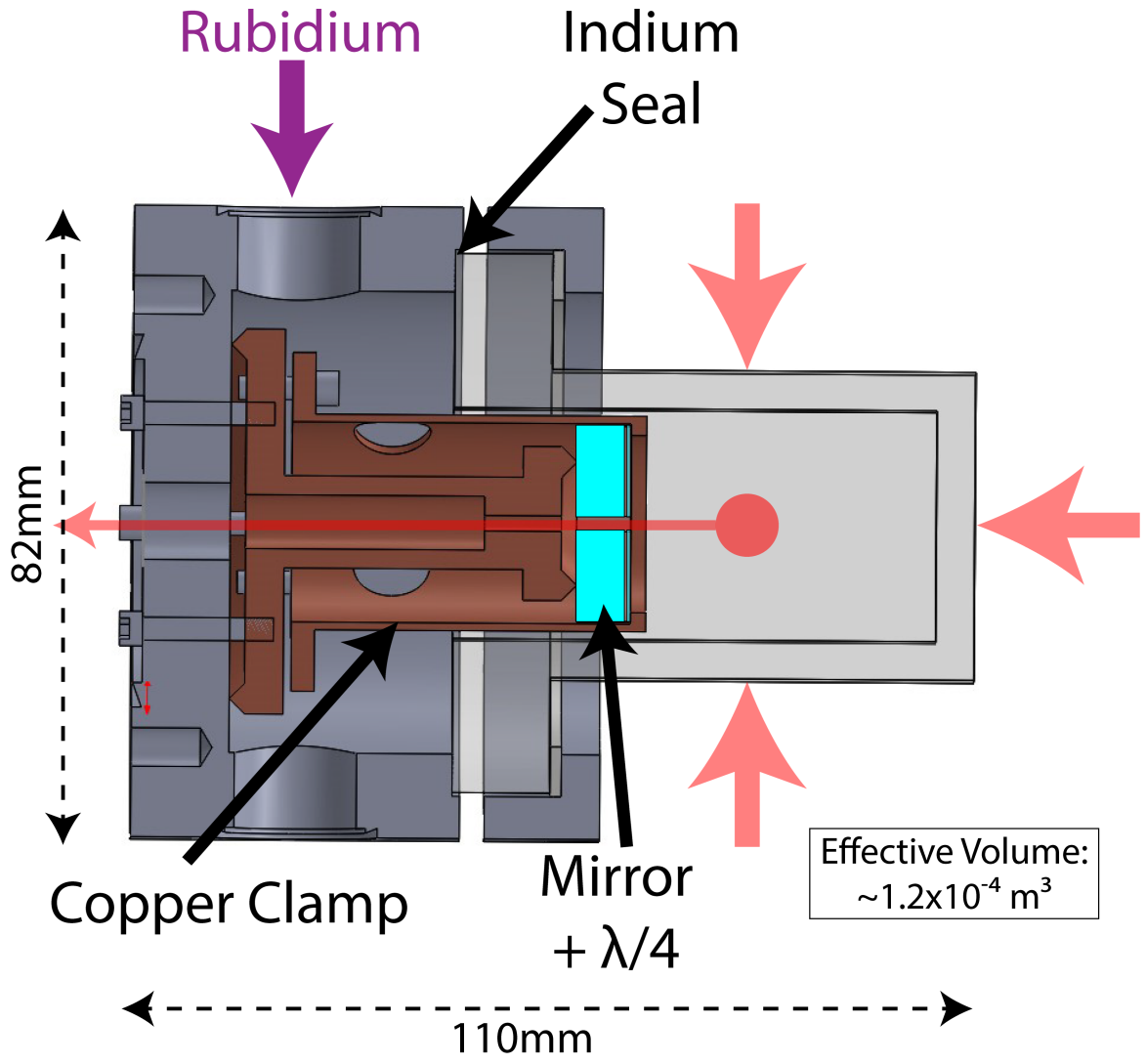

Fig. 3.8 “Old” LVIS Chamber Design. This design was tested as part of the glass house and octagonal science chambers. It featured a large glass section that provided maximum optical access for the LVIS beams. A large copper clamp was used to hold the mirror and waveplate. An indium seal was used at the glass and metal junction.

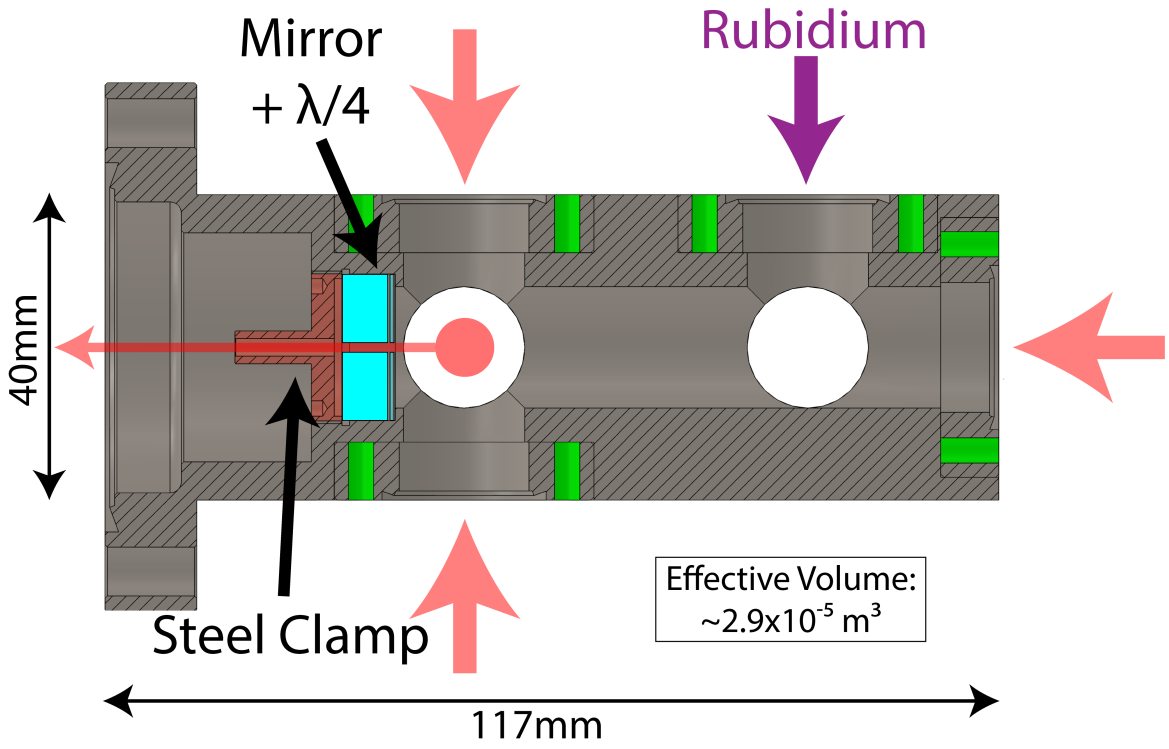

Fig. 3.9 Cross section view of the new LVIS chamber design. This design aimed to improve the Rubidium saturation within the LVIS chamber. Glass surfaces were kept to a minimum by subsituting the large glass cell for five DN16CF viewports. The clamp used to hold the mirror and waveplate was re-designed to be much smaller and manufactured from stainless steel. These changes allowed us to further reduce the size of the LVIS chamber, and therefore its internal volume, in an effort to improve the vacuum that we can achieve.

Holland. The new design eliminated the need to use indium or glue. It is designed to attach to the science chamber using a DN40CF port. Five DN16CF size optical ports provided the necessary optical access for the LVIS beams. This resulted in a much smaller chamber, with an internal volume $\sim$4 times smaller than the old design. Four threaded holes were also drilled around each viewport to make the chamber compatible with the Thorlabs 30 mm cage mounting system. This would make it easy to attach optical components directly to the chamber and also simplifying the alignment of the LVIS MOT beams. A stainless steel mirror clamp, which clamped the mirror and $\lambda/2$ plate in place was used to create a 2 mm channel through which the slow atoms would exit. In addition, two more DN16CF vacuum ports were incorporated - one for the vacuum pump that would be connected during baking, and another for the reservoir containing the rubidium sample.

The new LVIS chamber was successfully baked with the globe science chamber, and good UHV of $\sim 10^{-11}$ mBar was achieved. Interestingly, we were able to achieve a high saturation of rubidium in the LVIS chamber without the need to apply any heating to the rubidium reservoir, as is usually required. In Chapter 6, we discuss the saturation in detail and quantitatively assess the performance of our LVIS and its advantages over other LVISs from literature. Detailed schematics of the LVIS chamber design are provided in the Appendix.

3.5 Achieving Ultra-High Vacuum

"Baking" refers to the heating of a vacuum system, usually at 100-300°C, to accelerate the pumping process. Baking is essential to achieve UHV conditions, as, at room temperature, the rest gas is adsorbed to the chamber walls. A detailed review of outgassing of different materials, as well as methods for preparing vacuum parts and baking, can be found here [83].

Standard vacuum components come already clean and ready to be used in a UHV environment. For our set-up, several of the internal components were custom designed and manufactured in-house. This included several small steel parts like the LVIS mirror holder, the suspended prism holder and the accompanying screws. Before baking, care needed to be taken to ensure that all of the internal components were clean and free from any residue acquired during machining. For this purpose, the components were placed in a plastic container filled with acetone. The container was then placed in a heated ultrasonic bath for one hour, at 60°C. The container was then drained, and components were rinsed in tap water to remove the acetone.

The container was re-filled with distilled water, and the ultrasonic cleaning was performed for a further 60 minutes. The components were then dried and stored wrapped in aluminium foil.

Before baking an assembled chamber, firstly the internal steel components were pre-baked separately. This was done due to the fact that when baking the fully assembled chamber, the baking temperature is limited by the maximum temperature that the glass components could withstand. We pre-baked internal parts such as screws, prism holders etc. at a temperature of $\sim$250°C, to speed up the process when baking the fully assembled chamber at a lower temperature. The pre-baking was performed by placing the internal components inside a large, vacuum-sealed chamber which was attached to the pump via a flexible pipe. This prevented the parts from oxidising or otherwise reacting with the air during baking, while also removing the outgassing particles. Heating tapes were used to heat the sealed chamber. The vacuum pumping and baking set-up are illustrated in Figure 3.10.

After "pre-baking" the chamber was fully assembled. The insertion of the fused silica prism was performed inside a negative pressure enclosure to prevent any dust particles depositing on its surface. After the chamber was sealed, it was ready for baking. During baking, it was important to ensure that the glass viewports were heated uniformly, as they are prone to cracking from the heat. To protect the numerous viewports from cracking several layers of aluminium foil were wrapped over the glass surfaces. Foil was then wrapped around the rest of the chamber. This helped to ensure that the chamber was heated uniformly. Several thermocouples were attached to temperature-critical areas of the chamber, for monitoring.

A dedicated baking "oven" was designed and constructed for the purpose of vacuum bake out of the globe chamber. It comprised of a table-mounted breadboard, a heating element with a fan, and a frame around which thermal insulation was fitted. The baking oven allowed us to bake a whole vacuum chamber at once, without the need to use heating tapes. The fan ensured uniform heating of the chamber, which reduced the risk of viewports cracking.

The vacuum pump we used was a "HiCUBE" Turbo Pump. The chamber had to be pumped from both sides, due to it being a double-MOT system with only a narrow channel bridging the LVIS and the 3D-MOT sections. The chamber was designed with this in mind, with a dedicated valve positioned at each side.

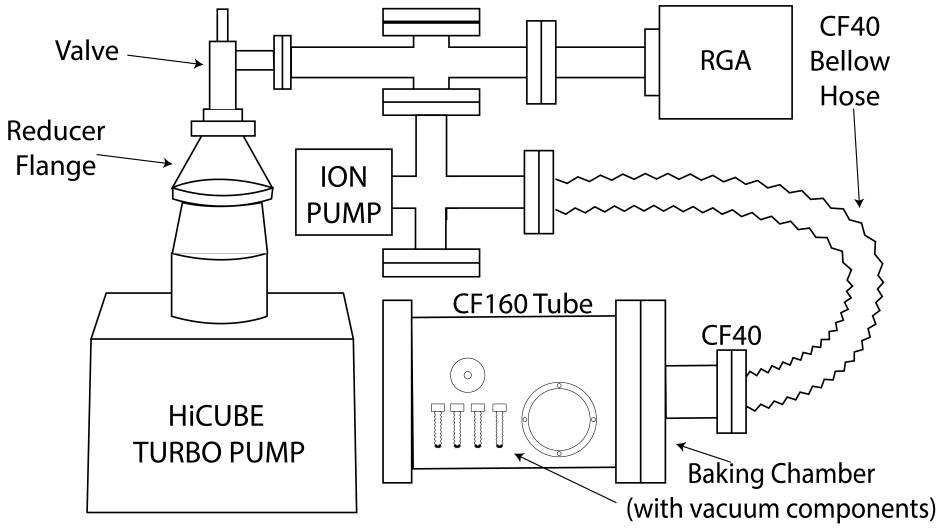

Fig. 3.10 Diagram illustrating the pumping and baking of vacuum components. The baking chamber was constructed using a CF160 Tube. The RGA and ion gauge were used to monitor the internal pressure.

The source of rubidium consisted of a Rb sample inside a glass cuvette. This was contained inside a steel tube and separated from the LVIS chamber via a valve, which was shut off for the duration of baking. Before baking, the ampule was broken under vacuum.

The temperature of the oven was slowly raised, to a final temperature of 200°C. An ion gauge and a residual gas analyzer (RGA) were used to estimate the pressure within the chamber during baking, and to check for leaks. After baking for 14 days, the heater was switched off. The vacuum was estimated to be $\sim 10^{-11}$mbar. The aluminium foil and insulation were left on for a full day, to allow the chamber to cool slowly and uniformly.

Chapter 4

Optical Set-up

4.1 Lasers and Frequency Control

A total of three different lasers were used in this experiment:

- A 1 W, 780 nm Quantel EYLSA (Erbium-Ytterbium) Fiber Laser was used to produce the cooling beams of the LVIS and 3D-MOT as well as the probe beam.
- A Moglabs 100 mW, 780 nm external cavity laser was used to produce the repumper beams.
- A 50 W, 1064nm IPG Photonics Ytterbium laser was used to produce the crossed Optical Dipole Trap (ODT) and the dimple beam. This particular laser was chosen due to its narrow linewidth (<50 kHz) and high output power. It produces a high-quality beam ($M^2 < 1.15$) with well-defined polarisation, single frequency and single-mode. These qualities provide high stability of the dipole potential in a crossed optical dipole trap, which is necessary for stable production of BEC.

Laser cooling of atoms is based on the resonant scattering of light at specific atomic transitions. This requires the laser frequency to be stabilised, by locking it to saturated absorption lines. This was performed through the use of Doppler-free saturated absorption spectroscopy. When a laser beam is passed through a Rb vapour cell, the resulting Doppler broadened spectrum can be observed using a photodiode. By reflecting the beam back on itself and passing it through the cell in the opposite direction, only the atoms with zero relative velocity in either direction will have the right frequency to interact. Using this method, the Doppler-free

absorption features can be observed superimposed on top of the Doppler absorption profile. The Rb Doppler-free absorption spectrum of the D_2 line is shown in Figure 4.1(a). This technique was developed in 1976 by Wiemann and Hänsch [84]. The process of frequency stabilisation is also described in detail in [85].

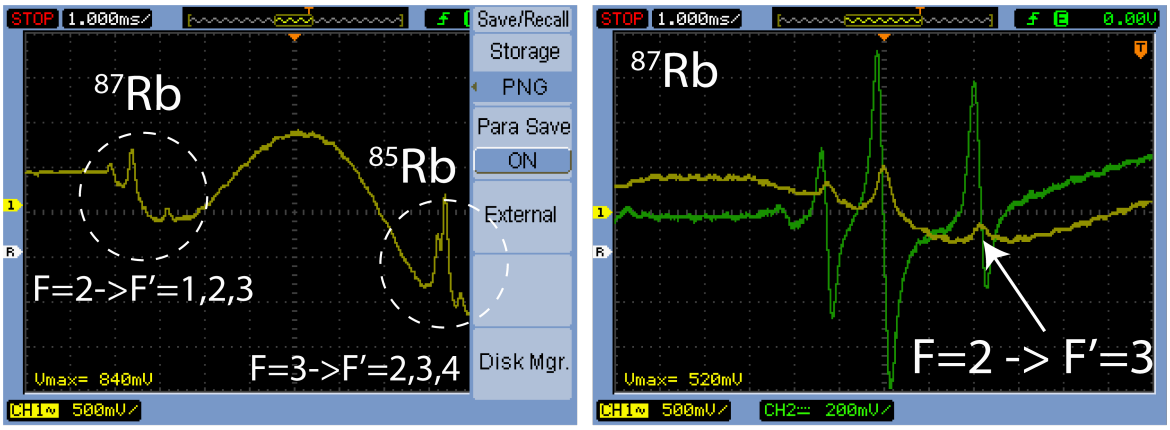

Fig. 4.1 Saturation absorption spectrum of the D_2 line of Rubidium. (a) Saturation absorption spectrum of the D_2 line of Rubidium, showing the broad Doppler peaks and hyperfine structure of ^{87}Rb $F = 2 \rightarrow F' = 1,2,3$ and ^{85}Rb $F = 3 \rightarrow F' = 2,3,4$ transitions. (b) Absorption spectrum (green) of the ^{87}Rb F=2 transition lines. The corresponding error signal is shown in yellow. The F=2 -> F'=3 line was used to lock the cooling laser.

For frequency stabilisation, a fraction of the laser output was passed through a Rb vapour cell. In our locking scheme, an electro-optical modulator (EOM) was used to apply small a small phase modulation to the beam. To avoid saturating the atomic transition, the intensity of the beam was attenuated to below 1.65 mW/cm^2. A mirror on a kinematic mount and a $\lambda/4$ waveplate were placed after the vapour cell to reverse the direction of the beam and to adjust the overlap. Finally, the signal from the return beam was observed using a photodiode. This saturated absorption spectroscopy provides an absorption spectrum free from Doppler broadening. The signal is measured by the photodiode and fed to the error input of the Vescent D2-125 lockbox. The reference signal is converted to a derivative-like "error" signal by the phase detector within the Vescent lockbox, and is monitored using an oscilloscope, using the "DC Error" output port, see Figure 4.1(b). An integrator circuit within the lockbox allows to lock to the zero-crossing electronically, and the servo output is used to control the frequency of the EYLSA laser. The cooling laser was locked to the F=2 -> F'=3 transition, while the repumping laser was locked to the F=1 to F'=1 - F'=2 crossover transition. The optical set-up for frequency stabilisation of the cooling and repumping lasers is illustrated in Figure 4.2.

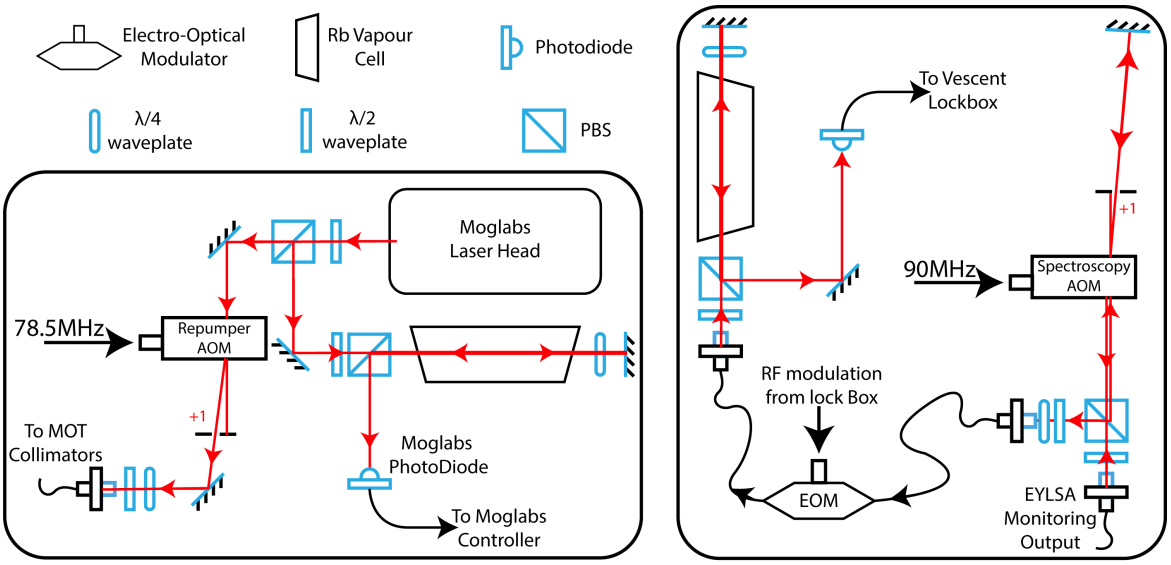

Fig. 4.2 (a) Optical set-up for locking the Moglabs laser and producing the repumping beam. The beam is passed through an AOM for frequency control and fast switching. A portion of the initial beam from the laser head is taken using a PBS for doppler-free saturation absorption for frequency locking. (b) Doppler-free saturation absorption scheme for locking the cooling laser.

An AOM in a double pass configuration was used to shift the frequency of the cooling laser by 80 MHz twice. This provides a total of 160 MHz shift from the laser emission frequency and a -20 MHz detuning to the red side of the cooling transition. The double pass is a convenient feature, as it allows us to change the AOM modulation frequency without misaligning the beam. Another AOM double pass was set up for the probe beam, providing a total shift of 180 MHz from emission and resulting in it being in resonance with the cold atoms. The utilised transitions for cooling, repumping and probing, as well as the AOM set-up, are illustrated in Figure 4.3.

4.2 MOT Distribution Board

The MOT distribution board had the purpose of splitting the output beam of the 1 W cooling laser into three pairs of beams that were then delivered to the science chamber via optical fibres to form the 3D-MOT. We used a fibre-coupled “OZ Optics” 3-way splitter to split the 3D-MOT master beam into three cooling beams of equal intensities. Each beam was then split into pairs using a PBS and $\lambda/2$ waveplate and coupled into individual optical

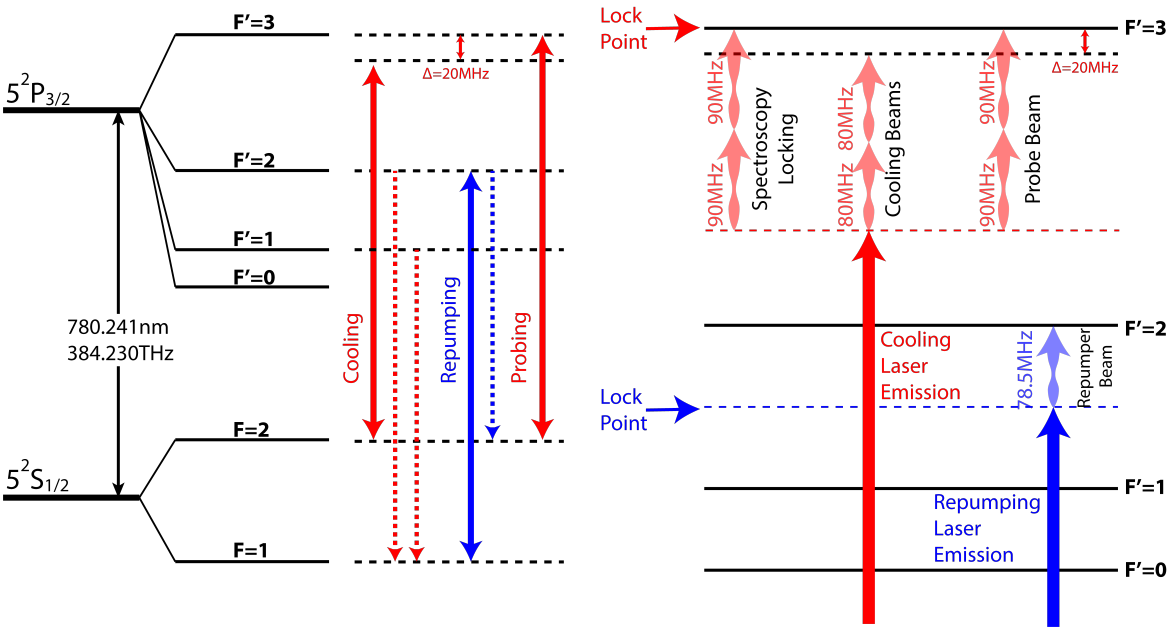

Fig. 4.3 (a) The ^{87}Rb D_2 line, showing the required cooling, repumping and probing transitions. (b) Zoomed in on the $5^2P_{3/2}$ hyperfine structure. A total of three AOMs, in double-pass configuration, were used to shift the frequency of the cooling laser for three different purposes: locking, probing and cooling. The repumper was locked over the F=1 to F'=1 - F'=2 crossover transition. An AOM was used to upshift the frequency by a further 78.5MHz to be in resonance with the F=1 to F'=2 transition.

fibres. This produced a total of six MOT beams, and the intensity balance of each pair was fine-tuned using the corresponding $\lambda/2$ waveplates. A set of $\lambda/2$ and $\lambda/4$ waveplates was placed at each fibre optic input in order to align the polarisation of the beam along the correct axis of the polarisation maintaining fibre.

Part of the initial beam was also used to produce the LVIS "master" beam and the probe beam. Double pass AOMs were used to shift the frequency of the cooling and probe beam according to the scheme shown in Figure 4.3. By using Thorlabs' "mini-series" components we were able to fit all of the optics for the MOT, LVIS and Probe beam distribution on a 45 x 45 cm optical breadboard. We refer to it as the "distribution board", and its optical set-up is illustrated in Figure 4.4.

4.3 LVIS Beam Distributor

The new LVIS chamber was designed to be compatible with the Thorlabs 30 mm cage system. Centred around each viewport were four 1/12" threaded holes, allowing for cage rods to be attached. This allowed us to construct and mount a 3-way beam distributor made entirely of standard Thorlabs components. As an added benefit, the distributor could be easily removed and re-attached as a single piece, while only requiring minor realignment of the mirrors. The LVIS beam distributor is illustrated in Figure 4.5.

The output of the LVIS optical fibre from the MOT distribution board carries the "master" beam. It is coupled into a collimator, producing a 15 mm beam. The beam is split using a PBS, with a 1:2 ratio using a $\lambda/2$ waveplate. The weaker beam is the "push" beam of the LVIS. The stronger beam is split into two more beams of equal power using a 50/50 beam splitter, forming the vertical and horizontal beams of the LVIS. The splitting is adjusted so that all three beams are roughly the same intensity. Finally, $\lambda/4$ waveplates are used to adjust the helicity of each beam. Both the vertical and horizontal beams are then passed through the LVIS chamber after which they are retro-reflected using mirrors mounted on kinematic mounts and attached to the opposite viewports using cage rods. The "push" beam is retro-reflected by utilising a mirror and $\lambda/4$ plate mounted inside the LVIS chamber. This mirror features a 2 mm hole in order to produce the "dark" channel through which a stream of slow atoms will propagate.

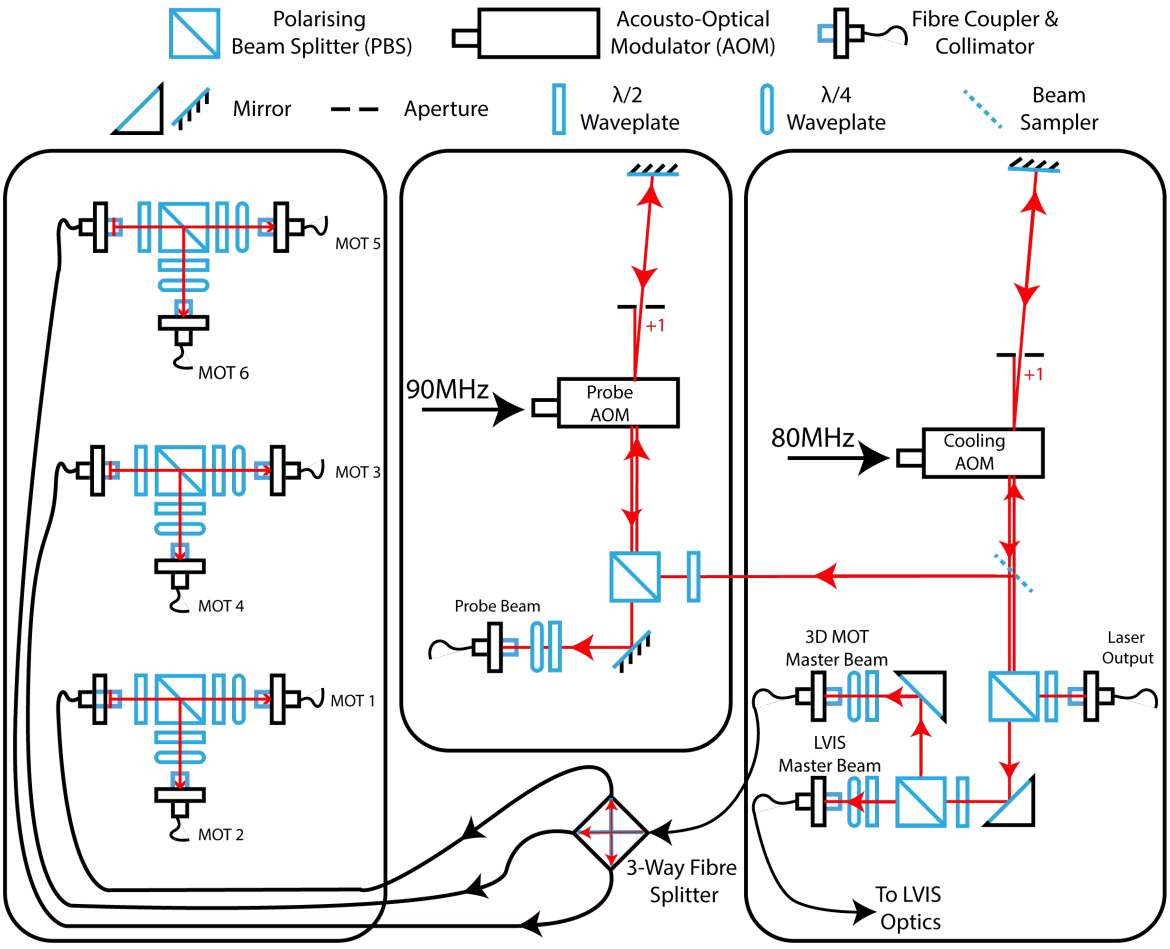

Fig. 4.4 Compact MOT distribution board. Miniature Thorlabs optics were used to set up the 3D-MOT and LVIS beams (right board). The master 3D-MOT beam is then further split into three pairs of beams, ready to be fibre coupled to the 3D-MOT collimators (left board). A small portion of the initial beam was taken using a beam sample and used to create the probe beam (middle board). The illustrated set-up is contained on a 45 x 45 cm board.

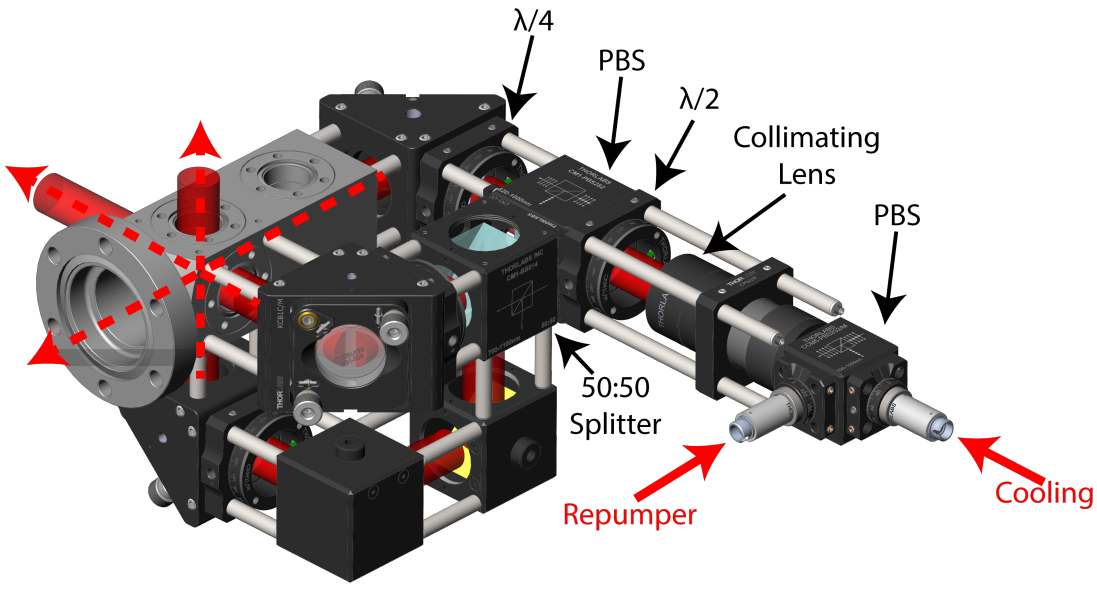

Fig. 4.5 LVIS Beam Distributor. The role of the beam distributor was to combine a fibre coupled cooling and repumper beam, split the beam into three separate beams of roughly equal intensity, and then to deliver the beams to the LVIS chamber. The repumper and the cooling beam were initially combined using a PBS. The combined beam was then collimated. A $\lambda/2$ waveplate and a PBS, followed by a 50:50 beam splitter were used to split the beams into three separate beams of roughly equal intensity. Finally, a $\lambda/4$ waveplates were used to adjust the helicity of each output beam. Two more sets of adjustable mirrors and $\lambda/4$ waveplates (not shown) were placed on the opposite sides of the two side viewports to retro-reflect the beams. The distributor was constructed using standard components from Thorlabs.

4.4 Main Optical Set-up

The vacuum chamber, MOT collimators, probe collimator, and optics for the dipole trap beam were set up on the main optical table along with the vacuum system. The MOT beams are delivered to the collimators from the MOT distribution board via optical fibres. The optical dipole trap is formed by a single beam, originating from the 1064 nm laser head. The beam is made to cross with itself at the centre of the MOT to create a crossed dipole trap. The beam is focused to a diameter of 140 μm using f = 250 mm doublet achromats (see later). The intensity of the final beam is then monitored using a photodiode which is used to stabilise the intensity of the dipole trap (see later). This optical set-up is illustrated in Figure 4.6.

4.5 MOT collimator designs

The MOT beams produced by the MOT distribution board were delivered to the main optical table via polarisation maintaining optical fibres. The fibres were then coupled into collimators designed to collimate and expand the beam to be 15 mm in diameter. A total of six collimators were set up for the 3D-MOT, as well as an additional one for the probe beam. One pair of the MOT collimators differed from the others by featuring two optical fibre inputs, and a PBS used to combine the cooling and repumping beams. These collimator designs are illustrated in Figure 4.7.

The beam profile of the 3D-MOT beams produced by the collimators was characterised using a Thorlabs linear CCD camera. This was done to ensure that we had good quality Gaussian beams with the expected diameter. The observed Gaussian profiles of the beams are illustrated in Figure 4.8.

The techniques used for aligning the 3D-MOT beams are described in detail in Chapter 5.

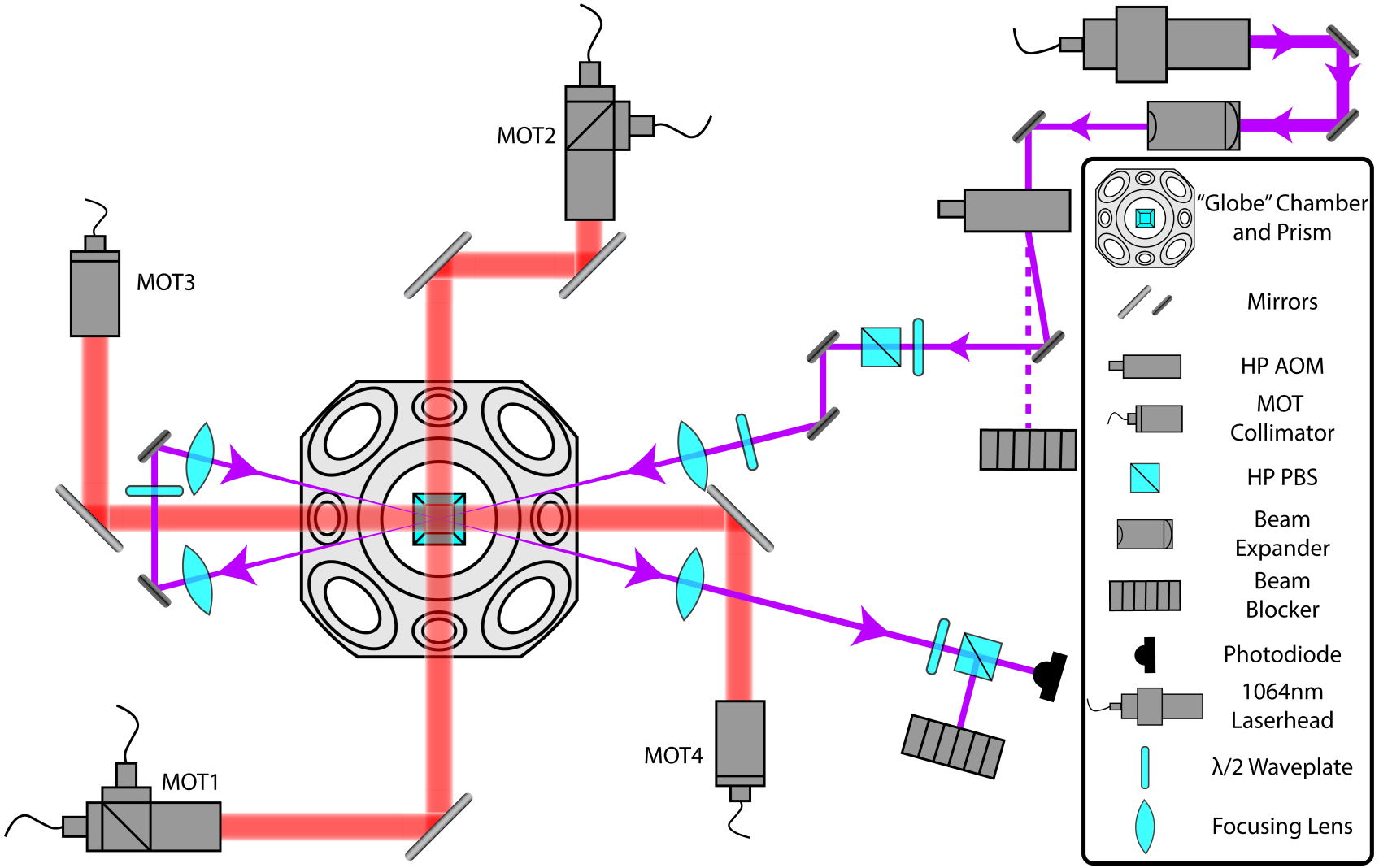

Fig. 4.6 Main Optical Set-up. The MOT beams are delivered to the MOT collimators via optical fibre from the MOT distribution board. Two of the vertical MOT beams, MOT5 and MOT6, are not shown. The repumping beam is delivered to MOT1 and MOT2 collimators via an optical fibre and combined with the MOT beam using a PBS. The centre of the MOT lies approx. 8 mm under the surface of the prism. The Optical Dipole Trap (ODT) is formed using a 1064 nm beam which originates from the laser head. It passes through a high power AOM, which is used to switch the beam on and off quickly. A PBS is used to "clean" the polarisation of the beam. The beam is crossed on itself to form a crossed dipole trap. $\lambda/2$ waveplates are used to ensure the polarisation is orthogonal to avoid potential fringes in the crossing region. Finally, the DT beam intensity is measured using a photodiode, which is used for intensity stabilisation (see later).

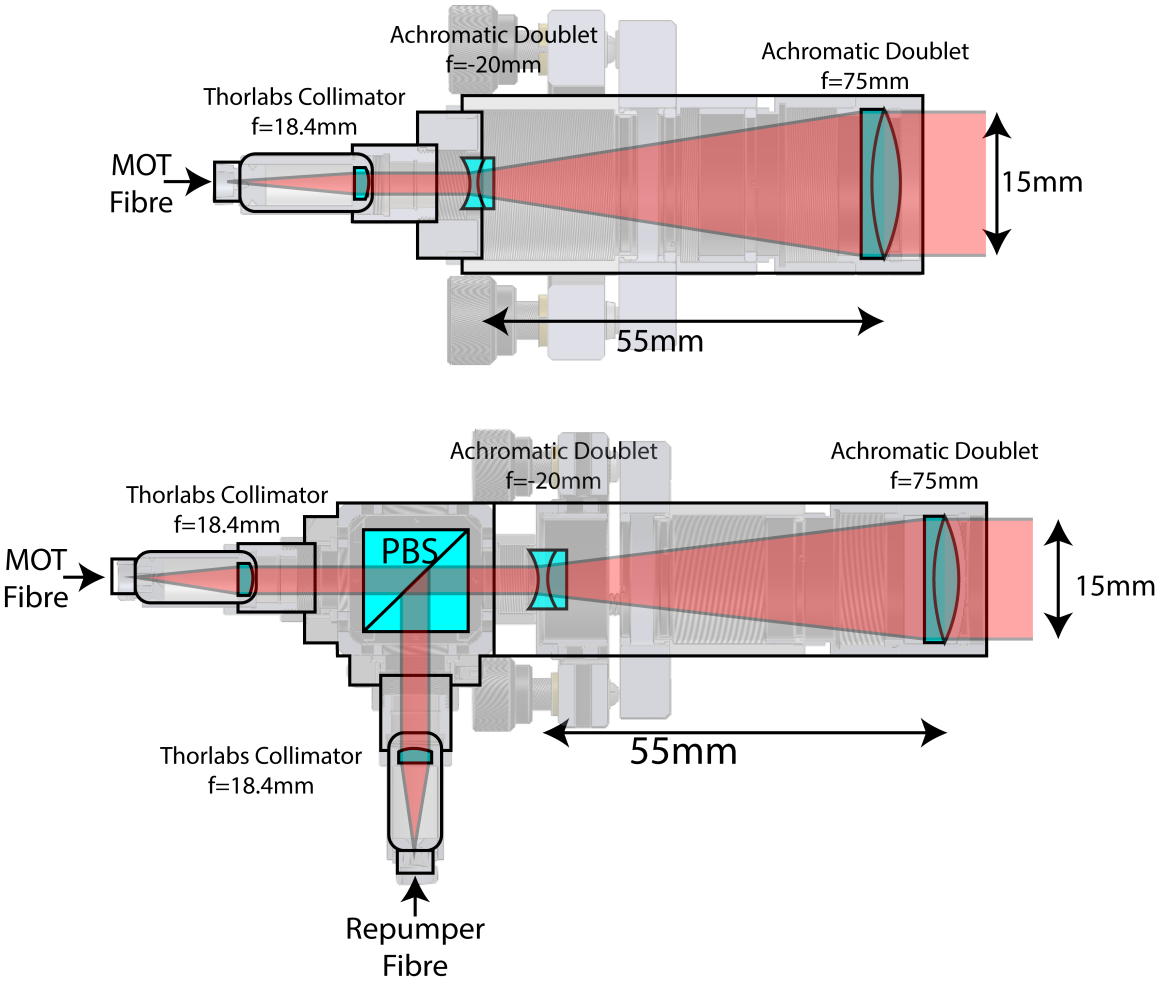

Fig. 4.7 MOT Collimator Design. Top: Collimator designed to produce a 15 mm beam. The beam is delivered via optical fibre, and subsequently expanded and collimated using two achromat doublets. Two pairs of 3D-MOT beams use this collimator design. Bottom: Collimator design for one pair of 3D-MOT beams and LVIS "master beam". This design is similar to the one pictured above but features a PBS which is used to combine the cooling and repumping beams, delivered via separate optical fibres. $\lambda/2$ plates (not shown) are used to maximise the beam intensity at the output.

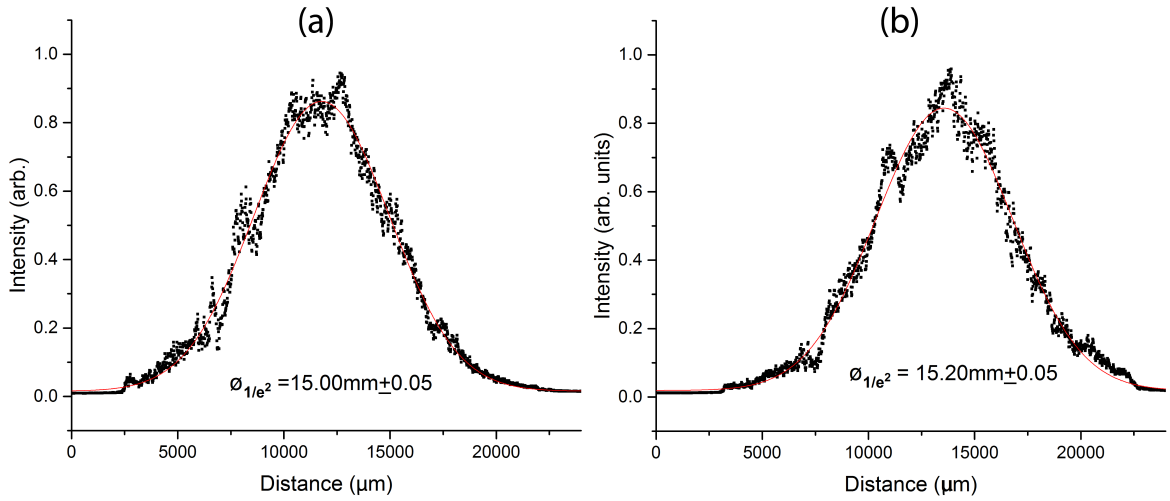

Fig. 4.8 Gaussian profiles of the collimated (a) MOT and (b) Repumper beams. The 1/e diameter is ∼15 mm as expected.

4.6 Crossed Optical Dipole Trap

In order to produce a BEC, we needed to implement an optical dipole trap. For this, we used a 50 W, 1064 nm laser. The optical set-up is illustrated in Figure 4.6. The beam was recirculated to cross with itself at ∼20°, to form a crossed dipole trap which offers a deeper potential and strong confinement in all directions of the trap. Out of the laser head, the beam was approximately 5.5 mm in diameter. A variable beam expander was used to reduce the beam to a mean diameter of ∼2.9 mm to ensure that it could be coupled to our high power AOMs that had an aperture of 3 mm. The beam was then passed through the AOM and finally focused using an f = 250 mm air-spaced doublet lens to a waist of 70 μm. The beam profile was imaged using a Thorlabs beam profiler to check the quality of the beam, as well as measure the waist of the optical dipole trap beam. Using Gaussian optics, we can calculate the expected spot size using:

$$2w_0 = \left(\frac{4\lambda}{\pi}\right)\left(\frac{f}{D}\right), \tag{4.1}$$

where f is the focal length of the lens and D is the diameter of the incident collimated beam. We calculate the theoretical spot size to be 47 μm. We could not establish the precise cause of this discrepancy. We eliminated some possible causes, such as thermal effects by conducting the measurement at a low power of a few mWs. One possibility is that the AOM aperture truncated the Gaussian beam, which would result in a larger spot, as expected from

diffraction. Alternatively, the larger than expected spot could be caused by the beam not being fully Gaussian. The dipole trap beam profile is presented in Figure 4.9.

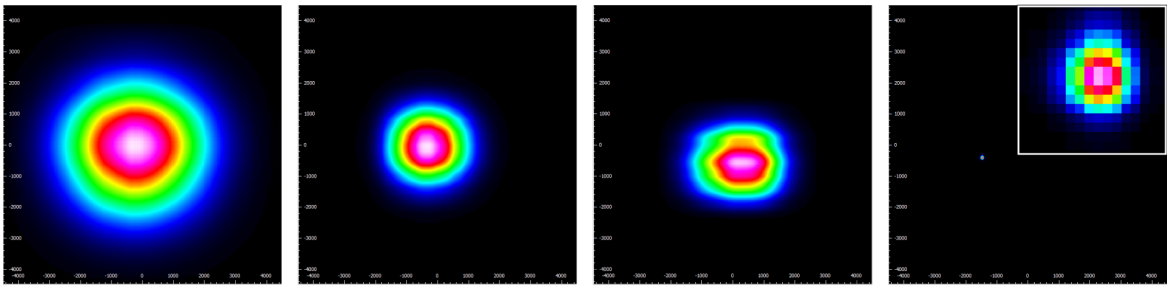

Fig. 4.9 Beam profile images of the 1064 nm laser taken using the Thorlabs beam profiler. (a) The beam imaged at the output of the laser head, diameter = 5444 μm. (b) Beam after expander, 2988 μm, (c) Beam after both AOMs, before being focused, 3050 μm. It can be seen that the beam quality has been reduced after passing through the optics. The coupling into both AOMs was fine-tuned to minimise these effects. (d) Focused optical dipole trap beam, 140 μm (zoomed-in view in top right).

4.7 Switching of beams using AOMs and shutters

In addition to frequency control, acousto-optical modulators (AOMs) were also used for fast switching of beams. The fast switching speed is critical when short pulses need to be used, for example, during probing. However, the extinction ratio of AOMs is rather poor, and some light always leaks through when switching the beams off. This can be destructive, since leaking resonant light will produce heating and knock the cold atoms out of the trap. To make sure that no leaking light reaches the science cell we used mechanical relay shutters for reliable beam blocking. They are however much slower than the AOMs. The shuttering speed was optimised by placing the shutter at the focal point of the beam where possible. For collimated beams on the distribution board, mechanical shutters were placed close to the input of the optical fibres to prevent any scattered light getting in when the beam is shut off. The shuttering speed of the AOMs and mechanical shutter was measured and is shown in Figure 4.10. The shuttering times had to be taken into account when composing the experimental sequence to allow for the needed times it takes to shut beams on and off.

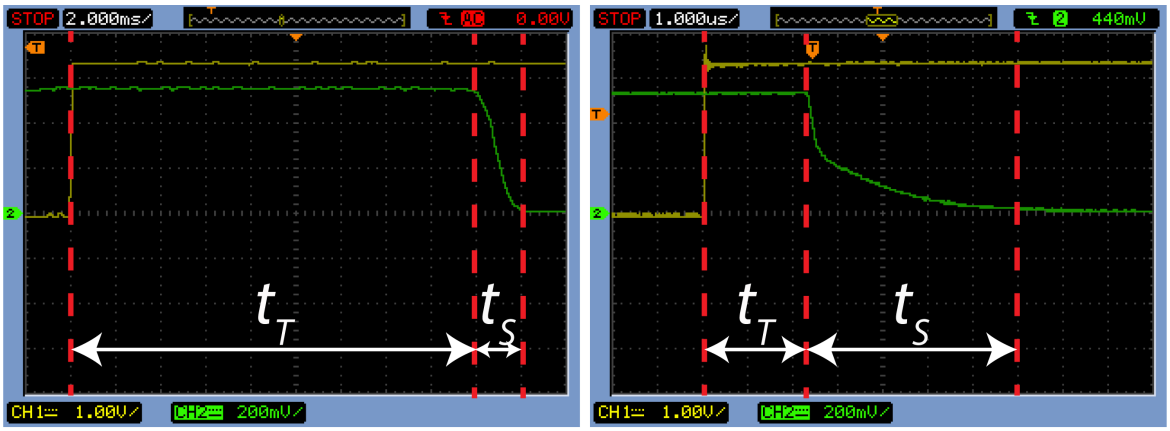

(a) (b)

Fig. 4.10 AOM and Mechanical Shutter response time. (a) Mechanical shutter. The intensity of the beam after the shutter (green signal) was monitored as the shutter was triggered (yellow signal). The triggering time (t_T) is 18 ms, while the shuttering time (t_S) is 2 ms. (b) AOM response time. The triggering time is 2.4 µs, while the shuttering time is ∼5 µs.

4.8 Detection Optics

A two-lens microscopic system was constructed and used to focus the image into the Andor iKon M 934 CCD camera. The CCD chip of this camera consisted of a 1024 x 1024 grid of square, 13 µm pixels. The microscope was formed by two lenses with a focal length of 250 mm and arranged to provide a 1:1 imaging ratio. The lenses used were 2" in diameter, "Thorlabs" achromatic doublet lenses. The minimum resolvable distance, also known as the diffraction limit, can be calculated using

$$d = \frac{\lambda}{2n\,sin\theta}, \tag{4.2}$$

where n is the index of refraction of the medium, and θ is the half-angle subtended by the objective lens. The calculated diffraction limit of our system is 4 µm.

The probe beam was coupled from the top of the chamber, with the focusing optics and CCD camera positioned at the bottom. The focusing optics 1:1 arrangement was verified by confirming that the probe beam was still collimated after passing through the microscope by using a shearing interferometer. Due to space limitations, the probe beam was positioned to make use of the same optics as the vertical MOT beams. The optical arrangement is shown in Figure 4.11.

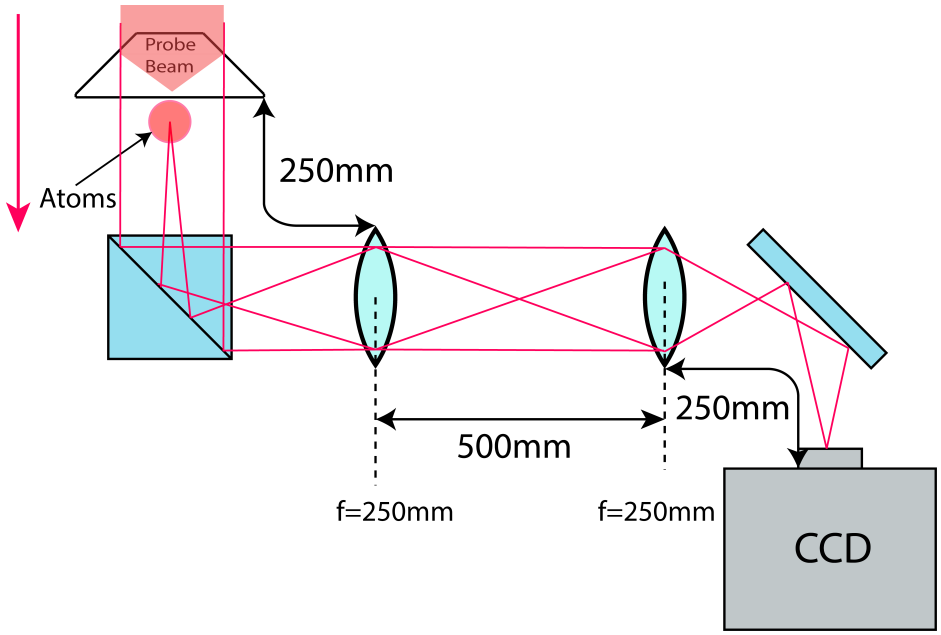

Fig. 4.11 Diagram showing the optical set-up for 1:1 absorption imaging. The CCD was mounted on a translational stage allowing for precise focusing of the image.

To obtain an accurate absorption image, (see section 5.5.2), it is essential that the probe beam is in resonance with the atomic transition of the atoms. We expect the probe beam to be at resonance when it is detuned by +20 MHz with respect to the cooling beams. The double-pass configuration of the probe beam, (see Figure 4.3), allowed us to change the frequency of the AOM without changing the alignment and the coupling efficiency of the beam. To confirm that the probe beam was at resonance with the atoms, we measured the total number of atoms detected via absorption imaging with respect to the detuning of the probe beam from the cooling beams. The relationship between the probe beam detuning and the number of detected atoms is presented in Figure 4.12. We expected to observe resonance at 20 MHz; however, we detected the most atoms at $\sim$17 MHz. This is likely due to some offset bias in the DDS frequency source.

4.9 Intensity Stabilisation and Pointing Stability

The intensity of the 50 W, 1064 nm laser was stabilised using an SRS SIM960 PID controller. After the dipole trap, a small portion of the exit beam was redirected using a beam sampler into a photodiode. The signal was then fed into the PID, and an external setpoint was set via the computer. The PID controlled the current into the dipole trap AOM in order to keep the

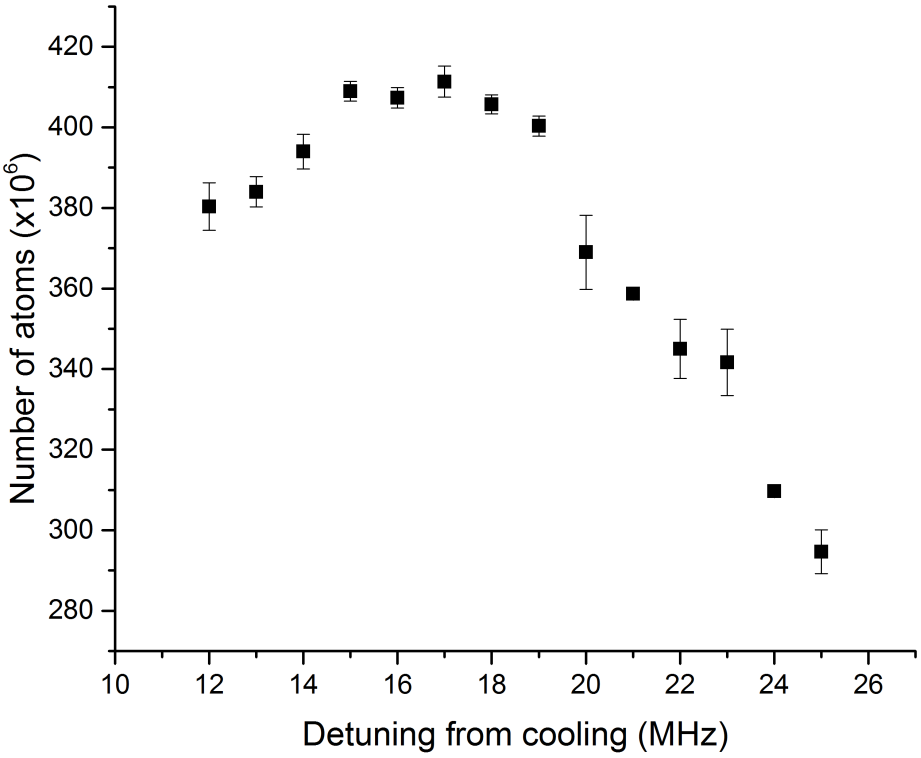

Fig. 4.12 Optimal probe beam detuning. Number of atoms detected via absorption imaging as a function of the detuning of the probe beam relative to the cooling beams. The highest number of atoms, (and therefore resonance), were found to be at $\sim$17 MHz.

intensity at the level of the setpoint. For the PID to do this efficiently, the gain, the integral and the derivative values had to be tuned. The trapping frequencies of the crossed optical dipole trap were calculated to be 12.5 kHz in the radial direction and 69.9 Hz in the transverse direction (due to the aspect ratio of the trap). It was, therefore, crucial to ensure that the intensity fluctuation noise was minimised close to these frequencies. The PID parameters were tuned by observing the signal at the photodiode using a frequency analyser. The PID values were tuned in order to minimise low-frequency intensity noise. This is crucial when performing evaporative cooling. A peak was observed at 50 Hz, from electronics of the diode. This can be avoided by using a battery-powered photodiode. No notable peaks were observed at frequencies past 50 Hz even without stabilisation, confirming that the IPG laser was stable.

The formation of a stable optical dipole trap also relies on the accurate alignment and pointing stability of the laser beam. Pointing stability refers to the measure of the positional drift of the beam over time. We observed the pointing stability of the dipole trap beam arbitrarily by monitoring the final beam position at approximately 1 metre away from the dipole trap using a Thorlabs beam profiler. The relative position of the beam was measured over the course of 60 seconds.

The sources of pointing instability include the laser itself, the sturdiness of the optical mounts, and vibrations originating from various devices in the lab. We attempted to further reduce the observed instability by introducing more support pillars that held the optical breadboards above the main optical bench. This reduced the flexion in the optical boards and improved the pointing stability of the dipole trap beam, as can be seen in Figure 4.13. This shows that while the Thorlabs 90x45cm boards have 5 dedicated mounting holes, it is beneficial to add further supports between the 5 designated ones. This acts to further reduce flexion and therefore improve the pointing stability of the beams.

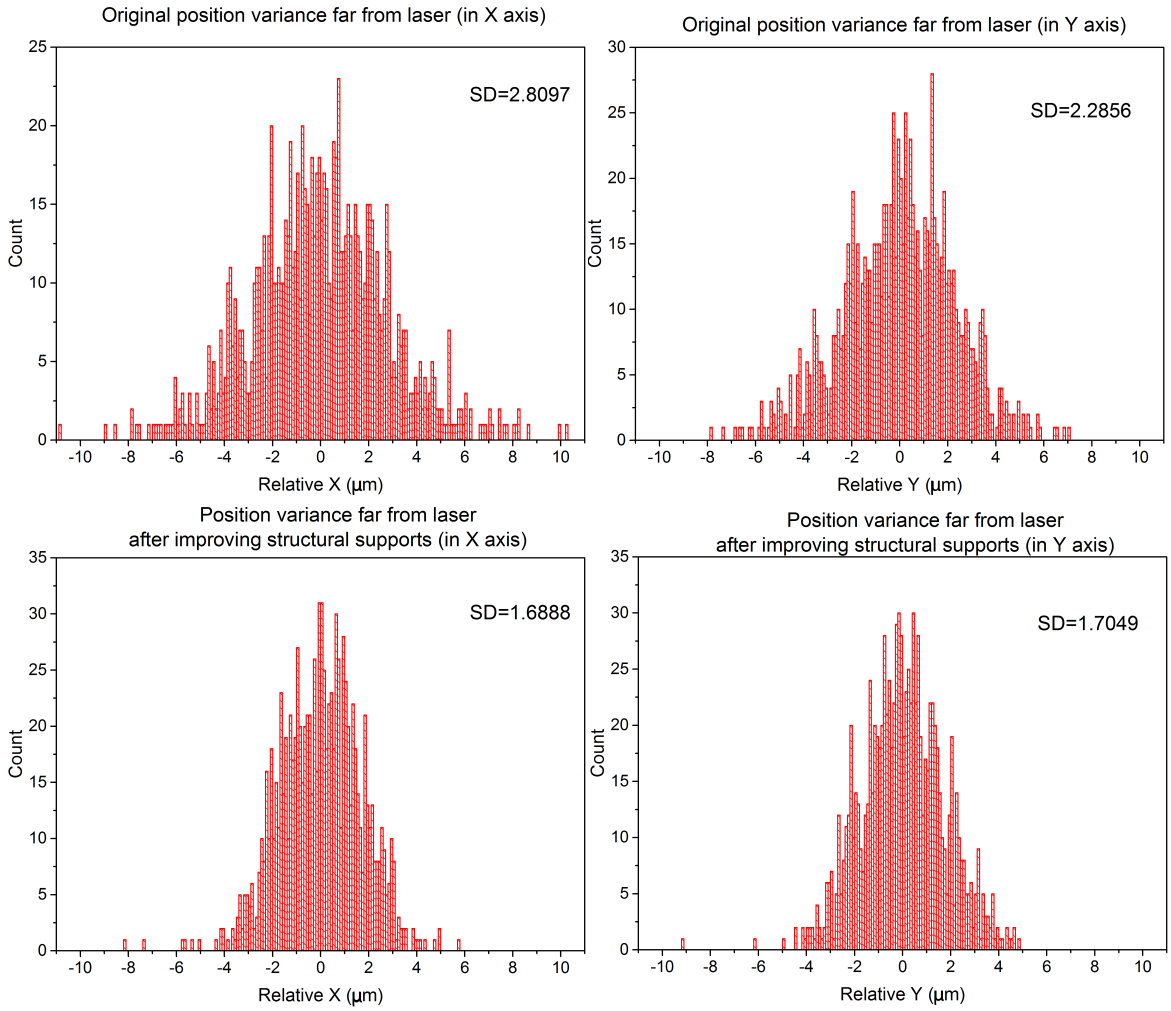

Fig. 4.13 Top: Position variance before, Bottom: Position variance after adding extra support pillars to the breadboards holding the optics.

Chapter 5

Experimental Techniques

This chapter describes the practical methods that were used to properly set-up the apparatus and perform detection of the cold atoms. We also describel the technique we developed and used to measure the velocity of atoms produced by our LVIS. While this technique is based on the usual time of flight method, it was modified to deal with the specific constraits of our set-up.

5.1 Beam Alignment

The 3D-MOT beam pairs needed to be overlapped with a high degree of precision as a small spatial misalignment can manifest as vortices within the molasses and produce heating. Each 3D-MOT collimator was mounted on a Thorlabs kinematic mount allowing for pitch and yaw adjustment. At approximately the half-way point between the collimator and the 3D-MOT each beam was also passed through a mirror on a kinematic mount, (see Figure 4.6). This configuration allows for maximum spatial control of the beam. To ease the alignment process, a pair of apertures were placed at the output of the collimators with the aim to reduce the diameter of the beams to $\sim$1 mm. At first, one of the beams was aligned with respect to the centre of the viewport of the chamber. The opposite beam was then superimposed with the first using the two kinematic mounts using an iterative process called “walking the beam”. The process was repeated for the other two pairs of 3D-MOT beams.

Aligning the vertical pair of 3D-MOT collimators proved the most challenging due to a lack of space between the collimators and the large vacuum chamber. Additionally, the top beam

needed to pass through the fused silica prism. If the beams were not precisely perpendicular with respect to the prism surface, this would result in unwanted aberrations and reflections inside the prism, especially since it lacked an anti-reflective coating. We exploited the lack of anti-reflective coating on the prism to aid in this alignment. The apertures were set up as before, but with the bottom beam initially blocked. A near-IR viewer and a piece of paper were used to look for a reflection of the beam from the top of the prism, back towards the top collimator. The position of the reflected beam was adjusted using the kinematic mount of the collimator until the incident and reflected beam overlapped, ensuring the beam path was normal with respect to the surface of the prism. This is illustrated in Figure 5.1. The same process was repeated for the bottom MOT beam. The bottom MOT beam was mounted on a 2-directional translation stage, which was then used to precisely overlap both beams.

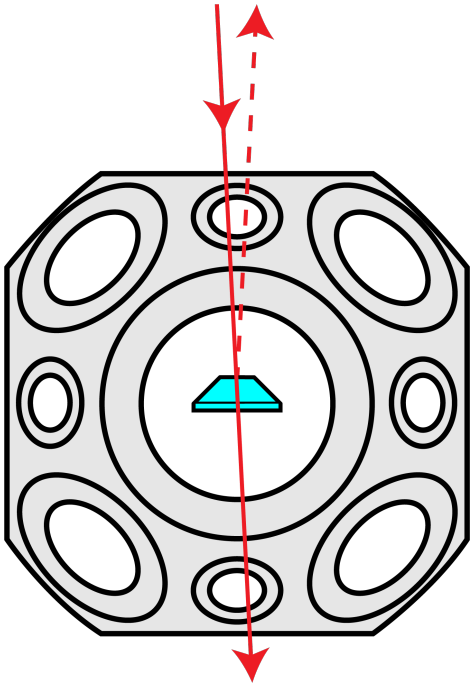

Fig. 5.1 Alignment of vertical MOT beams with respect of the prism. We ensured that the MOT beam paths were normal to the prism surface by looking for the faint reflection of the incident beam (indicated by the dashed line). The position of the incident beam was adjusted using its collimator until the reflected beam was superimposed with it. Performing this check was crucial to avoid aberrations and reflections that would arise if the beams were travelling through the prism at some angle.

5.2 Stray Magnetic Field Compensation

Atoms suspended in optical molasses are very sensitive to magnetic field gradients. It is therefore vital to compensate for any stray magnetic fields that could influence our atoms. This was performed by implementing compensation coils. The compensation coils comprised of three pairs of Helmholtz coils, one pair for each axis (x, y, z). Since the Earth's magnetic field is likely the largest contributor to the unwanted field, the vertical (z) direction was the strongest. Some other contributors could be electronics in the lab, magnets inside the ion pump and structural components of the building.

In order to fully compensate the magnetic field along all three axes, we used the following technique. First, the 3D-MOT intensities had to be checked with a power meter and balanced. This is an important step, as an imbalance in the cooling beams would "blow" the atoms in a direction, and could be confused with the effect of a magnetic field gradient. The 3D-MOT coils were turned off while keeping the cooling beams on. Provided that the flux of atoms from the LVIS is high enough, faint molasses form at the centre of the chamber. Two, live, near-IR Thorlabs USB CMOS cameras (Thorcams), positioned at 90 degrees with respect to each other were used to view the molasses from two directions. The coils compensating the vertical direction were adjusted first, aiming to centre the molasses with the centre of the chamber. The process was repeated using the other two coil pairs until the molasses appeared to be at the centre when viewed from both directions.

This preliminary adjustment provides only a rough approximation, as the molasses can be quite large and faint. To improve the alignment further, the following technique was used. The 2D-MOT coils were switched off. The 3D-MOT coils were turned back on and ramped to their maximum value. This shifted the MOT to the zero point of the quadrupole field, which coincided with the centre of the chamber. Substantially increasing the magnetic field gradient also reduced the number of atoms in the MOT, which allowed us to more accurately mark the position of the atoms on the images produced by the two Thorcams. The 3D-MOT field was then relaxed to the minimum value possible while maintaining a visible amount of the atoms. During this process, if the atoms moved away from the centre, the compensation coil values were adjusted to compensate. Since each adjustment of the compensation coil slightly changed the starting position of the 3D-MOT, this was an iterative process that had to be repeated 3-4 times.

5.3 3D-MOT and Bias Coils

Due to the size of the vacuum chamber, large spherical quadrupole coils had to be implemented for the 3D-MOT. Spaced apart by 28 cm, the pair of coils were wound with 950 turns of 1 mm copper wire. The power of the coils was 230 W, requiring liquid cooling. Cooling rings were mounted on the aluminium coil holders, and supplied with cooled water by a 300 W ThermoCube chiller.

The large proportions of the chamber also meant that it was rather difficult to get the 3D-MOT coils to be close to the true anti-Helmholtz configuration. It is desirable for the magnetic field gradient to be uniform, at least close to the MOT, to ensure efficient cooling. The magnetic field gradient was calculated to be ∼12 Gauss/cm, and the shape of the magnetic field is illustrated in Figure 5.2.

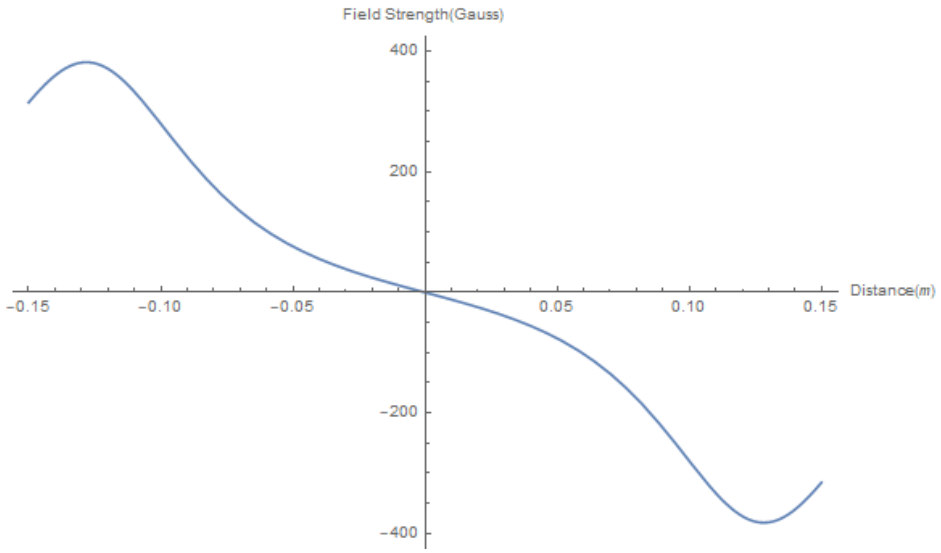

Fig. 5.2 Magnetic spherical quadrupole field produced by the 3D-MOT coils in the anti-Helmholtz configuration. The magnetic field gradient is ∼12 Gauss/cm and is linear near the centre of the MOT.

Due to the design of the chamber, the bottom surface of the prism needed to be at the centre of the chamber. Since the 3D-MOT coils were mounted on the large viewports, the centre of the "zero" magnetic field at which the MOT was to form was also at the centre of the chamber. This meant that in order to be able to form a MOT, we had to shift the magnetic field down by ∼7.5 mm. This was performed by introducing a pair of bias coils that applied a downwards magnetic gradient.

During the molasses stage of the sequence, it was crucial to switch all magnetic fields off at the same time. Due to the dramatic difference in size and power between the 3D-MOT and the bias coils, this was not straight forward to achieve. The 3D-MOT coils took considerably longer to fully switch off (∼20 ms), while the bias coils only took <100 µs. We decided to implement a fast-coil switching circuit, as presented in [86]. The circuit is shown in the Figure 5.3. After the implementation of the switching circuit, the ramping down of the bias coils was tuned to match the discharge curve of the large 3D-MOT coils. This allowed us to switch both coils in <10 ms simultaneously.

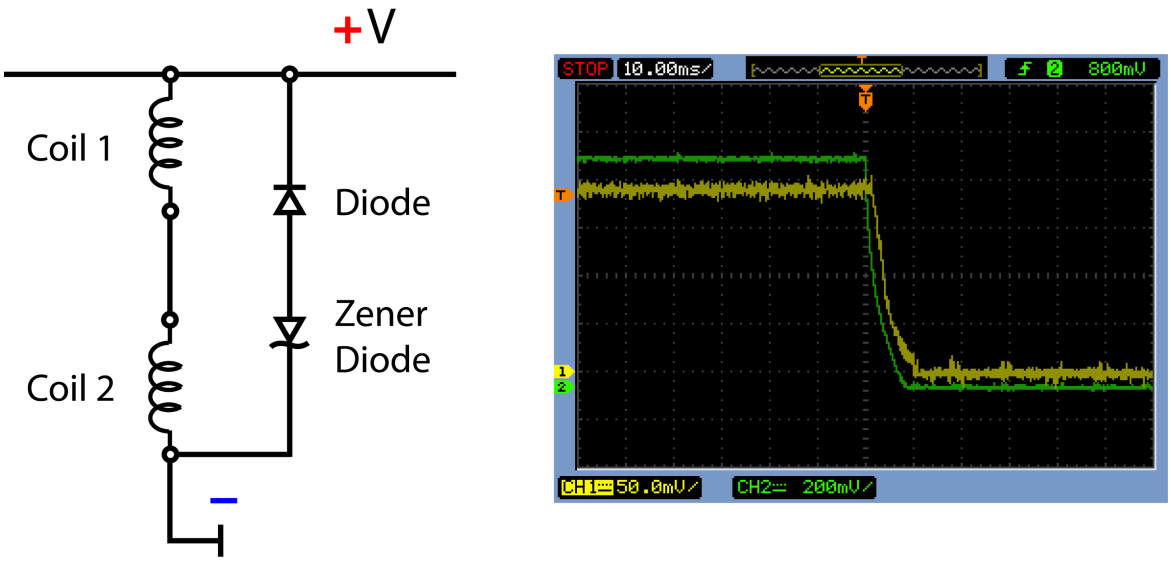

Fig. 5.3 Left: Fast coil switching circuit. Right: Current discharge curves of both coils matched to ramp down simultaneously in <10 ms.

While this technique seemed to work, we later decided to simplify the set-up by getting rid of the bias coils and merely shifting the position of the 3D-MOT coils down. This involved the manufacture of a new custom holder-adapter which allowed us to attach the coil to the chamber at a lower position.

All magnetic coils were controlled remotely from the computer. Ramping of the current is performed via an analogue RS232 connection at the power supply of each set of coils. For rapid switching off of the coils, solid-state switches were used. The switches were placed in series with the coils and were controlled by a trigger signal from the computer.

5.4 Coupling in Polarisation Maintaing Fibres

Polarisation maintaining fibres can stabilise the polarisation of the coupled beam, provided that the polarisation of the initial beam is correctly aligned with the fibre. This was performed using the following method:

1. The beam was coupled into the fibre, with good coupling efficiency (>60% power at the output)
2. A half-wave retardation plate was placed before the input collimator, while the output end of the fibre was monitored using the scheme in the figure below.
3. As the fibre was stressed, by gentle squeezing by hand, the polarisation inside the fibre rotated. We detected this effect as a fluctuation of power between the two ports of the photodetector, placed after a polarising beam splitter.
4. The position of the half-wave plate was adjusted in order to get minimum power fluctuations.
5. A quarter-wave plate was then added before the half-wave plate, and adjusted to reduce the fluctuations further.
6. To fine-tune the alignment, the process was repeated for several iterations, taking turns to make small adjustments to each wave plate until no further improvement on power stability could be made.
7. The coupling quality was then quantified using a Thorlabs Extinction Ratio (ER) meter. An ER of >20 was deemed sufficient for our needs.

5.5 Detection

5.5.1 Monitoring the MOT

Fluorescence and absorption imaging are the two workhorses for optical detection of cold atoms, with each having its own pros and cons. Fluorescence imaging is the simpler of the two and involves measuring the scattering of resonant light from the atom cloud. Commonly the resonant light is provided by the trapping lasers, and so, no dedicated probe beam is

required. This means the detector can be placed anywhere with a line of sight to the cloud, without needing optical access from the other side. The light intensity can be measured with a photodiode or observed with a webcam.

While this set-up is easy to implement, it is not ideal for imaging optically dense samples as only the fluorescence from the outer "shell" of the cloud reaches the detector without re-absorption. Two Thorlabs USB CMOS cameras were used to provide a live feed of the MOT, see Figure 5.4.

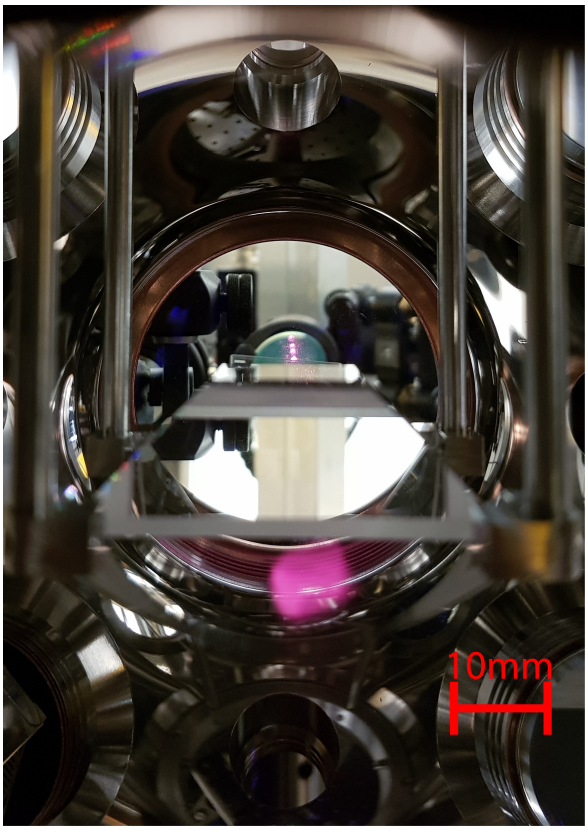

Fig. 5.4 Fuorescence of atoms trapped in the 3D-MOT, below the prism. The fluorescence is visible with the naked eye. Estimated number of atoms is 2×10^9.

5.5.2 Absorption Imaging

Absorption imaging involves firing a short pulse of resonant probe light at the sample of atoms. Due to absorption, the intensity of the probe light after the atom cloud will decrease

in accordance with the Lambert-Beer law:

$$I = I_0 e^{-OD}, \tag{5.1}$$

where I and I_0 are the intensities before and after the atom cloud. OD is the optical density and can be reperesented in terms of the column density n and the absorption cross-section δ:

$$OD = n(x,y)\delta. \tag{5.2}$$

The absorption results in a shadow, which is then imaged onto a CCD camera with the help of some focusing optics. We will refer to the first image as the "atom image". A second image is then taken of just the probe light without the atoms, which we will call the "light image". A third image is taken with all the beams off, producing the "dark image". The optical density of each pixel can then be calculated using the following formula:

$$OD_{meas} = ln(\frac{I_{light} - I_{dark}}{I_{atoms} - I_{dark}}), \tag{5.3}$$

where I_{atoms}, I_{light}, I_{dark} refer to the pixel counts of the atom, light and dark images respectively. The dark image is subtracted from the first two images to eliminate any dark currents produced by the CCD.

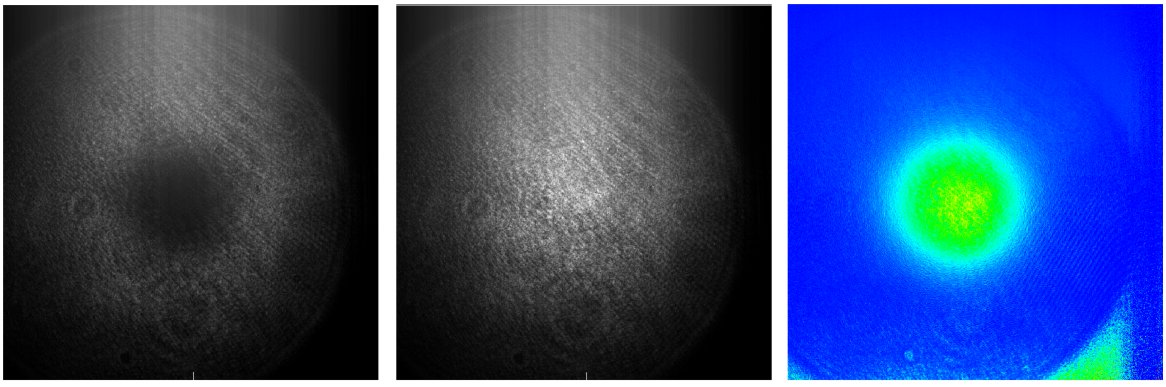

Fig. 5.5 Absorption imaging. (a) "Atom image", including the atom cloud (dark spot) and the probe beam. (b) "Light image" of the probe beam after the atoms are removed. (c) Final image computed by inputting the "atom", "light" and "dark image" (not pictured) into equation 5.3.

Performing this operation results in a shadowgraph image, from which one can directly extract the number of atoms. Hence, in contrast to fluorescence imaging, this technique can be considered self-calibrating. This process is illustrated in Figure 5.5. While absorption imaging produces a high signal to noise ratio, it is a destructive technique and hence requires a new atom sample to be produced for each image.

5.6 Time of Flight Temperature Measurements

The temperature of the cold atoms was determined using the typical time of flight (TOF) measurement [87]. This is performed by taking several images of the atom sample at increasing times of flight when all of the cooling and trapping lasers are off. This allows the cloud to expand freely, according to its velocity distribution.

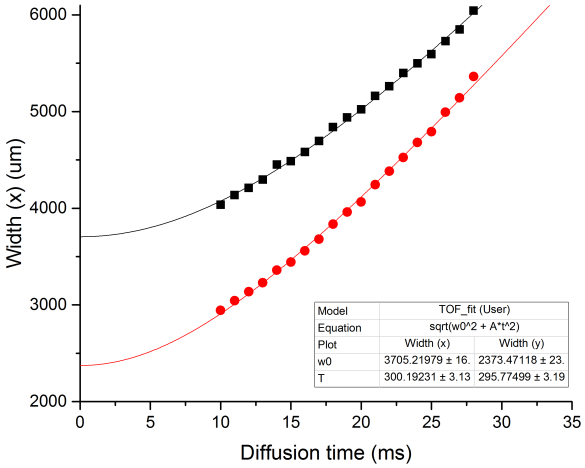

Fig. 5.6 TOF temperature estimate of atoms in the 3D-MOT. The temperature is calculated to be 300±3 μK and 296±3 μK in the x and y directions respectively.

The rate of expansion is measured in the x and y direction by fitting a 2D gaussian for each image of the cloud. Our probe and imaging system are aligned along the direction of gravity, z. This means we do not need to take the fact that the cloud is falling due to gravity into account. The rate of expansion is proportional to the temperature of the cloud as:

$$\sigma_{x,y}(t) = \sqrt{\sigma_{x,y}^2 + \frac{k_B T_{x,y}}{M} t^2}, \tag{5.4}$$

where $\sigma_{x,y}$ is the gaussian radius in the x and y directions, and M is the atomic mass. We can obtain an accurate measurement of the cloud temperature by plotting the Gaussian radius

of the expanding cloud over time, and then fitting the resulting curve with Equation 5.4. A typical TOF temperature measurement is illustrated in Figure 5.6.

5.7 Measuring the Velocity of Atoms from the LVIS

For a full calibration of the improved LVIS design, it is useful to know not only the flux of atoms but also their velocities. Slower atom velocities are favoured as they equate to a larger proportion of trappable atoms, resulting in faster loading rates and lower temperatures in the MOT.

For this measurement, a resonant "plug" beam was temporarily set up and aimed at the exit aperture of the LVIS. When the beam was on, it deflected the stream of atoms and prevented them from passing through the aperture in the retro-reflecting mirror. The beam was triggered using an AOM which provided us with an accurate on-off switch for the stream of cold atoms. The plug beam was 3 mm in diameter with a power of ∼30 mW.

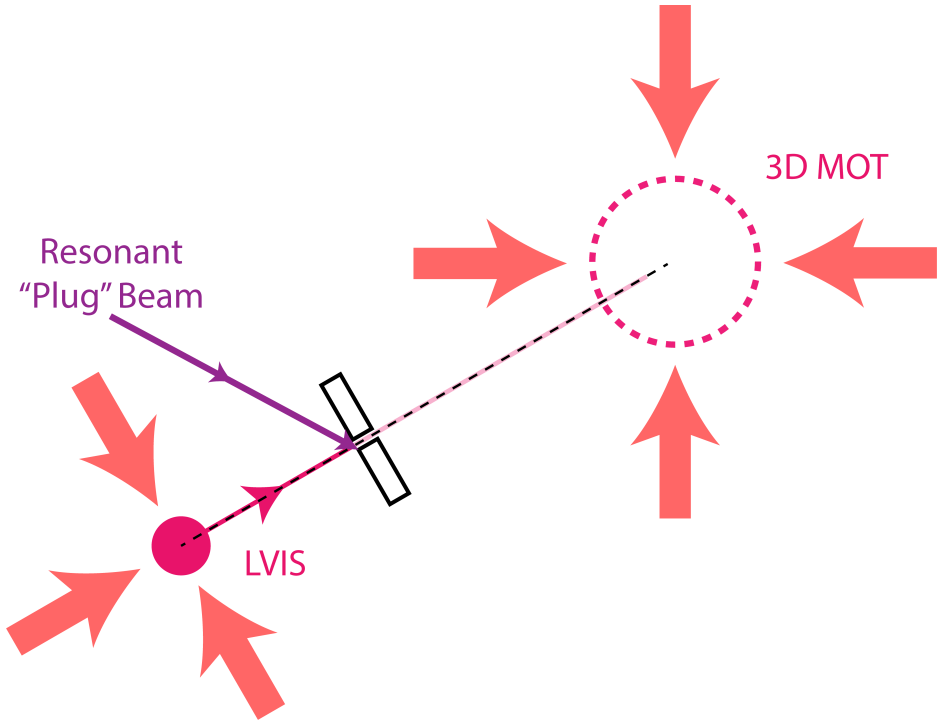

Fig. 5.7 Scheme for measuring the velocity of LVIS atoms. In this double-MOT system, atoms travel from the LVIS to the 3D-MOT. We use a resonant "plug" beam (purple) to shut off the beam of atoms from exiting the LVIS chamber, or to let them propagate and be loaded into the 3D-MOT. The loading of the 3D-MOT is monitored using a photodiode.

To measure the velocity profile of the atoms emitted by the LVIS, we developed a technique that is based on the time of flight method described in [78, 81]. In the usual method, atoms are released from the LVIS, and their fluorescence is detected using a resonant probe beam placed at some known distance, L, from the aperture of the LVIS. The effective velocity is calculated using the simple relationship $v = L/\tau$, where τ is the elapsed time between triggering the release of atoms from the LVIS and their subsequent detection. In our set-up, the fluorescence of atoms passing through a probe beam was too weak to be detected. This was due to the large size of our chamber, which meant that the photodetector could not be placed closer to the atoms, resulting in a very low signal to noise ratio. Instead of measuring the fluorescence of atoms passing through the probe beam, we instead loaded the atoms into the 3D-MOT. This provided a stronger signal which was much easier to pick up by our photodetector. Our scheme is illustrated in Figure 5.7.

Sequence Step	Duration (ms)
Load LVIS (3D-MOT is off)	1500
Turn on 3D-MOT	100
"Unplug" LVIS	7
"Plug" LVIS	100
Turn off LVIS and 3D-MOT	500

Table 5.1 Sequence for measuring the loading curve of the 3D-MOT from a short pulse of LVIS atoms.

The experimental sequence for obtaining the velocity data was as follows. Initially, the 3D-MOT beams were off to prevent the loading from background atoms. The LVIS was allowed to load while the plug beam was turned on to block the exit aperture. The 3D-MOT beams were then preemptively turned on, followed by a short, (7 ms), “off” pulse of the plug beam. This pulse duration was picked because it was the shortest pulse that allowed a small “train” of atoms to leave the LVIS. Shorter pulses tended not to allow enough time for the LVIS atoms to clear the plug beam before it was turned on again. The fluorescence signal was measured over time as the atoms were loaded into the 3D-MOT. The LVIS and 3D-MOT were switched off before rerunning the sequence. This sequence is summarised in Table 5.1.

We then needed to extract the velocity profile measurement from the “loading curve” obtained by plotting the fluorescence signal of the 3D-MOT over time. The loading curve tends to resemble a sigmoid curve, and is illustrated in Figure 5.8(a), which was obtained using the sequence described above. The distance, L, between the exit aperture of the LVIS and

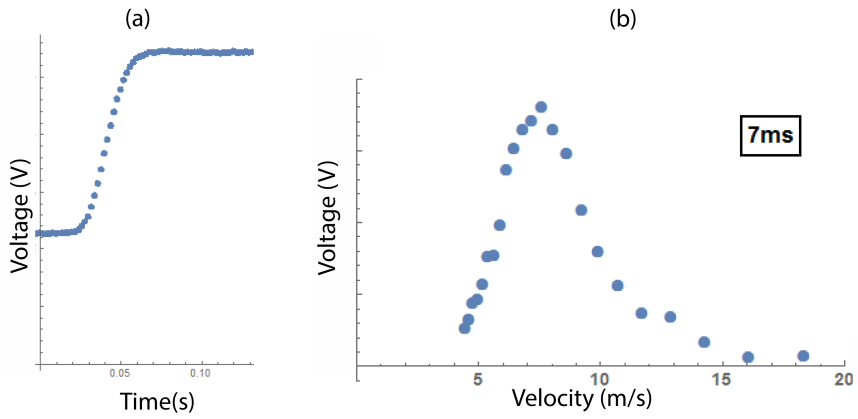

Fig. 5.8 Loading curve and velocity profile of LVIS atoms. (a) The loading curve obtained by measuring the fluorescence signal from the 3D-MOT while loading from the LVIS. The vertical axis provides an arbitrary scale for the number of atoms represented by the voltage of the signal picked up by the photodiode. (b) Velocity profile of the LVIS atoms loaded into the 3D-MOT, obtained from the derivative of the loading curve in (a). The derivative of the loading curve data was obtained using the "differences" function in Mathematica.

the centre of the 3D-MOT was 26 cm. We can transpose the time axis into velocity using $v = L/\tau$. Then, by finding the derivative of the sigmoid curve, we obtain a "bell" curve, which will be centred on the average velocity of the atoms. This was performed using the "differences" function in Mathematica for our data set. An example of the resulting velocity profile graph is presented in Figure 5.8(b). The results obtained using this technique are presented and discussed in detail in Chapter 6.

5.8 Loading of Crossed Optical Dipole Trap from Optical Molasses

Prior to attempting to produce a BEC through forced evaporative cooling, it is important to maximise the number of atoms that can be loaded into the ODT. The crossed optical dipole trap (ODT) was aligned to overlap with the centre of the MOT. The typical sequence used to load and subsequently image the ODT is described below and summarised in Table 5.2.

The MOT was loaded from the LVIS over 3 seconds, with the ODT on continuously. The 2D-MOT coils and the 2D-MOT bias coil were then switched off. After a 50 ms delay, the 3D-MOT coils were also switched off. Due to the large size and power of these coils,

Sequence Step	Duration (ms)
MOT Loading	3000
2D-MOT Coils off	50
3D-MOT Coils off	5
Eddy Currents Decay	10
Frequency Jump	10
ODT Loading	50
ODT Hold	100
Time of Flight	10
Pump to F'=3	0.5
Atom Image	250
Remove Atoms	200
Light Image	250
Light off	200
Dark Image	250

Table 5.2 Typical Sequence for Loading the Oprical Dipole Trap.

a waiting period of 10 ms was needed to allow for the eddy currents within the coils to decay. Switching off the 3D-MOT coils releases the atoms from the MOT. We then rapidly detune the frequency of the cooling light by 200 MHz from resonance over 10 ms, while also decreasing the intensity of the cooling and repumping light. The detuning is performed in order to place the atoms in a dark hyperfine state which reduces collisional trap loss and heating from rescattered light. This is known as a "dark" molasses and is analogous to the dark MOT [88]. The cooling and repumping light are kept on for an additional 50 ms at a reduced intensity, which we will refer to as the "ODT loading" stage. The repumping light is turned off 3 ms before turning off the cooling light, to ensure that the atoms are populating the F=1 state. The atoms are held in the ODT trap for a minimum time of 100 ms prior to detection to allow for the MOT cloud to fall out of the detection region. The ODT is then switched off, and the atoms are flashed with repumping light to pump them into the F'=3 state. The atoms are then detected using absorption imaging. The time between the ODT being switched off and subsequently imaged is referred to as "time of flight". During this time period there are no trapping forces acting on the atoms, and so the "cloud" falls due to gravity and expands depending on the temperature of the atoms.

Chapter 6

LVIS Characterisation

This chapter aims to quantify the performance of the new LVIS chamber design that I developed during my PhD. We initially experienced difficulties with rubidium saturation of the "old" LVIS chamber design, which was assembled for this project prior to my involvement, as discussed in Chapter 3. After investigating, we concluded that the "old" design was flawed in its use of large surface area internal copper parts, as well as glass. These materials tend to adsorb the free rubidium in the LVIS chamber, preventing its saturation. Other LVIS chamber designs also use internal copper parts; however, they are usually not as large, and the loss of free rubidium via adsorption is easily counteracted by applying heat to the rubidium reservoir. During the development of the new LVIS chamber design, we decided to test this further by minimising the surface area of the glass by using just the necessary amount of DN16CF viewports. We redesigned the way that we clamp the internal mirror (see Chapter 3), to further reduce the amount of surface area that can adsorb rubidium. Additionally, we made an effort to minimise the internal volume of the new LVIS chamber, to produce a better vacuum, less outgassing and better saturation of rubidium. In the final section of this chapter, we compare the performance of our design to other LVISs from literature.

6.1 Rubidium Vapour Pressure

Using a simple, single-pass absorption scheme, the absorption of a weak probe beam due to the presence of ^{87}Rb and ^{85}Rb vapour in the LVIS chamber was determined to be 22.3% and 45.0% respectively. The measurement was performed using a linearly polarised beam, with

an intensity of 82 $\mu W/cm^2$ at a temperature of 21.6°C, measured using a thermocouple. The effective length of the chamber was 40 mm. The absorption of the probe beam was measured for the ^{85}Rb $F = 3 \rightarrow F_e$ and ^{87}Rb $F = 2 \rightarrow F_e$ transitions, by measuring the maximum absorption of the probe when scanning the laser frequency through these transitions as a fraction of the overall signal. The frequency reference was provided by a separate Rb vapour cell. No effort was made to null the magnetic field of the lab. The rubidium sample that was used to populate the LVIS chamber with vapour contains both ^{85}Rb and ^{87}Rb in their natural abundances of 72.17% and 27.83% respectively[89]. For comparison, the absorption inside a 75mm Rb Vapour Cell was also measured to be 22.1% ^{87}Rb and 49% ^{85}Rb at the same temperature.

The absorption measurements were used to calculate the number density and vapour pressure of ^{87}Rb and ^{85}Rb in the LVIS and the Rb vapour cell using the Beer-Lambert Law[90]. For a beam travelling through a uniform medium of length L, the transmission is defined as:

$$\tau = \frac{I_{out}}{I_0} = exp[-\alpha L], \tag{6.1}$$

where α is the transmission coefficient. The number density, N, can be extracted from the transmission coefficient using $\alpha = N\sigma$, where σ is the microscopic atomic cross-section of the corresponding transition.

Additionally, we can estimate the vapour pressure using the following vapour-pressure model from Nesmeyanov's model [91]:

$$log_{10}p = -94.04826 - \frac{1961.258}{T} - 0.03771687 \times T + 42.57526 \times log_{10}T, \tag{6.2}$$

where the pressure is given in Torr and temperature in K. From the vapour pressure, we can calculate the number density of rubidium atoms using:

$$N = \frac{p \times 133.323}{k_B T}, \tag{6.3}$$

where the vapour pressure is in Pa and 133.323 is used to convert the pressure from Torr to Pa. The relative abundances of ^{85}Rb and ^{87}Rb must be taken into account when calculating the vapour pressures. Our experimental measurements of the number densities of Rb and vapour pressures and calculated values from Nesmeyanov's model are presented in Table 6.1.

	Number Density (atoms/cm^3) ^{85}Rb	Number Density (atoms/cm^3) ^{87}Rb	Vapour Pressure (Torr) ^{85}Rb	Vapour Pressure (Torr) ^{87}Rb
Nesmeyanov Model	4.9×10^9	1.8×10^9	1.5×10^{-7}	5.8×10^{-8}
Rb Vapour Cell	7.2×10^{10}	2.4×10^{10}	2.2×10^{-6}	7.3×10^{-7}
LVIS	1.2×10^{11}	4.65×10^{10}	3.7×10^{-6}	1.4×10^{-6}

Table 6.1 Comparison of experimentally measured number densities and vapour pressures in our LVIS and a standard Rb vapour cell, as well as the theoretical values obtained from Nesmeyanov's formula. T=294.75 K (21.6°C) was used during all measurements.

We observed a higher total pressure of Rb vapour in the LVIS than in the Rb vapour cell by a factor of 1.7. We suspect the increased pressure in our LVIS is due to the different chemistry of Rb atoms which occurs at the surface of different materials. The chemical reactions of Rb atoms at the walls of the chamber prevent the chamber from being completely saturated. Copper, which is widely used in UHV systems, seems to be the worst case. This is confirmed by our experience with the initial LVIS design, in which a large surface area copper clamp was used to hold the internal mirror in place. Glass is better than copper but worse than stainless steel. The Rb vapour cell is made entirely out of glass. The LVIS chamber was constructed entirely out of stainless steel, including the mirror clamp. We also opted to use the minimum size of viewports (DN16), which minimised the glass surface area. These factors add up to produce a higher pressure of Rb atoms even without additional heating of the Rb reservoir.

6.2 Velocity Profile of LVIS Atoms

The velocity profile of the LVIS atoms was obtained using the technique described in section 5.7. The average velocity of the non-thermal LVIS atoms was determined to be 7.8 ± 0.5 m/s, which is in agreement with [82].

We also calculated the expected velocity of atoms in the LVIS using a simple, two-dimensional theoretical model presented in [82]. The model is based on a two-level model of the atom and assumes that the beams of the LVIS are of equal intensities and in a symmetrical arrangement. The motion of an atom in the trap is described by the corresponding dissipative force. In a typical LVIS, the push beam is retro-reflected by a mirror with a hole, producing a dark channel. This means that the trapped atoms which enter that channel experience only the

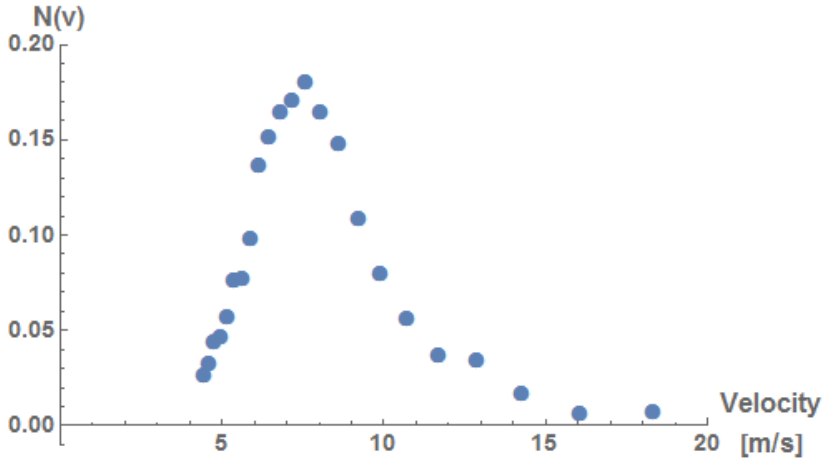

Fig. 6.1 Velocity Profile of Atoms from LVIS. The LVIS was unblocked for a duration of 7 ms, while monitoring the population of the 3D-MOT. This velocity profile was obtained by taking the derivative of the initial loading curve of the 3D-MOT. This method is described in detail in section 5.7.

force due to the"push" beam, and are accelerated through the hole. The calculated velocity distribution of a beam of 500 slow atoms extracted from the LVIS is illustrated in Figure 6.2. The calculated value of 8 m/s is in excellent agreement with the velocities we measured experimentally.

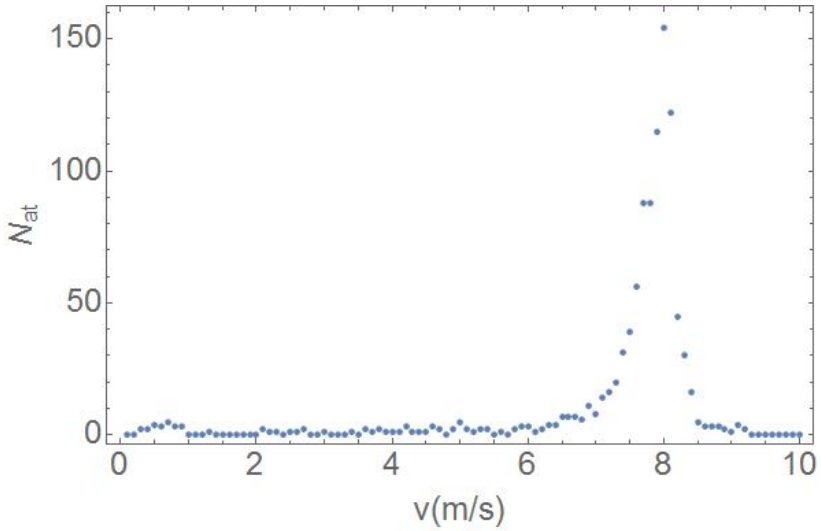

Fig. 6.2 Calculated Velocity Profile of Atoms from LVIS. The expected velocity of extracted atoms is ∼8 m/s.

6.3 Atomic Flux and Loading Rate of 3D-MOT

Another useful quantitative measurement of LVIS performance is the loading rate of the MOT. A "loading curve" was obtained by plotting the number of atoms in the 3D-MOT as a function of loading time. The number of atoms in the MOT was measured using absorption probing for the initial loading time of 300 μs and extrapolated to 10 seconds using fluorescence imaging. Fluorescence imaging had to be used for longer loading times as the MOT became larger than the field of view of the CCD camera used for absorption imaging. The atomic flux of trappable atoms from the LVIS was determined from the gradient of the loading curve to be 7.5×10^9 atoms/s, see Figure 6.3(a). The high flux of atoms allowed us to load a large MOT of 9×10^9 atoms in just 1.7 seconds.

The lifetime of the atoms in the MOT was measured by firstly loading the 3D-MOT as usual and then switching off the LVIS. The number of atoms in the 3D-MOT was then measured using fluorescence imaging over time. The 1/e lifetime was measured to be $\sim$18 seconds. The lifetime can be a good indicator of the vacuum conditions inside the chamber, as collisions with background atoms are one of the mechanisms by which atoms can leave the MOT. However, the lifetime of the MOT is also highly dependent on the balance of the MOT beam intensities. Even a small imbalance within a pair of the beams can slowly "push" atoms out of the MOT. Since we use a total of six independent beams to create the MOT it is likely that our measured lifetime is short due to the intensity imbalance rather than poor vacuum.

The 3D-MOT temperature was measured using the TOF technique using absorption imaging. The temperature of atoms trapped in the 3D-MOT was measured to be $298 \pm 3\mu$K. The average temperature of the atoms in optical molasses after the dark molasses stage was measured to be $35 \pm 4\mu$K.

For a complete characterisation of the LVIS, we were also interested in measuring the flux of thermal atoms out of the LVIS. This was performed by shutting off the LVIS beams completely and loading the 3D-MOT as normal. The number of atoms in the 3D-MOT was measured via fluorescence and recorded as a function of loading time, see Figure 6.4. The flux of trappable thermal ^{87}Rb atoms is approximated, from the gradient of the plot, to be 28×10^6 atoms per second. This is a rather high flux and provides additional evidence of the high vapour pressure of Rb in the LVIS. It should be noted that this estimate only accounts for the trappable portion of thermal atoms.

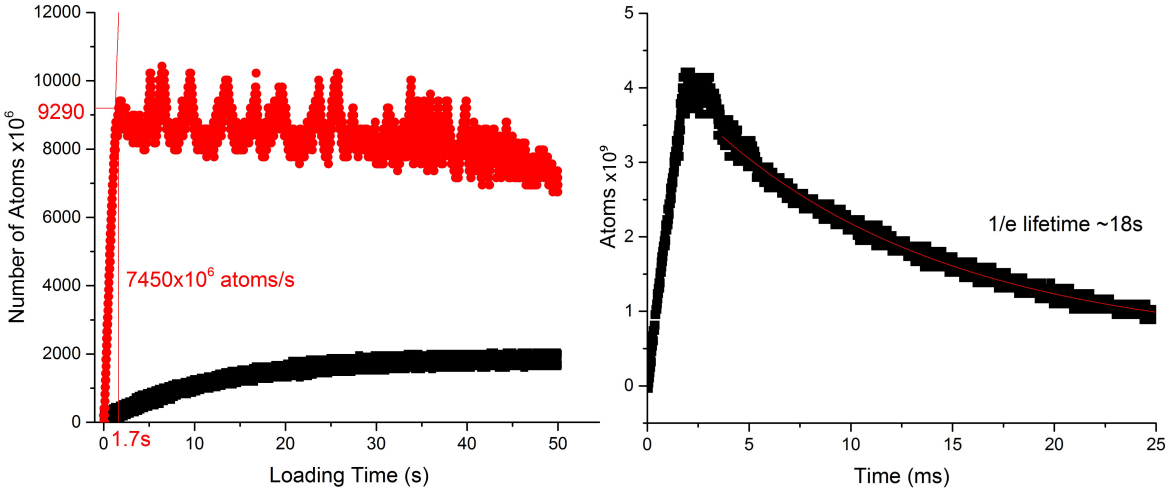

Fig. 6.3 Left: Loading of the MOT from the compact LVIS source. The trap was loaded in 1.7 seconds with 9.3×10^9 atoms (red). The initial loading rate was 7.5×10^9 atoms/s. The black curve represents the loading rate without the pushing beam of the LVIS. This was performed to calibrate the fluorescence signal received by the photodetector with the number of atoms measured by absorption. Right: Lifetime of atoms in the MOT when the LVIS source is switched off. 18 seconds is rather short, which can be attributed to an imbalance of MOT beam intensities. The short lifetime is not due to poor vacuum, since sufficiently long lifetimes were observed in the optical dipole trap.

Finally, we compare the performance of our LVIS against other LVISs found in the literature [78, 92, 81, 82] . This is presented in Table 6.2. From the table, we note that the high flux and low velocity of the atoms produced by our LVIS is on par with the next best performing LVIS reported in [82]. However, we were able to achieve this performance using just half of the laser power. Additionally, as discussed previously, our LVIS does not require heat to be applied to the rubidium reservoir to maintain the required rubidium pressure. These features make our design particularly valuable in applications where power consumption and heat need to be kept to a minimum, such as onboard of a satellite.

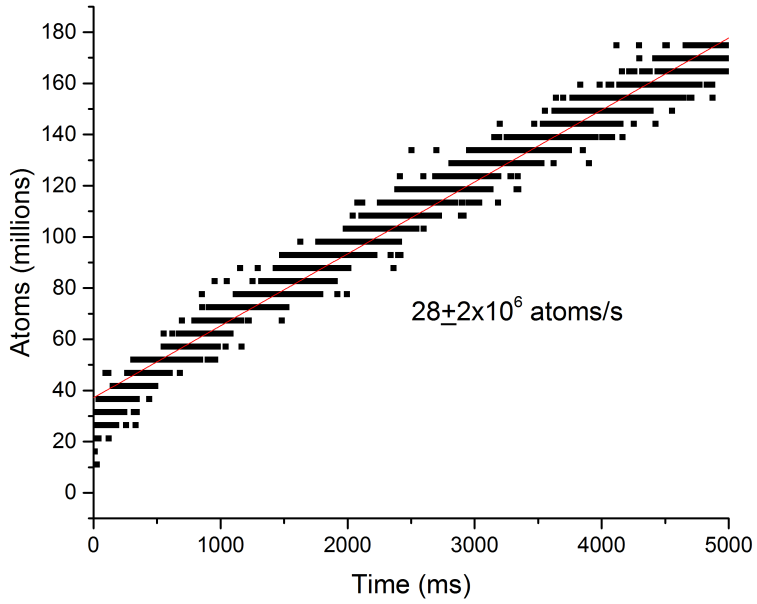

Fig. 6.4 Measurement of the Thermal Atom Flux from the LVIS. The LVIS beams were turned off, and the 3D-MOT was loaded with just the thermal atoms. The graph shows the number of atoms detected in the 3D-MOT (vertical axis), as a function of loading time. The flux of trappable thermal atoms is determined to be $28 \pm 2 \times 10^6$ atoms per second.

Work	Z.T. Lu et al [78]	R.S. Conroy et al [92]	K. Dieckmann et al [81]	Yu.B. Ovchinnikov [82]	Present Work
Total laser power (mW)	500	200	27	60	30
Laser beams diameter (mm)	40	35	14	25	14
Velocity of cold atoms (m/s)	14	15	26	8	8
CW flux (at/s)	5×10^9	8×10^9	3×10^7	8×10^9	7.5×10^9

Table 6.2 Performances of other LVISs from literature, as well as the one presented in this work.

Chapter 7

Optical Dipole Trapping

In this chapter, we discuss the performance of the crossed-optical dipole trap and our attempt at evaporative cooling using the newly constructed apparatus as discussed in prior chapters. This stage of the experiment is similar to the work I did in the first year of my PhD alongside another PhD student, Richard Moore in the "old lab", prior to my move to the "new lab". In the old lab, we were able to produce the first BEC at NPL, using Rubidium atoms via all-optical evaporation in a crossed-dipole trap. This achievement is documented in the thesis of R. Moore [63]. Due to the similarity of the trapping schemes across both labs, we will be referring to the performance of the dipole trap and evaporation to BEC in the old lab, from the thesis of R. Moore, as a comparison to the results obtained in the new lab.

7.1 Realisation of the Crossed Optical Dipole Trap

The ODT was formed by a 1064 nm beam, focused to a waist of 70 μm from an initial beam diameter of 2.9 mm, as described in section 4.6. The waist of the beam was overlapped with the centre of the chamber by the use of the translation stage to which the doublet lens was mounted. After passing through the chamber, the beam was again collimated, focused and reflected back into the chamber with an orthogonal polarisation to produce a crossed ODT. The crossing angle of the initial and return beam was $\sim 22°$, the same as in the old lab. The trap was roughly overlapped with the centre of the MOT. Exact overlap was unnecessary as the MOT is much larger than the ODT. The power of each beam was $\sim$20 W, corresponding to

a peak potential depth of $U_0 = 809\ \mu K$, and calculated radial and axial trapping frequencies of 1.25 kHz and 217 Hz respectively.

Atoms were successfully loaded from molasses into the crossed ODT, using the loading procedure described in section 5.8. We were able to trap 1.8×10^6 atoms in the crossing region of the ODT, see Figure 7.1.

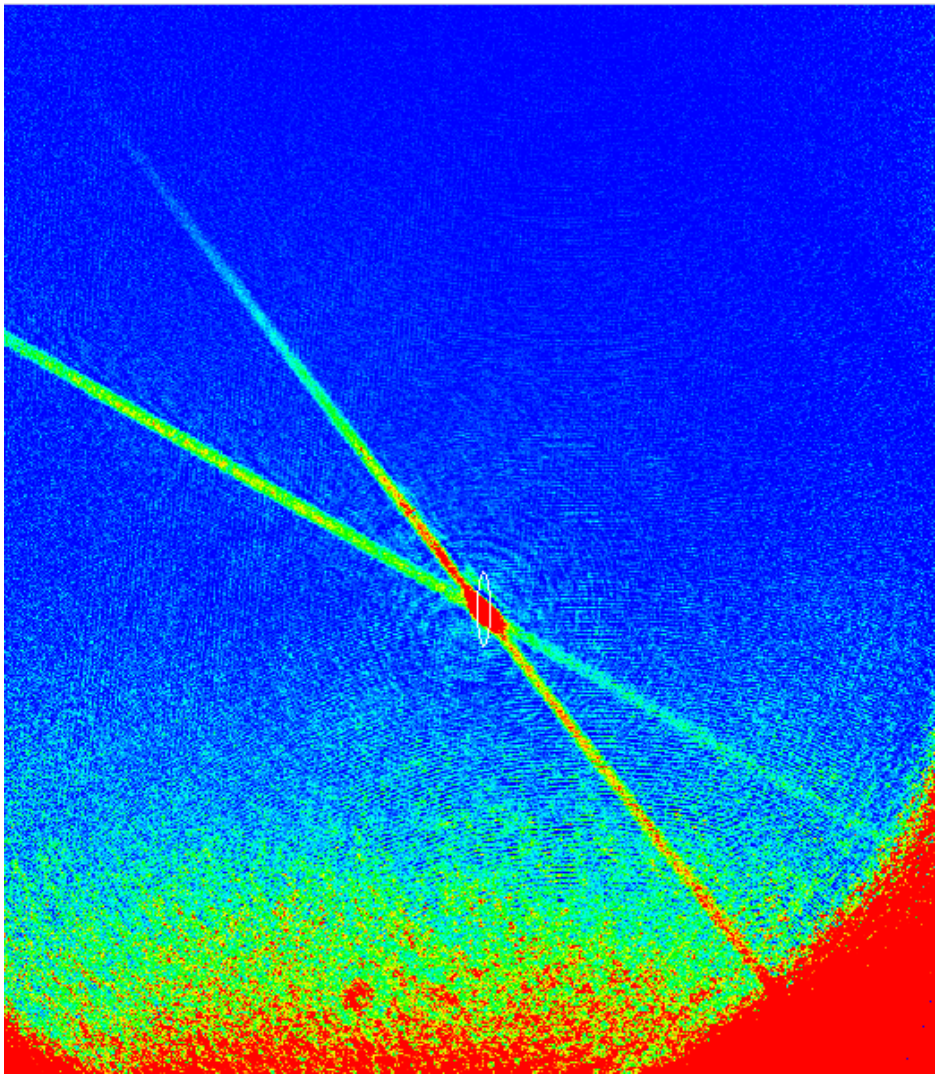

Fig. 7.1 Absorption image of the crossed optical dipole trap with $\sim 1.8 \times 10^6$ atoms in the crossing region. The angle between crossed beams is $\sim 22°$.

After loading, the number of atoms in the trap decays exponentially via several mechanisms. The primary cause of atom loss are collisions with room temperature background gas atoms. This rate of decay is directly proportional to the quality of the vacuum. The lifetime of the trap is defined as the time taken to reach 1/e of the number of initial atoms in the trap. This was

determined by measuring the number of atoms in the crossing region via absorption imaging as a function of storage time while maintaining full power in the beams. The resulting curve is presented in Figure 7.2. From Figure 7.2, we can make two main observations regarding the rate of decay of atoms from the trap. At short storage times <150 ms, we observe a rapid and almost linear decay. This is then followed by a much slower, exponential decay. The initial high rate of decay can be attributed to evaporation of hottest atoms from the trap and has also been observed in [77]. Thermal equilibrium is reached within ∼100 ms and is followed by a slower rate of exponential decay, dominated by losses due to collisions with the background atoms. By measuring the lifetime of the ODT we also gain an idea about the quality of the vacuum within the chamber. Lifetimes of ∼3-20 seconds are typically observed in ODT experiments in vacuum conditions similar to ours ($\sim 1 \times 10^{-10}$ mbar). From 7.2, we estimate the 1/e lifetime to be ∼8 seconds, which is consistent with the expected values, yet lower than the lifetime of ∼22 seconds observed in the "old" lab in similar vacuum conditions.

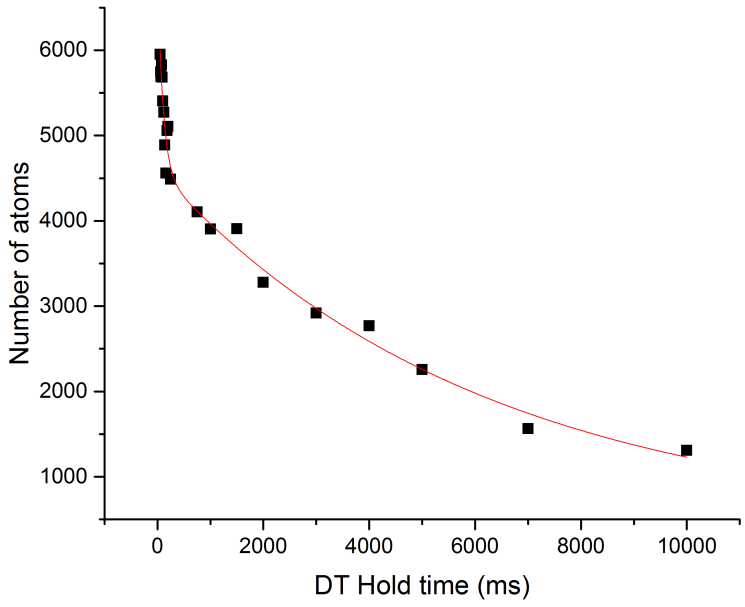

Fig. 7.2 Lifetime of atoms in the Crossed Optical Dipole Trap. The fit of the data is formed by two exponentials. The initial high rate of decay is due to evaporation of the hottest atoms from the trap. The lifetime of atoms after the initial decay is ∼8 seconds.

7.2 Attempt at Evaporative Cooling

The next step was to reduce the temperature of the atoms in the ODT using forced evaporative cooling. In an all-optical set-up, this is performed by ramping down of the power is the trap beams, followed by a period of re-thermalisation. The most optimal way to evaporate is to use an exponential ramp [93]. This is due to the fact that reducing the power in the beams also reduces the trap frequency by $\sqrt{P} \propto \omega$, which in turn reduces the density and the rate of elastic collisions. If the power is ramped down too fast, the atoms have insufficient time to re-thermalise. If the evaporation proceeds too slowly, one body loses become the dominant loss mechanism, limiting the efficiency of evaporation.

In the old lab, a dimple beam was used to aid in confining atoms at the centre of the trapping potential during evaporation. The dimple beam configuration [94] involves overlapping an additional beam, usually derived from the same laser as the ODT beams, with the centre of the crossed ODT. The beam is usually held at a much lower power to the ODT beams, so its contribution is negligible during the loading stage. During evaporation the trapping potential of the dimple becomes significant as the power of the ODT beams is decreased. The dimple beam has a narrower diameter than the ODT beams and so it aids in spatially confining the atoms in it's potential and keeping the density high.

We have started to implement the dimple beam configuration in the new lab when it became apparent that the bad quality of the beam made it very difficult to produce a waist any smaller than 70 μm. In section 4.6 we briefly discuss how the expected size of the beam waist is 47 μm, while the actual size is 70 μm. This corresponds to a beam quality factor of $M^2 \sim 1.45$. By contrast, an ideal Gaussian beam has $M^2 = 1$. This is a significant deviation from a Gaussian beam. Even though the beam appears "clean" and symmetrical when exiting out of the laser, the same M^2 quality factor is measured. A visual deformation can be observed when the beam size is reduced to 3 mm using lenses, as seen in Figure 4.9 in Chapter 4. This suggests that the beam wavefront becomes even more deformed when it is focused down to 70 μm.

Another important parameter to consider when discussing evaporative cooling is the phase-space density,

$$\rho = n_0 \lambda_{dB}^3, \tag{7.1}$$

where n_0 is the atom density and $\lambda_{dB} = \sqrt{2\pi\hbar^2 m k_B T}$ is the thermal de Broglie wavelength.

The phase space density can also be expressed in terms of the number of atoms, N, their temperature, T, and the geometrical mean of the trapping frequencies, $\bar{\omega}$:

$$\rho = N\left(\frac{\hbar\bar{\omega}}{k_B T}\right)^3. \tag{7.2}$$

The phase-space density in a typical optical dipole trap is in the order of $10^{-4} - 10^{-5}$, while Bose-Einstein condensation occurs when $\rho \sim 2.6$.

For starting conditions in our ODT, prior to evaporation, we had 1.8×10^6 atoms, with a temperature of 163 μK, and phase space density of $1.94 \times 10^{-}5$. We ramped the power of the ODT down from 20 W to 300 mW exponentially over 6 seconds. At 300 mW the peak trap depth was 10 μK with radial and axial trapping frequencies of 153 Hz and 27 Hz respectively. By performing an exponential ramp of the power in the ODT beams, we were able to decrease the temperature of the atoms to 1 μK, and a calculated phase-space density of 2.8×10^{-3}. The final atom number was 4×10^4, and we were unable to evaporate any further due to losing too many atoms.

We can quantify the efficiency of evaporative cooling by simply calculating the decrease in temperature per particle lost:

$$\gamma_{eff} = -\frac{ln(\rho_f/\rho_i)}{ln(N_f/N_i)}, \tag{7.3}$$

where ρ_i and ρ_f is the initial and final phase space density, and N_i and N_f is the atom initial and final atom number. For our best evaporation conditions, we achieved an efficiency of 1.3. By comparison, typical evaporation efficiency achieved in the old lab was between 2.1 and 2.5.

In Table 7.1 we present the initial and final conditions of our evaporation stage and compare them to the results from the "old" lab and other similar experiments from literature. We can note that successful BEC production involves initial phase-space densities in the ODT of $\rho_i > 10^{-4}$, and efficiency of evaporation $\gamma_{eff} > 2.1$. It is clear that our starting phase space density is too low for runaway evaporative cooling. This means the elastic collision rate is too low right from the start, resulting in a low efficiency of evaporation of 1.3. We expect

Ref.	N_i	N_f	ρ_i	ρ_f	γ_{eff}
Ref. [95]	1.9×10^6	5×10^5	0.0445	2.6	3.05
Ref. [77]	2×10^6	1.8×10^5	0.0018	1.4	2.76
Ref. [93]	5×10^5	4.9×10^4	2.59×10^{-4}	2.6	3.95
"Old" lab [63]	5×10^6	5×10^4	4.76×10^{-4}	2.6	2.1
This work	1.8×10^6	4×10^4	1.94×10^{-5}	2.79×10^{-3}	1.3

Table 7.1 Comparison of initial and final conditions during evaporative cooling in optical dipole traps from literature, the "old" lab, and present work. γ_{eff} is the efficiency of evaporation calculated using equation 7.3.

to be able to trap at least 5×10^6 atoms in our ODT since its volume is larger than that in the old lab. Therefore, there must be some issue with the loading of our trap, which must be further investigated. One potential problem could be resonant light leaking into the system right after loading. The bad quality of the laser beam results in a deformed trapping potential and will contribute to poor loading of the trap as well as will hinder the condensation of atoms into the centre of the crossing region during evaporation. This could be the reason why we are seeing lower phase-space densities than in other similar experiments, as shown in Table 7.1.

Additionally, while our lifetime was within the expected limits, it was still considerably lower than that reported by R. Moore in the old lab. This prevented us from attempting slower evaporation ramps, which could reduce losses via three-body collisions. This is peculiar since the vacuum conditions in our set up are at least as good. This could mean that the loss of atoms in our ODT is accelerated by some additional process, such as leaking resonant light. Currently, the priority is to fix the issue with the quality of the ODT beam. This would allow us to utilise the dimple trap beam, which is crucial for maintaining the rate of elastic collisions. This could also improve the number of atoms that we are able to load into the ODT from the MOT, and therefore increase the phase space density.

Chapter 8

Discussion and Conclusion

8.1 Current Status of the Experiment

During the course of this project we have developed and built from scratch a full cold-atom apparatus capable of laser cooling and trapping Rubidium atoms in a crossed optical dipole trap. This included the design, construction and testing of three different UHV chambers. The final chamber design, the "Globe" chamber proved most successful due to it's robustness and good optical access. A vacuum of $< 5 \times 10^{-10}$ mbar was achieved after bakeout. The design also allowed for easier exchanging of the fused silica prism in the future, for planned experiments with evanescent wave surface traps and atom chips, by attaching the prism inside the chamber mechanically instead of using glue.

We have designed, realised and characterised an LVIS chamber capable of achieving a high flux of atoms (7.5×10^9atoms/s) travelling at slow velocities of 7.8 ± 0.5m/s. The main advantage of our LVIS chamber design is that it can produce this high flux of atoms without the need to heat the Rb reservoir. This provides further advantages, such as better vacuum and reduced power consumption. Due to this, our design has already attracted interest from other cold atom groups. We suspect that the reason we were able to achieve this high flux of atoms was due to the absence of copper parts from inside the LVIS chamber. It appears that the copper parts absorb some of the Rubidium atoms and lower the vapour pressure within the LVIS chamber. From our tests with several LVIS designs we were able to observe the high flux of trappable atoms when we substituted the internal copper mirror clamps for ones made from stainless steel.

Using our LVIS, we were able to load a large MOT consisting of 9×10^9 atoms in as little as 1.7 seconds. The initial temperature of atoms in the MOT was measured to be $\sim$300μK. The temperature was further reduced below the Doppler limit through the use of "dark" molasses to $\sim$30μK.

Having achieved good starting conditions in the MOT, the optical dipole trap was set up using a 50W 1064 nm laser. We were able to load 1×10^6 atoms into the crossed ODT from the dark molasses. We also observed a sufficiently long 1/e lifetime of the ODT ($\sim$8 seconds) for evaporation to BEC. In order to produce a BEC through forced evaporation, we would need to start with at least 3×10^6 atoms in the ODT. Since we have a large MOT, it should be relatively straight forward to load a lot more atoms into the ODT. More work is required to fine-tune the loading sequence, particularly the tuning of the dark molasses process to maximise the transfer into the ODT.

The intensity stabilisation was also set-up for the crossed ODT. Stabilising the intensity is important for the forced evaporation stage as intensity fluctuations could be a source of heating during the exponential ramp of intensity. Once we are able to load a sufficient amount of atoms into the ODT we will be able to cool atoms to BEC.

8.2 Next Steps

This chamber was designed to be the testing ground for surface mounted all-optical atom chips. To fulfil its purpose, we will first need to demonstrate that we can transport atoms to, and trap them close to, the surface of the fused silica prism. The first challenge will be to demonstrate the all-optical transfer of BEC atoms from the optical dipole trap to the surface Bi-Chromatic EW Trap. This EW trap will be formed using free-space beams, totally internally reflected from the flat polished surface of the prism. The successful demonstration of this transfer and surface trapping will be an important stepping stone towards realising integrated EW traps and waveguides on a substrate.

8.2.1 Larger BEC via Painted Potential

A dynamically-shaped dipole trap will be implemented in order to increase the number of atoms forming the BEC.

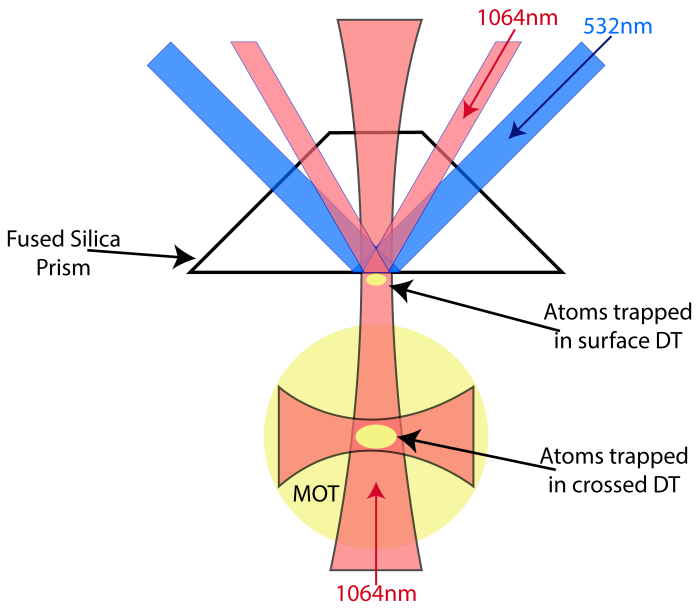

Fig. 8.1 Scheme for all-optical transfer of atoms from ODT to surface EW trap.

This will be achieved by producing a painted dipole potential to increase the trap volume. This has the primary benefit of trapping more atoms before evaporative cooling to BEC. The secondary benefit is the ability to decrease the trap volume dynamically as evaporative cooling takes place, thereby realising a more efficient thermalisation process necessary for the production of a BEC.

The dynamical shaping of the trap will be achieved by modulating the AOM driving frequency. With appropriate positioning of the lens at the output of the AOM, a change in modulation frequency is converted to a lateral beam shift. This scheme is illustrated in Figure 8.2(Top). Varying the modulation frequency by ± 5 MHz provides a shift of ± 4 mm for a focal length of 500 mm, see Figure 8.2(Bottom)..

8.2.2 Transfer Trap Implementation

In order to transport the atoms from the dipole trap towards the surface of the prism for studying the optical evanescent wave trap, an air bearing translation stage will be used to move the focusing lens of the dipole trap. This will have the effect of shifting the dipole trap upwards, towards the prism and taking the trapped atoms with it.

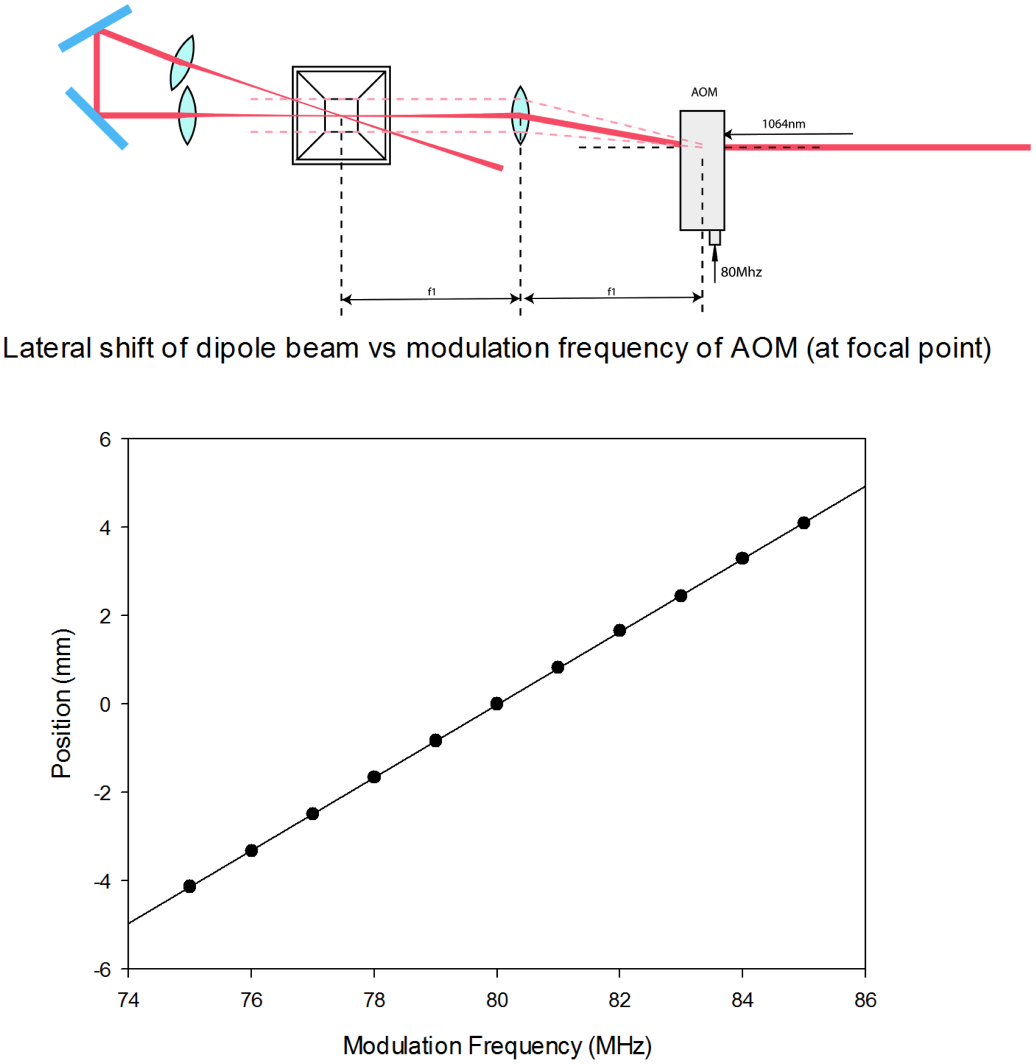

Fig. 8.2 Optical Dipole Painted Potential Scheme. Top: Optical configuration for realisation of a painted optical dipole potential in the crossed beam configuration. Due to the optical configuration, this produces a parallel shift of the beam and the focal point, which is located inside the science cell. Bottom: Experimental measurement of the lateral shift of the dipole beam focus as a function of the modulating frequency of the AOM.

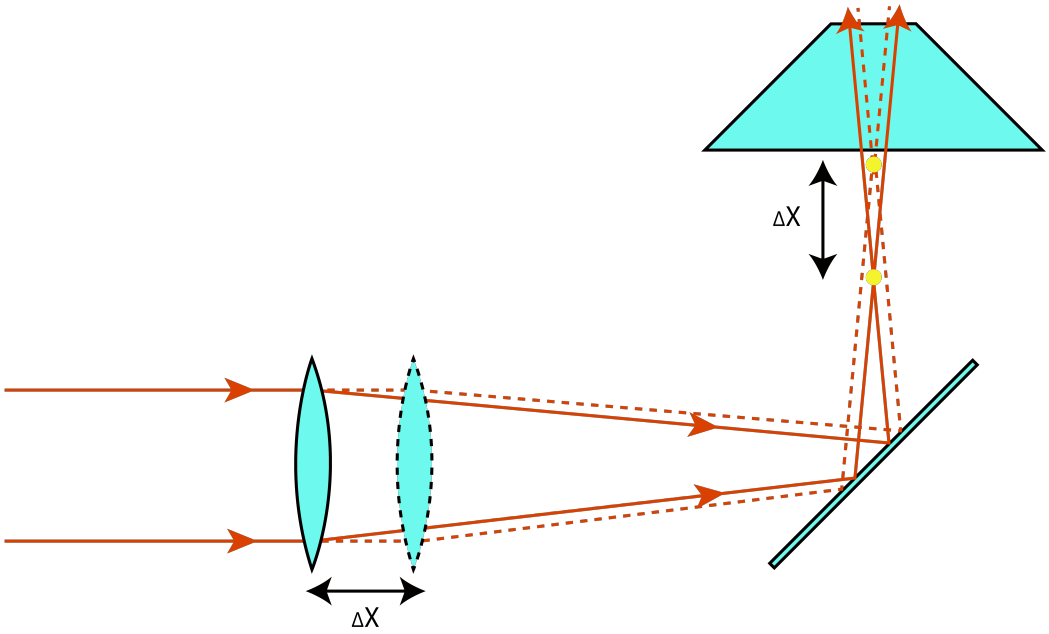

Fig. 8.3 Optical Transfer Trap. The focus of the Dipole Trap beam is shifted upwards by moving the focusing lens closer to the prism. Since the region of maximum trap depth is at the focus the atoms will move with it.

The optical transfer of the atoms needs to be performed adiabatically. For this, a programmable air-bearing linear translation stage was chosen, the A-121 PIglide AT1 manufactured by Physik Instrumente. The air-bearing minimises mechanical vibration and will provide smooth acceleration for adiabatic transport of atoms.

8.3 Conclusion

The experiment discussed in this work needed to be set-up entirely from scratch, and so a large part of this work details the design and assembly of various UHV chambers to perform cold atom experiments. Additionally, a fused silica prism was incorporated in to the design of the chambers to allow for future experiments with evanescent wave traps, and surface mounted atom chips. In this work, we have described the process of designing and assembling different UHV chambers for cold atom experiments. Valuable experience was gained in designing compact chambers with glass walls. After testing several of the compact designs, we decided to instead design and assemble a large volume, steel chamber. The

designed chamber proved successful in attaining good vacuum conditions while being more robust and avoiding the use of UHV glue and indium seals.

During the course of testing of various chambers, we had the opportunity to observe flaws in the typical design of the LVIS. Specifically, the use of copper and glass parts with large surface areas can significantly hinder the performance of the LVIS by preventing full saturation of the LVIS with Rb vapour. We re-designed the LVIS chamber with this in mind. We eliminated the copper parts and reduced the size of glass viewports to the minimum size. We have also re-designed the way the internal mirror is clamped, resulting in an even smaller surface area inside the chamber. Additionally, efforts were made to reduce the internal volume of the LVIS, to be able to achieve better vacuum and full saturation with Rb vapour faster. These modifications resulted in drastic improvements to the performance of the LVIS. We were able to achieve high fluxes of trappable atoms and slow velocities while operating at low total beam powers of 30mW. The most important advantage of our LVIS, compared to others described in the literature, is the fact that it does not require heating of the Rb reservoir to maintain high vapour pressure within the LVIS chamber. This is important for producing better UHV in the main scientific chamber. This and the comparably low power needs of our LVIS makes it ideal for use in compact cold atom sensors and in experiments in space.

Lastly, we were successful in setting up a working crossed Optical Dipole Trap (ODT). We implemented a loading sequence for transferral of atoms from the MOT to the ODT via a dark molasses stage. While we were able to load $\sim 10^6$ atoms, we observed sufficiently long lifetimes of atoms in the trap for future work involving evaporation to BEC.

PART II

FREE-SPACE ATOM INTERFEROMETRY

Chapter 9

Free-Space Atom Interferometry

Publications resulting from material presented in this section:

• V. Guarrera, R. Moore, A. Bunting, T. Vanderbruggen, and Y. B. Ovchinnikov. distributed quasi-bragg beam splitter in crossed atomic waveguides. Scientific Reports, 7(1):4749, July 2017. [60]

9.1 Introduction

This section discusses some of the work performed in the free-space atom interferometry laboratory. We refer to this lab as the “old lab” in this thesis. The motivation for the undergoing work in the "old lab" is the study of continuous waveguide atom interferometers for ultra-cold atoms. This chapter focuses on recent results concerning the behaviour of atoms in a distributed quasi-Bragg splitter formed using guided optical waveguides. These results can also be found in [60], and in the PhD Thesis of Richard Moore [63]. This chapter aims to provide further explanations of atom behaviour as they pass through the splitter, as well as discuss some of the improvements that we have started to implement to the way we control the atom velocity and reflection. These improvements will be vital to the eventual demonstration of a working interferometer using the quasi-Bragg splitter.

My contribution to the work presented in this part of the thesis was as follows. During the first year after starting my PhD at NPL, I was heavily involved in setting up and tuning the laser and optical systems needed for the production of an all-optical BEC, alongside R.

Moore and with guidance from Y.B. Ovchinnikov. This contributed to the observation of the first BEC at NPL, the proof of which obtained by V. Guarerra and R. Moore. At the same time, I have started working full time in the “new” lab, the progress of which was detailed in Part I of this thesis. R. Moore and V. Guarerra continued work in the old lab and obtained all of the experimental data for the distributed Bragg splitter, which we will be referring to in this chapter. After V. Guarerra and R. Moore departures, I continued working part-time in the old lab. My contribution there was predominantly work on improving the experimental apparatus, as well as work with Y.B. Ovchinnikov on providing further explanations to the observation of "fragmentation" of atoms after recombination by the quasi-Bragg splitter, which was previously unexplained.

9.2 Continuous Bragg Splitter

A novel approach to coherently split a matterwave in optical waveguides was explored in the old lab [60]. The coherent splitter was realised by the overlapping of two tightly focused, far red-detuned, laser beams producing an optical lattice at the crossing region. The optical dipole beams function as optical waveguides along which a matter-wave can propagate. Through the principle of Bragg reflection, atoms propagating through the lattice are selectively transmitted and reflected from one waveguide into the other, in a continuous manner. Hence, we refer to this splitter as the continuous waveguide Bragg splitter.

The trapping potential in the transverse plane of the crossing region of two far detuned optical waveguides can be defined in 1D as:

$$U_{well}(r) = -U_0 exp(\frac{-2r^2}{w^2}), \tag{9.1}$$

where U_0 is the potential depth which is proportional to the intensity of the laser beams and w is the beam waist. An optical lattice is formed in the crossing region of the two beams due to interference. The lattice can be modelled as:

$$U_{lattice}(r) = -2\varepsilon U_0 exp(\frac{-r^2}{w^2}) cos(2kr), \tag{9.2}$$

where $k = 2\pi/\lambda$ is the wave number of the light and ε is the interference coefficient which represents the relative polarisation of the two beams and takes values $0 \leq \varepsilon \leq 1$.

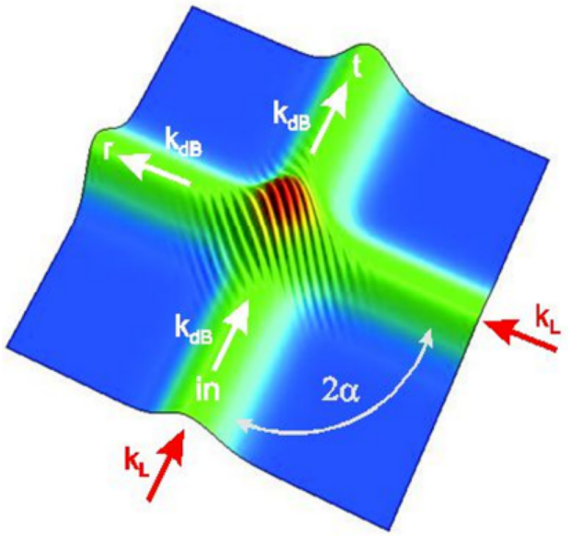

Fig. 9.1 Continuous Waveguide Bragg Splitter. Illustration is by Y. Ovchinnikov. [57]. Atoms are diffracted at the optical lattice in the cross region of the beams, and are split between the two waveguides. k_L and k_{dB} are the wavevectors of the laser beams and the matter-wave respectively. The waveguides into which the atoms are either reflected or transmitted are labeled respectively with an r and t.

The resulting potential experienced by atoms propagating through the crossing region is then:

$$U(r) = -U_0[1 + exp(\frac{-2r^2}{w^2}) + 2\varepsilon exp(\frac{-r^2}{w^2})cos(2k_{eff}x)]. \tag{9.3}$$

k_{eff} is the effective wavevector $k_{eff} = 2sin(\alpha/2)k = 2\pi/d$ where $a\alpha$ is the crossing angle of the beams and d is the lattice spacing. The periodic potentials for different values of ε are illustrated in Figure 9.2.

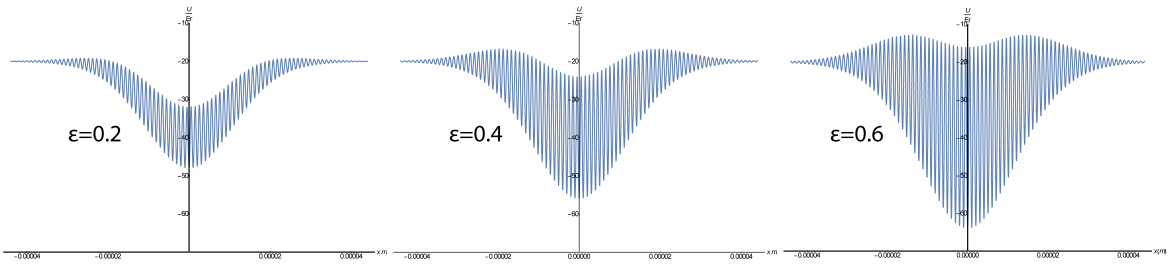

Fig. 9.2 Optical lattice periodic potentials formed by crossing of two waveguides for different interference coefficients.

To understand how an atom can be reflected by an optical lattice we have to consider band theory [96] and the theory of the Mathieu equation [97]. The time dependent Schrödinger

equation for the wavefunction $\psi(x)$ of an atom travelling in an infinite optical lattice is given as:

$$\widehat{H}\psi(x) = \left[-\frac{h^2}{2m}\frac{\delta^2\psi}{\delta x^2} + U(x)\right]\psi(x) = E\psi(x), \tag{9.4}$$

where $E = mv^2/2$ is the energy of the particle. The periodic potential experienced by the atom can be expressed simply as:

$$U(x) = -U_0 sin^2(\pi x/d), \tag{9.5}$$

where d is the lattice spacing. Substituting (9.5) into (9.4), we can rewrite the Schrödinger equation as:

$$\frac{\delta^2\psi}{\delta x^2} + p[a - 2qcos\frac{2\pi x}{d}]\psi = 0, \tag{9.6}$$

which takes the form of the Mathieu equation [98], where a and q are:

$$\begin{cases} a = 4(v/v_R)^2 + 2U_0/E_R, \\ q = U_0/E_R \end{cases} \tag{9.7}$$

Depending on the parameters q and a, the solutions to the Mathieu equation will either remain bounded or at least one of the solutions will grow exponentially as x/d increases. This corresponds to stable and unstable regions in the (q,a) plane. The unstable regions correspond to the situation where the energy of the incident atom lies in a forbidden band and results in total reflection by the lattice. The positions of the band gaps are determined numerically by plotting the equation of the boundaries between the stable and unstable regions. The equation for these boundaries are given by the Mathieu characteristic functions $a_n(q)$ and $b_n(q)$ [99]. Figure 9.5 shows the graphical representation of the bands for a particle with energy E and a lattice of depth U_0.

9.3 Experimental Procedure

In this section, we will present the experimental set-up and procedure of the free-space Bragg splitter experiment conducted in the "old" lab. More detailed descriptions of the methods can be found in the [63] and [60].

A BEC of 7×10^4 ^{87}Rb atoms was prepared at the crossing region of a crossed optical dipole trap with dimple, in an all-optical manner. The crossed ODT was formed using a single 1064 nm beam, intersected with itself as illustrated in 9.3(a). The BEC was then loaded into a linear optical waveguide (WG1), overlapped with the crossed ODT, by rapidly switching off the beam of the ODT. The atoms then propagate along WG1 which has an axial frequency of $2\pi \times 2.4$ Hz and radial frequency of $2\pi \times 190$ Hz. A second waveguide (WG2) is crossed with WG1 at 90°, at a distance δ from the centre of the crossed ODT, where the BEC was produced. The two waveguides were created by linearly polarised beams produced by the same laser as the ODT, with a wavelength of 1064nm and were intersected at their minimum waist of $\sim$20 μm. The trapping potential produced by each waveguide at the intersection region is $U_0 \sim 25E_R$.

WG1 and WG2 interfere at the intersection region, producing an optical lattice the height of which can be controlled by setting the angle between the linear polarisations of the two crossed laser beams, see 9.3(b). After atoms are released from the ODT, they naturally propagate along WG1 towards the minimum of the trapping potential at the crossing region of WG1 and WG2. The maximum velocity of the atoms arriving at the crossing region could be controlled by varying the distance of δ. The maximum velocity that was observed in this way was $4.7v_R$, where $v_R = 4.3$mm/s is the recoil velocity, at $\delta \sim 1$ mm, corresponding the Rayleigh length of the waveguide beam [60]. Higher wavepacket velocities, up to $23v_R$, were produced by the use of a magnetic field gradient produced by a single magnetic coil, aligned along the axial direction of WG1. The magnetic coil for accelerating the atoms into the lattice was also used to reflect the transmitted atoms back towards the lattice for recombination by reversing the current. For the reflection of the atoms reflected into WG2 by the lattice one of the MOT coils was used (not pictured in Figure 9.3(a)).

The behaviour of the atoms as they passed through the lattice were observed by absoprtion imaging. Atoms were allowed sufficient time to pass through the crossing region, the intensity of the waveguides was then reduced to zero followed by imaging of the atoms after a time of flight of 2 ms. Analysis software was then used to calculate the number of atoms in each

of the waveguides. To measure the flux of atoms in the waveguides after recombination(see Figure the analysis software was used to measure the number of atoms in a small region of space after the crossing region.

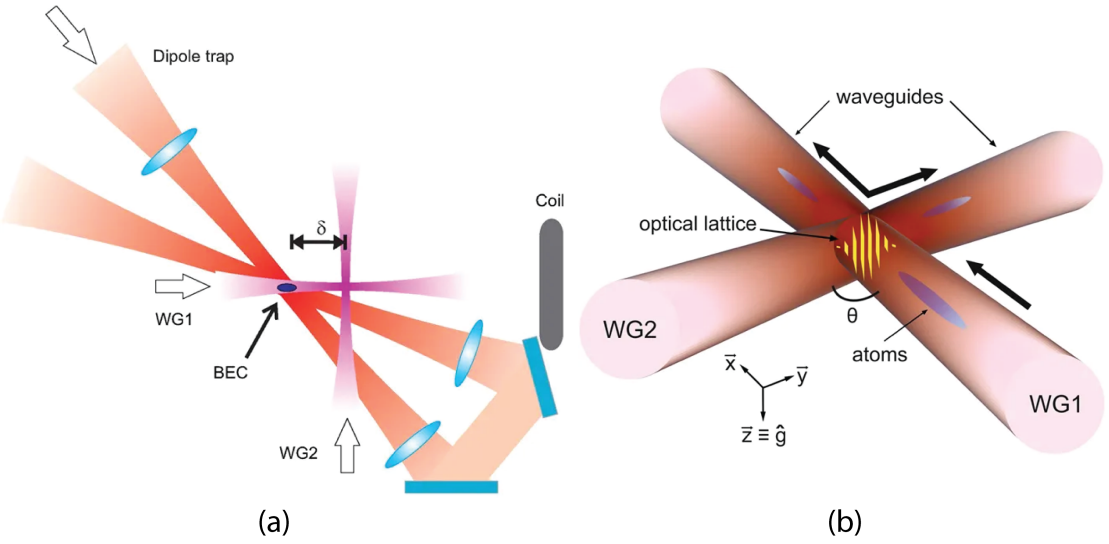

Fig. 9.3 Optical Set-up of the Bragg Splitter. (a) The optical set-up of the Bragg splitter experiment. The view is a bird's eye view, with gravity acting into the page. (b) A focused view of the Bragg splitter. Atoms propagate along WG1 until they reach the optical lattice, where they are either transmitted along WG1 or reflected into WG2. Diagrams from [63].

9.4 Revision of Results

The results of interest to this work are the ones regarding the behaviour of atoms in the splitter, during the initial pass through the lattice - splitting, and the second pass after reflection by magnetic coils - recombination. In particular, "fragmentation" of atoms between the two ports was observed after recombination. In this chapter we aim to explain the origin of the "fragmentation". We will first begin by explaining the behaviour of atoms in both waveguides after the initial splitting.

Figure 9.4(left) shows an absorption image of the atoms after an initial pass through the lattice at a 32 mm/s which produces roughly equal splitting into both waveguides. We observe that the atoms in both waveguides have been excited into higher modes by the lattice, and that the oscillations are visibly different. Figure 9.4(right) illustrates the origin of the oscillations. For the atoms reflected into WG2, they were reflected not only at the centre of the lattice (region B), but also at two other regions (A and C). The transmitted atoms are also excited

into higher modes because of some misalignment of the two waveguides from 90°. Figure 9.5 shows the calculation of the position of the reflection bands as experienced by the atoms travelling through the lattice. The calculation was performed using "MathieuCharacteristicA" and "MathieuCharacteristicB" in Mathematica. The green region shows the case for the set-up used and the blue lines represent the bands.

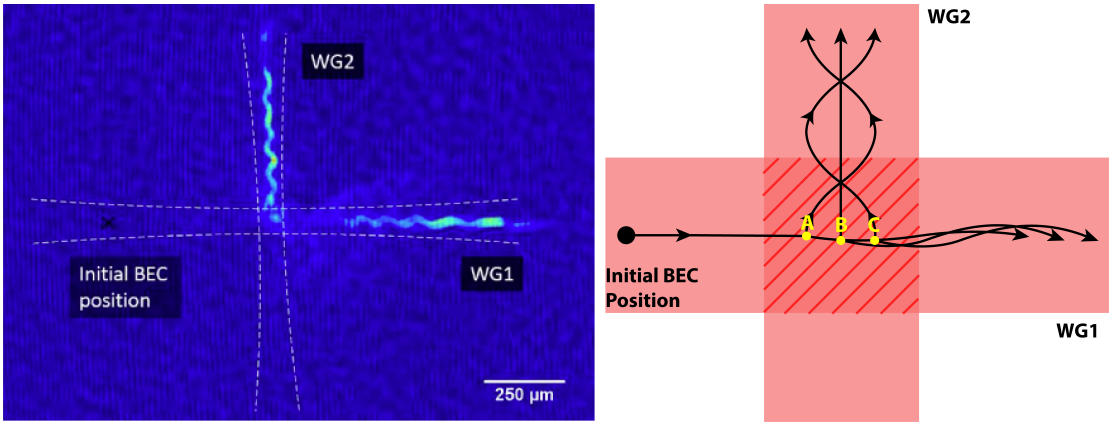

Fig. 9.4 Behaviour of Atoms After Initial Splitting. Left: Taken from [63]. Absorption image of atoms in both waveguides after initial splitting. WG1 contains the atoms that were transmitted, WG2 contains atoms that were reflected. Right: Diagram to illustrate the origin of the oscillations inside both waveguides. Regions A,B and C correspond to points of reflection of atoms into WG2. Region B corresponds to reflection into the ground mode of WG2, while A and C correspond to excitation to the higher transverse mode of WG2. The transmitted atoms in WG1 are also excited into higher modes at these regions due to some misalignment of the beams from 90°.

We will now discuss the behaviour of the atoms after the second pass through the splitter. In [63], after the atoms are reflected back through the lattice, the atomic wavepackets appeared to be "fragmented". This fragmentation was observed in the case of just the single wavepacket returning in WG1, as well as in the case when the transmitted and reflected wavepackets were recominded together. These results were obtained by R.Moore [63] and are presented in Figure 9.6. Figure 9.6 (a) shows the flux of atoms in WG1 after the second pass through the lattice of just the initally transmitted atoms in WG1. Figure 9.6 (b) shows the flux of atoms in WG1 after the second pass through the lattice for the combination of initially reflected and initially transmitted atoms.

We propose the following explanations for this behaviour based on quantum revivals[100],[101]. We begin by describing the behaviour of atoms that were transmitted through the lattice. For this we will refer to illustrations in Figure 9.7. As mentioned previously, due to some misalignment of the waveguides from 90°, the transmitted atoms acquire some excited mode

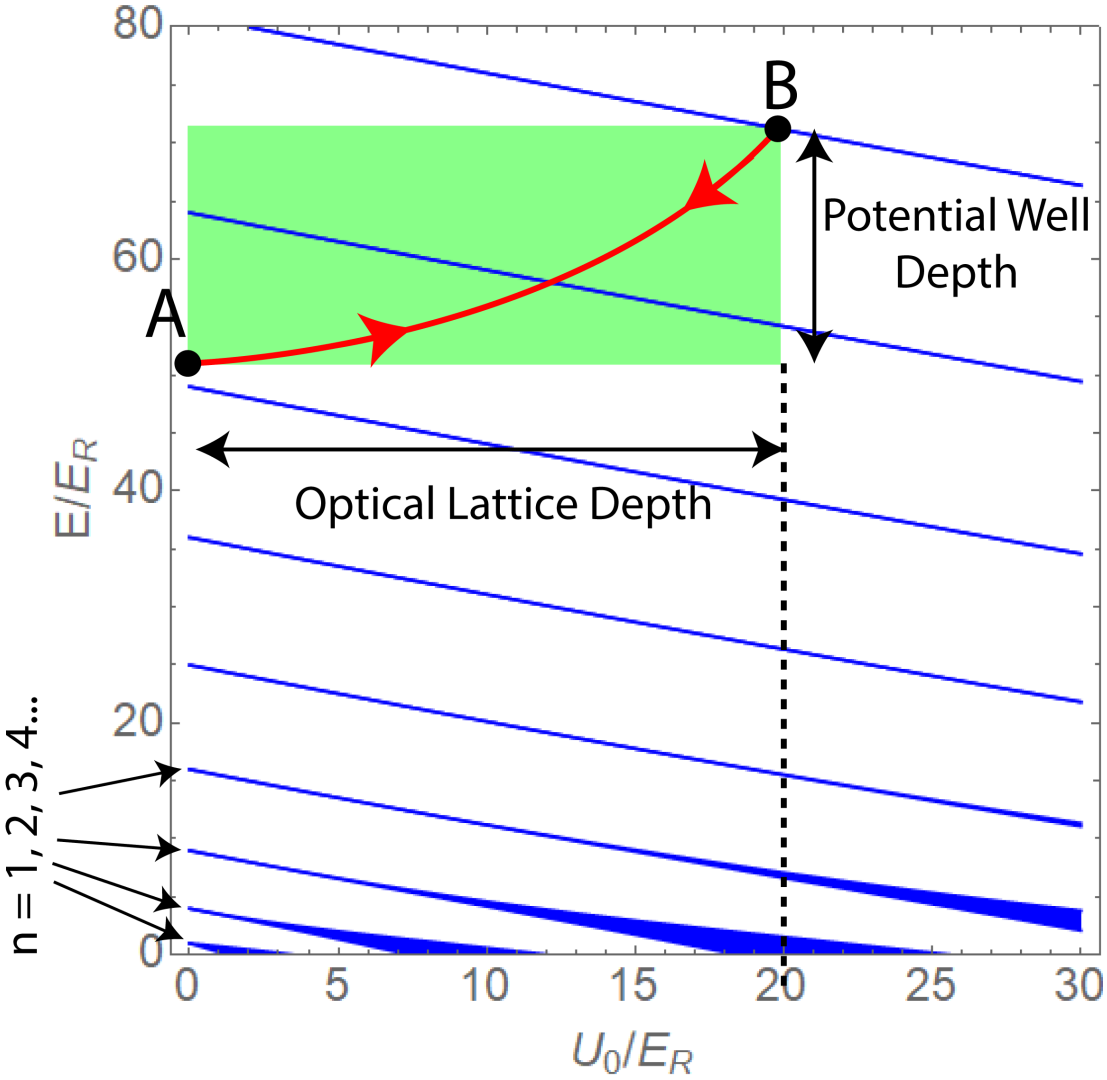

Fig. 9.5 Band gaps in a semi-infinite lattice calculated using the Mathieu equation. At an infinitely small lattice the bands are spaced in accordance with the Bragg condition $E_n = n^2 E_r$. The green region represents the optimal case possible using the current free-space set-up, where $U_0 = 20E_r$ and the beam waist is $w = 20\mu m$. The red line represents the energy of the atoms as they travel through the crossing region. Point A represents the initial energy of the atoms when they enter (and exit) the potential well at the crossing region. Point B corresponds to the energy of the atoms at the centre of the crossing region. The blue filled lines represent bands of reflectance with their thickness being proportional to the probability. In this case the atoms experience three reflection regions: one on the way towards the centre of the potential well, one at the centre and one on the way out.

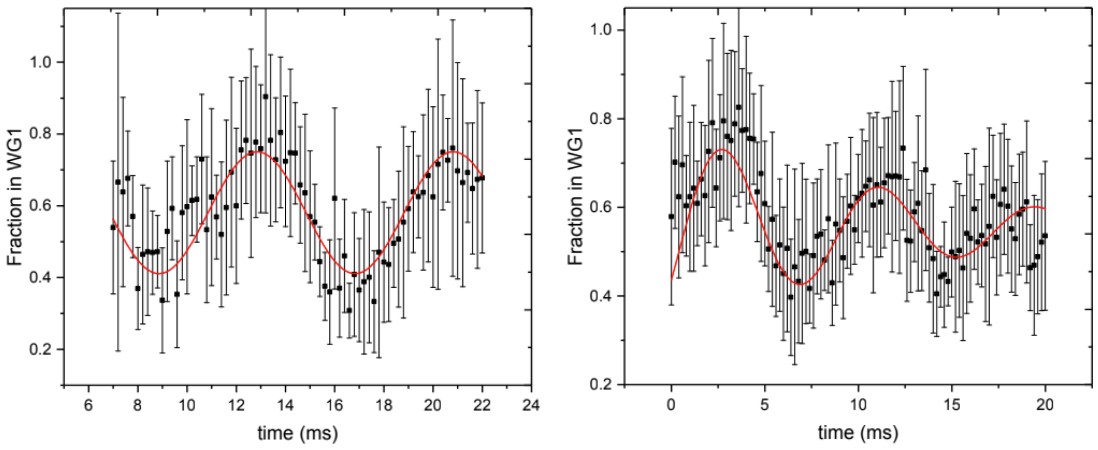

Fig. 9.6 Flux of atoms in WG1 after the second pass through the lattice, after reflection by magnetic coil. (a) Only atoms from WG1 (single magnetic coil) (b) Atoms from WG1 and WG2 (both magnetic coils). Fragmentation is observed in both cases.

which results in an observable oscillation with a period of revival, L_r. The atoms are then reflected back towards the crossing region, at some distance L from the lattice. If the mirror is placed at a distance $2L = NL_r$, the returning atoms will remain precisely in phase for $N = 2,4,6...$ or precisely in anti-phase for $N = 1,3,5...$, and will be split evenly by the lattice as illustrated in Figure 9.7(a). However, in our practical case, the mirror is realised by a gradual repulsive potential produced by a magnetic coil. This means that atoms are reflected not only at $2L = NL_r$, but also at $2L = (N+1/2)L_r$, where $N = 1,2,3....$ The undefined L produces the observed "fragmentation" in both ports, which are in anti-phase with each other.This is illustrated in Figure 9.7(b).

The atoms that were initially reflected into WG2, were reflected at the three different sites. The three partial waves propagate along WG2 with different phases ϕ_a, ϕ_b, ϕ_c. After reflection, assuming interger number of revivals, they arrive back to the lattice with phases $\phi_a + D$, $\phi_b + D$, $\phi_c + D$, where D is the constant phase shift acquired by all partial waves. Since their relative phases are the same as during the first reflection they will now constructively interfere back into the ground state of WG1.

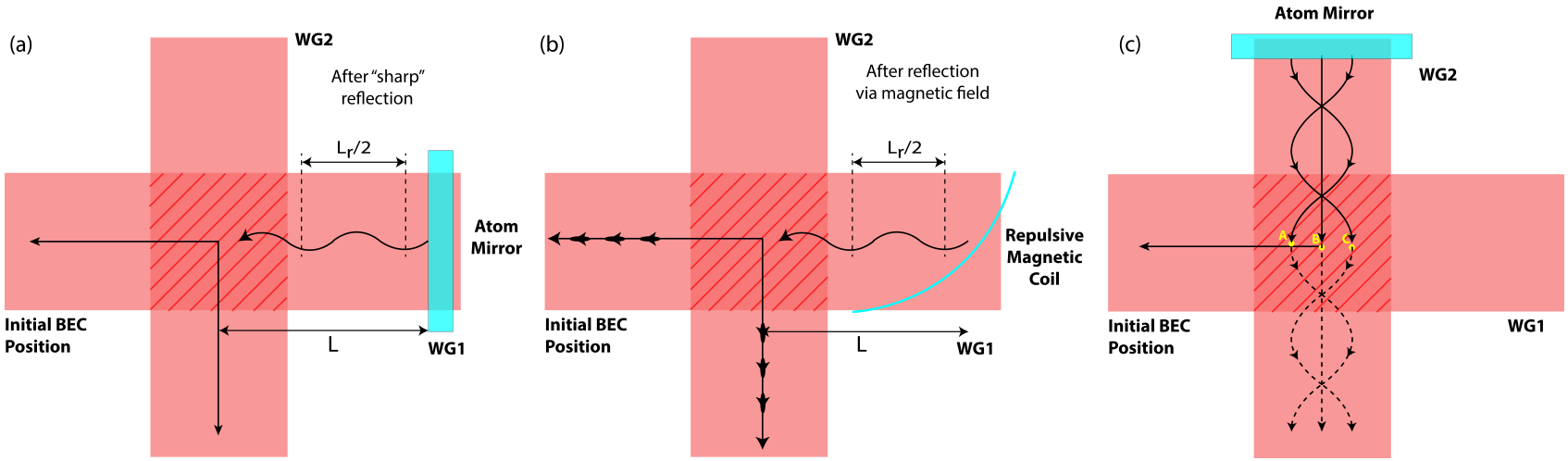

Fig. 9.7 Behaviour of atoms after recombination. (a) Return of the transmitted atoms into the lattice after sharp reflection. The atoms are split 50:50 between the two arms when the mirror is placed at $2L = NL_r$. (b) Return of the transmitted atoms into the lattice after reflection by magnetic coil, resulting in the "fragmentation" observed in Figure 9.6. (c) Return of the reflected atoms. The three partial waves constructively interfere back into the ground mode of WG1.

9.5 Improvements

The atoms were accelerated into the splitter and reflected using applied magnetic fields. The main negative consequence of controlling the velocity of the atoms in this way is that it produces large velocity spreads since the applied potential is gradual. This is the primary cause of the "fragmentation" of the transmitted atoms between the two waveguides after they have been recombined, as discussed in the previous section.

To rectify this, we have begun the implementation of the following two improvements: The acceleration of the atoms into the coils will be performed using a moving standing wave. This will provide a constant acceleration precisely along the axis of the waveguide. The reflection of the atoms will be performed using two blue-detuned "plug" beams. This will provide a sharp repulsive potential, the position of which could be precisely controlled and measured. This was not possible when using magnetic coils.

To realise the moving standing wave, we have overlapped another 1064 nm beam with WG1 beam. This was not trivial, as for the standing wave beam to be superimposed with the waveguide it would have to be coupled from the opposite side of the chamber. Figure 9.8 illustrates our solution. We have installed a dichroic mirror between the LVIS push beam and the LVIS chamber viewport. The dichroic mirror would transmit the 780 nm LVIS beam while reflecting the 1064 nm beam. A second mirror was used to couple the 1064 nm standing wave beam into the LVIS. Both mirrors were mounted on kinematic mounts, to allow for careful tuning of the position and angle of the beam. The beam was then aligned to travel through the 2 mm exit hole of the LVIS and then overlapped with the WG1 beam. The result is a scheme that is similar to the one describe in [102]. When the standing wave beam frequency is detuned by Δf with respect to the WG1, the standing wave pattern will move with velocity

$$v = \Delta f \frac{\lambda}{2}. \tag{9.8}$$

In [63] atoms were accelerated to a velocity of 32 mm/s over 5 ms using a magnetic coil, corresponding to an acceleration of $\sim$0.65g. Using the moving standing wave method we could achieve the same velocity and acceleration by using a linear ramp of frequency detuning from 0 to 60KHz over 5 ms. This method provides significant advantages over accelerating using the magnetic coil:

- Atoms are accelerated precisely along the axis of the waveguide
- The acceleration can be sharply stopped (as opposed to the slow decay of the magnetic field)
- Velocity spread will be reduced as all atoms will experience the same acceleration regardless of their position along the beam. (Velocity spread was $\pm 20\%$ when using the magnetic coil)

We have not been able to experimentaly demonstrate this yet due to unrelated issues with BEC production.

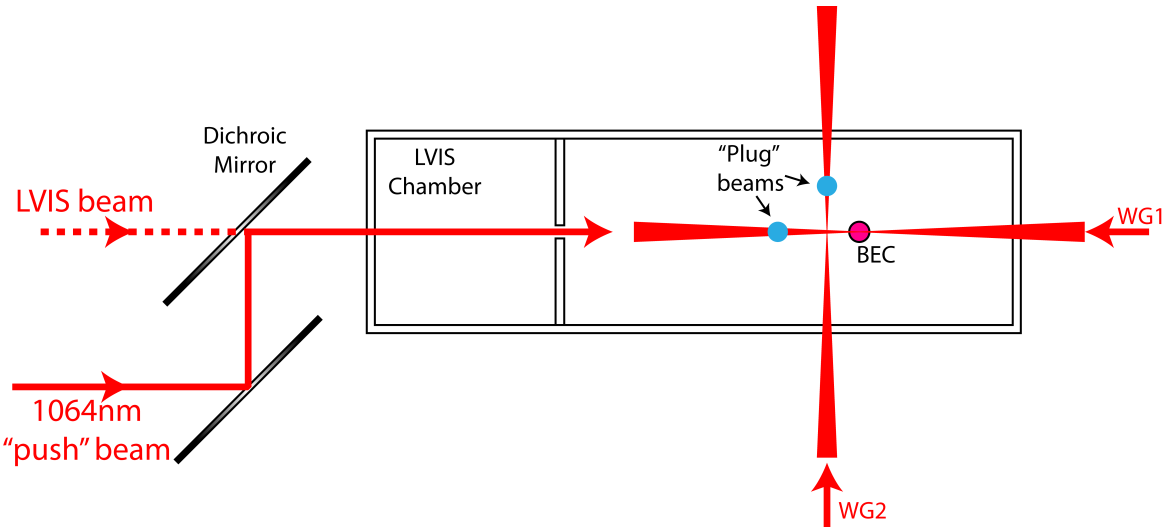

Fig. 9.8 Optical configuration for the realisation of the moving standing wave and sharp reflection (view from above). Two blue-detuned "plug" beams aligned to cross with WG1 and WG2 to provide sharp reflection of atoms after the splitter. Two additional mirrors (one of thich is dichroic) are used to overlap another1064 nm beam with WG1 in order to produce the moving standing wave.

Another key improvement that we are in the process of realising is reflecting the atoms in WG1 and WG2 using two blue-detuned "plug" beams, as illustrated in Figure 9.8. These beams will be aligned in the vertical plane and will interesect with both waveguides perpendicularly. This will produce a sharp repulsive potential. Performing the reflection in this way will allow us to precisely control the propagation distance which should eliminate the "fragmentation" of the transmitted atoms in WG1 after recombination. The beams will be formed using a Sacher Lasertechnik TEC150 770nm laser. The beam position will be controlled using mirrors mounted on Polaris-K1PZ2 piezo mounts. Implementing these atom mirrors together with the moving standing wave acceleration method will allow us to use BEC atoms in

magnetically non-sensitive states which will also reduce the source of different phase noise between the two arms.

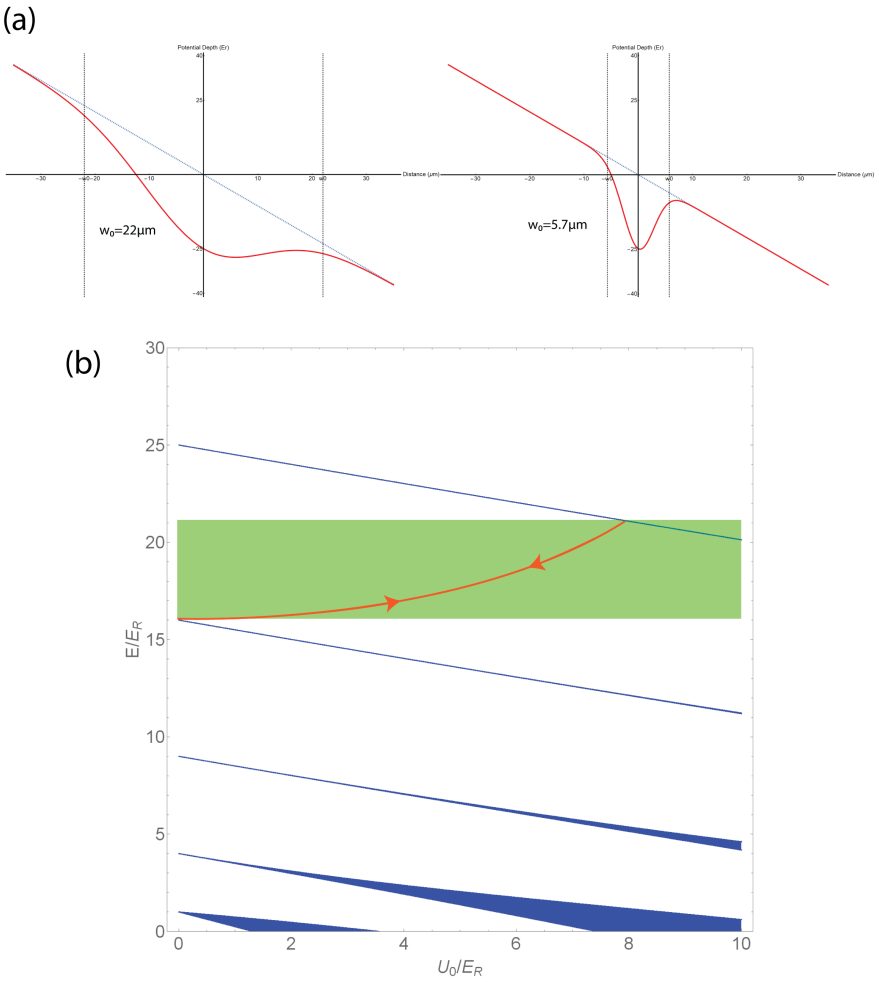

Fig. 9.9 (a) Comparison of the effect of gravity sag for two waveguides with waist of $22\mu m$ and $5.7\mu m$, with equal optical dipole potentials of $25E_r$. The effect of the gravity sag is drastically reduced when using narrower beams. (b) Reflective band encountered by atoms travelling in narrow beams ($5.7\mu m$) at slower velocities . At slower velocities there's also an added advantage of higher probability of reflectance, as depicted by the width of the bands.

Finally, it would also be beneficial to reduce the number of reflective sites in the splitter to one. Currently, atoms reflected into WG2 experience three reflective bands resulting in three partial waves. Ideally the atoms will pass through a single reflective band gap at the centre of the lattice. Looking at Figure 9.5 we can acheive this by reducing the potential depth. However, in practice we are already at the limit of holding atoms in the waveguide against gravity at a trapping potential of 25 E_r. We can reduce the effect of the gravity sag by using smaller beam waists. Figure 9.9(a) illustrates the effect of gravity sag of two beams with

equal trapping depth but different waists. Figure 9.9(b) proposes a way to achieve atoms experiencing only a single reflective band at the centre of the lattice by utilising $5.7\mu m$ beams with shallower potentials.

9.6 Conclusion

We have revised the observed behaviour of atoms in the Bragg splitter. The "fragmentation" of the atoms observed in [63] has been explained in the context of quantum revivals. We have discussed current improvements that are currently underway, such as uniform acceleration of atoms via moving standing wave and sharp reflection using blue-detuned beams. These improvements are crucial, as they will allow for precise control of the phase of the atoms and therefore confirmation of coherence. The advantages of using narrower beams for the waveguides are also mentioned, however this is yet to be realised experimentally.

References

[1] William D. Phillips. Nobel lecture: Laser cooling and trapping of neutral atoms. *Rev. Mod. Phys.*, 70:721–741, Jul 1998.

[2] T.W. Hänsch and A.L. Schawlow. Cooling of gases by laser radiation. *Optics Communications*, 13(1):68 – 69, 1975.

[3] D. J. Wineland and Wayne M. Itano. Laser cooling of atoms. *Phys. Rev. A*, 20:1521–1540, Oct 1979.

[4] A. Clairon, C. Salomon, S. Guellati, and W. D. Phillips. A laser cooled cesium atomic fountain: towards a high performance clock. In *Journées 1991: Systèmes de référence spatio-temporels*, page 37, January 1991.

[5] Michel Abgrall, Baptiste Chupin, Luigi [De Sarlo], Jocelyne Guéna, Philippe Laurent, Yann [Le Coq], Rodolphe [Le Targat], Jérôme Lodewyck, Michel Lours, Peter Rosenbusch, Giovanni Daniele Rovera, and Sébastien Bize. Atomic fountains and optical clocks at syrte: Status and perspectives. *Comptes Rendus Physique*, 16(5):461 – 470, 2015. The measurement of time / La mesure du temps.

[6] J. B. Fixler, G. T. Foster, J. M. McGuirk, and M. A. Kasevich. Atom interferometer measurement of the newtonian constant of gravity. *Science*, 315(5808):74–77, 2007.

[7] Rym Bouchendira, Pierre Cladé, Saïda Guellati-Khélifa, Fran çois Nez, and Fran çois Biraben. New determination of the fine structure constant and test of the quantum electrodynamics. *Phys. Rev. Lett.*, 106:080801, Feb 2011.

[8] Andreas Wicht, Joel M. Hensley, Edina Sarajlic, and Steven Chu. A preliminary measurement of the fine structure constant based on atom interferometry. *Physica Scripta*, T102(1):82, 2002.

[9] Daniel McCarron. Laser cooling and trapping molecules. *Journal of Physics B: Atomic, Molecular and Optical Physics*, 51(21):212001, oct 2018.

[10] Amira M. Eltony, Dorian Gangloff, Molu Shi, Alexei Bylinskii, Vladan Vuletić, and Isaac L. Chuang. Technologies for trapped-ion quantum information systems. *Quantum Information Processing*, 15(12):5351–5383, Mar 2016.

[11] C. Monroe and J. Kim. Scaling the ion trap quantum processor. *Science*, 339(6124):1164–1169, 2013.

[12] Alexander D. Cronin, Jorg Schmiedmayer, and David E. Pritchard. Optics and interferometry with atoms and molecules. *Rev. Mod. Phys.*, 81:1051–1129, Jul 2009.

[13] B. Battelier, B. Barrett, L. Fouché, L. Chichet, L. Antoni-Micollier, H. Porte, F. Napolitano, J. Lautier, A. Landragin, and P. Bouyer. Development of compact cold-atom sensors for inertial navigation. *Quantum Optics*, Apr 2016.

[14] A. A. Michelson and E. W. Morley. On the relative motion of the earth and the luminiferous ether. *American Journal of Science, Vol. 34, No. 203, pp. 333- 345.*, 1887.

[15] Zweizig J. and et al. Gw170817: Observation of gravitational waves from a binary neutron star inspiral. *Phys. Rev. Lett.*, 119:161101, Oct 2017.

[16] L. Zehnder. Ein neuer interferenzrefraktor. *Zeitschrift für Instrumentenkunde 11: 275–285*, 1891.

[17] L. Mach. Ueber einen interferenzrefraktor. *Zeitschrift für Instrumentenkunde 12: 89–93*, 1892.

[18] J. Shamir. *Optical Systems and Processes*. 1991. p.168.

[19] R. Y. Chiao, A. Antaramian, K. M. Ganga, H. Jiao, S. R. Wilkinson, and H. Nathel. Observation of a topological phase by means of a nonplanar mach-zehnder interferometer. *Phys. Rev. Lett.*, 60:1214–1217, Mar 1988.

[20] G. Sagnac. On the proof of the reality of the luminiferous aether by the experiment with a rotating interferometer. *On the proof of the reality of the luminiferous aether by the experiment with a rotating interferometer, Comptes Rendus 157: 1410–1413*, 1913.

[21] Ayswarya P R, Pournami S S, and Ravi Nambiar. Article: A survey on ring laser gyroscope technology. *International Journal of Computer Applications*, 116(2):25–27, April 2015. Full text available.

[22] B Culshaw and I P Giles. Fibre optic gyroscopes. *Journal of Physics E: Scientific Instruments*, 16(1):5, 1983.

[23] Brynle Barrett, Rémy Geiger, Indranil Dutta, Matthieu Meunier, Benjamin Canuel, Alexandre Gauguet, Philippe Bouyer, and Arnaud Landragin. The sagnac effect: 20 years of development in matter-wave interferometry. *Comptes Rendus Physique*, 15(10):875–883, Dec 2014.

[24] Stuart S. Szigeti, Behnam Tonekaboni, Wing Yung S. Lau, Samantha N. Hood, and Simon A. Haine. Squeezed-light-enhanced atom interferometry below the standard quantum limit. *Phys. Rev. A*, 90:063630, Dec 2014.

[25] O. Carnal and J. Mlynek. Young's double-slit experiment with atoms: A simple atom interferometer. *Phys. Rev. Lett.*, 66:2689–2692, May 1991.

[26] David W. Keith, Christopher R. Ekstrom, Quentin A. Turchette, and David E. Pritchard. An interferometer for atoms. *Phys. Rev. Lett.*, 66:2693–2696, May 1991.

[27] Mark Kasevich and Steven Chu. Atomic interferometry using stimulated raman transitions. *Phys. Rev. Lett.*, 67:181–184, Jul 1991.

[28] Ernst M. Rasel, Markus K. Oberthaler, Herman Batelaan, Jörg Schmiedmayer, and Anton Zeilinger. Atom wave interferometry with diffraction gratings of light. *Phys. Rev. Lett.*, 75:2633–2637, Oct 1995.

[29] J. M. McGuirk, G. T. Foster, J. B. Fixler, M. J. Snadden, and M. A. Kasevich. Sensitive absolute-gravity gradiometry using atom interferometry. *Phys. Rev. A*, 65:033608, Feb 2002.

[30] A Peters, K Y Chung, and S Chu. High-precision gravity measurements using atom interferometry. *Metrologia*, 38(1):25, 2001.

[31] T. L. Gustavson, P. Bouyer, and M. A. Kasevich. Precision rotation measurements with an atom interferometer gyroscope. *Phys. Rev. Lett.*, 78:2046–2049, Mar 1997.

[32] Alan Lenef, Troy D. Hammond, Edward T. Smith, Michael S. Chapman, Richard A. Rubenstein, and David E. Pritchard. Rotation sensing with an atom interferometer. *Phys. Rev. Lett.*, 78:760–763, Feb 1997.

[33] B. Canuel, F. Leduc, D. Holleville, A. Gauguet, J. Fils, A. Virdis, A. Clairon, N. Dimarcq, Ch. J. Bordé, A. Landragin, and P. Bouyer. Six-axis inertial sensor using cold-atom interferometry. *Phys. Rev. Lett.*, 97:010402, Jul 2006.

[34] P Gillot, O Francis, A Landragin, F Pereira Dos Santos, and S Merlet. Stability comparison of two absolute gravimeters: optical versus atomic interferometers. *Metrologia*, 51(5):L15–L17, Jun 2014.

[35] Pierrick Cheiney, Lauriane Fouché, Simon Templier, Fabien Napolitano, Baptiste Battelier, Philippe Bouyer, and Brynle Barrett. Navigation-compatible hybrid quantum accelerometer using a kalman filter. *Physical Review Applied*, 10(3), Sep 2018.

[36] J. Le Gouët, T.E. Mehlstäubler, J. Kim, S. Merlet, A. Clairon, A. Landragin, and F. Pereira Dos Santos. Limits to the sensitivity of a low noise compact atomic gravimeter. *Applied Physics B*, 92(2):133–144, Jun 2008.

[37] J. Lautier, L. Volodimer, T. Hardin, S. Merlet, M. Lours, F. Pereira Dos Santos, and A. Landragin. Hybridizing matter-wave and classical accelerometers. *Applied Physics Letters*, 105(14):144102, Oct 2014.

[38] S. Bonvalot, N. Le-moigne, S. Merlet, B. Desruelle, and J. Lautier-gaud. The new absolute quantum gravimeter (aqg): first results and perspectives. *EGU General Assembly Conference Abstracts, p.11824,*, 2016.

[39] Wilbert Rooijakkers, Mukund Vengalattore, Gary Zabow, and Mara Prentiss. Tightly confining waveguide for cold atom interferometry. In *Quantum Electronics and Laser Science Conference*, page QTuG6. Optical Society of America, 2001.

[40] W. Hänsel, P. Hommelhoff, T. W. Hänsch, and J. Reichel. Bose–einstein condensation on a microelectronic chip. *Nature*, 413(6855):498, 10 2001.

[41] H. Ott, J. Fortagh, G. Schlotterbeck, A. Grossmann, and C. Zimmermann. Bose-einstein condensation in a surface microtrap. *Phys. Rev. Lett.*, 87:230401, Nov 2001.

[42] H. Ahlers, D. Becker, S. T. Seidel, T. Wendrich, E. M. Rasel, and M. D. Lachmann W. Ertmer. Creating the first bose-einstein condensate in space, 2018.

[43] Ying-Ju Wang, Dana Z. Anderson, Victor M. Bright, Eric A. Cornell, Quentin Diot, Tetsuo Kishimoto, Mara Prentiss, R. A. Saravanan, Stephen R. Segal, and Saijun Wu. Atom michelson interferometer on a chip using a bose-einstein condensate. *Phys. Rev. Lett.*, 94:090405, Mar 2005.

[44] G. D. McDonald, H. Keal, P. A. Altin, J. E. Debs, S. Bennetts, C. C. N. Kuhn, K. S. Hardman, M. T. Johnsson, J. D. Close, and N. P. Robins. Optically guided linear mach-zehnder atom interferometer. *Phys. Rev. A*, 87:013632, Jan 2013.

[45] A. E. Leanhardt, A. P. Chikkatur, D. Kielpinski, Y. Shin, T. L. Gustavson, W. Ketterle, and D. E. Pritchard. Propagation of bose-einstein condensates in a magnetic waveguide. *Phys. Rev. Lett.*, 89:040401, Jul 2002.

[46] C Ryu and M G Boshier. Integrated coherent matter wave circuits. *New Journal of Physics*, 17(9):092002, sep 2015.

[47] J. Estève, T. Schumm, J.-B. Trebbia, I. Bouchoule, A. Aspect, and C. I. Westbrook. Realizing a stable magnetic double-well potential on an atom chip. *The European Physical Journal D*, 35(1):141–146, Jul 2005.

[48] MP Jones, CJ Vale, D Sahagun, BV Hall, and EA Hinds. Spin coupling between cold atoms and the thermal fluctuations of a metal surface. *Physical review letters*, 91(8):080401, August 2003.

[49] Yu. B. Ovchinnikov, I. Manek, and R. Grimm. Surface trap for cs atoms based on evanescent-wave cooling. *Phys. Rev. Lett.*, 79:2225–2228, Sep 1997.

[50] M Hammes, D Rychtarik, V Druzhinina, Ulf Moslener, Inka Manek-Hönninger, and Rudolf Grimm. Optical and evaporative cooling of cesium atoms in the gravito-optical surface trap. *Journal of Modern Optics*, 47, 11 2000.

[51] M. Hammes, D. Rychtarik, H.-C. Nägerl, and R. Grimm. Cold-atom gas at very high densities in an optical surface microtrap. *Phys. Rev. A*, 66:051401, Nov 2002.

[52] Y B Ovchinnikov, S V Shul'ga, and V I Balykin. An atomic trap based on evanescent light waves. *Journal of Physics B: Atomic, Molecular and Optical Physics*, 24(14):3173, 1991.

[53] M. Hammes, D. Rychtarik, B. Engeser, H.-C. Nägerl, and R. Grimm. Evanescent-wave trapping and evaporative cooling of an atomic gas at the crossover to two dimensions. *Phys. Rev. Lett.*, 90:173001, Apr 2003.

[54] A. H. Barnett, S. P. Smith, M. Olshanii, K. S. Johnson, A. W. Adams, and M. Prentiss. Substrate-based atom waveguide using guided two-color evanescent light fields. *Phys. Rev. A*, 61:023608, Jan 2000.

[55] Y. Meng, J. Lee, M. Dagenais, and S. L. Rolston. A nanowaveguide platform for collective atom-light interaction. *Applied Physics Letters*, 107(9):091110, 2015.

[56] Yuri B. Ovchinnikov and Folly Eli Ayi-Yovo. Towards all-optical atom chips based on optical waveguides. 2019.

[57] Yuri Borisovich Ovchinnikov. Uk patent gb2527148: Waveguide diffraction beam splitters for matter waves based on crossed interfering laser beams and matter wave interferometry using such beam splitters, 2017.

[58] Luigi Amico, Gerhard Birkl, Malcolm Boshier, and Leong-Chuan Kwek. Focus on atomtronics-enabled quantum technologies. *New Journal of Physics*, 19(2):020201, Feb 2017.

[59] Rainer Dumke, Zehuang Lu, John Close, Nick Robins, Antoine Weis, Manas Mukherjee, Gerhard Birkl, Christoph Hufnagel, Luigi Amico, Malcolm G Boshier, Kai Dieckmann, Wenhui Li, and Thomas C Killian. Roadmap on quantum optical systems. *Journal of Optics*, 18(9):093001, aug 2016.

[60] V. Guarrera, R. Moore, A. Bunting, T. Vanderbruggen, and Y. B. Ovchinnikov. distributed quasi-bragg beam splitter in crossed atomic waveguides. *Scientific Reports*, 7(1):4749, July 2017.

[61] A. Browaeys, H. Häffner, C. McKenzie, S. L. Rolston, K. Helmerson, and W. D. Phillips. Transport of atoms in a quantum conveyor belt. *Physical Review A*, 72(5), Nov 2005.

[62] V. Singh, R.R. & Priye. Parametric optimization of fiber to waveguide coupler using bragg gratings. *Opt Quant Electron 51, 256*, (2019).

[63] R. Moore. *Towards interferometry with ultra-cold atoms in crossed optical waveguides*. PhD thesis, 2018.

[64] V. Letokhov, V. Minogin, and B. Pavlik. Cooling and capture of atoms and molecules by a resonant light field. *Sov. Phys. JETP 45(4)*, 1977.

[65] Steven Chu, L. Hollberg, J. E. Bjorkholm, Alex Cable, and A. Ashkin. Three-dimensional viscous confinement and cooling of atoms by resonance radiation pressure. *Phys. Rev. Lett.*, 55:48–51, Jul 1985.

[66] A. Ashkin and J. P. Gordon. Stability of radiation-pressure particle traps: an optical earnshaw theorem. *Opt. Lett.*, 8(10):511–513, Oct 1983.

[67] W. Phillips, P. Lett, S. Rolston, C. Tanner, R. Watts, C. Westbrook, C. Salomon, J. Dalibard, A. Clairon, and S. Guellati. Optical molasses: The coldest atoms ever. *Physica Scripta*, 1991(T34):20, 1991.

[68] J. Dalibard and C. Cohen-Tannoudji. Laser cooling below the doppler limit by polarization gradients: simple theoretical models. *J. Opt. Soc. Am. B*, 6(11):2023–2045, Nov 1989.

[69] C. Cohen-Tannoudji and W. Phillips. New mechanisms for laser cooling. *Phys. Today 43, 33-40*, 1990.

[70] Daniel Adam Steck. Rubidium 87 d line data. 01 2003.

[71] E. L. Raab, M. Prentiss, Alex Cable, Steven Chu, and D. E. Pritchard. Trapping of neutral sodium atoms with radiation pressure. *Phys. Rev. Lett.*, 59:2631–2634, Dec 1987.

[72] Rudolf Grimm, Matthias Weidemüller, and Yurii B. Ovchinnikov. Optical dipole traps for neutral atoms. volume 42 of *Advances In Atomic, Molecular, and Optical Physics*, pages 95 – 170. Academic Press, 2000.

[73] L. Allen and J. H. Eberly. *Optical Resonance and Two-Level Atoms*. Dover, 1987.

[74] M. S. Safronova, Bindiya Arora, and Charles W. Clark. Frequency-dependent polarizabilities of alkali-metal atoms from ultraviolet through infrared spectral regions. *Phys. Rev. A*, 73:022505, Feb 2006.

[75] Sanjay Kumar, Shuuichi Hirai, Yuuki Suzuki, Masahide Kachi, Mark Sadgrove, and Ken'ichi Nakagawa. Simple and fast production of bose–einstein condensate in a 1 μm cross-beam dipole trap. *Journal of the Physical Society of Japan*, 81(8):084004, 2012.

[76] M. H Anderson, Jason Ensher, M. R Matthews, C. Wieman, and E. A. Cornell. Observation of bose-einstein condensation in a dilute atomic vapor. 269:198–201, 08 1995.

[77] M. D. Barrett, J. A. Sauer, and M. S. Chapman. All-optical formation of an atomic bose-einstein condensate. *Phys. Rev. Lett.*, 87:010404, Jun 2001.

[78] Z. T. Lu, K. L. Corwin, M. J. Renn, M. H. Anderson, E. A. Cornell, and C. E. Wieman. Low-velocity intense source of atoms from a magneto-optical trap. *Phys. Rev. Lett.*, 77:3331–3334, Oct 1996.

[79] William D. Phillips and Harold Metcalf. Laser deceleration of an atomic beam. *Phys. Rev. Lett.*, 48:596–599, Mar 1982.

[80] J. Schoser, A. Batär, R. Löw, V. Schweikhard, A. Grabowski, Yu. B. Ovchinnikov, and T. Pfau. Intense source of cold rb atoms from a pure two-dimensional magneto-optical trap. *Phys. Rev. A*, 66:023410, Aug 2002.

[81] K. Dieckmann, R. J. C. Spreeuw, M. Weidemüller, and J. T. M. Walraven. Two-dimensional magneto-optical trap as a source of slow atoms. *Phys. Rev. A*, 58:3891–3895, Nov 1998.

[82] Yuri B. Ovchinnikov. Compact magneto-optical sources of slow atoms. *Optics Communications*, 249(4):473 – 481, 2005.

[83] Rebecca Grinham and Dr Andrew Chew. A review of outgassing and methods for its reduction. *Applied Science and Convergence Technology*, 26:95–109, 09 2017.

[84] C. Wieman and T. W. Hänsch. Doppler-free laser polarization spectroscopy. *Phys. Rev. Lett.*, 36:1170–1173, May 1976.

[85] K. B. MacAdam, A. Steinbach, and C. Wieman. A narrow-band tunable diode laser system with grating feedback, and a saturated absorption spectrometer for cs and rb. *American Journal of Physics*, 60(12):1098–1111, 1992.

[86] C. J. Dedman, K. G. H. Baldwin, and M. Colla. Fast switching of magnetic fields in a magneto-optic trap. *Review of Scientific Instruments*, 72(11):4055–4058, 2001.

[87] Tomasz M Brzozowski, Maria Maczynska, Michal Zawada, Jerzy Zachorowski, and Wojciech Gawlik. Time-of-flight measurement of the temperature of cold atoms for short trap-probe beam distances. *Journal of Optics B: Quantum and Semiclassical Optics*, 4(1):62–66, jan 2002.

[88] Wolfgang Ketterle, Kendall B. Davis, Michael A. Joffe, Alex Martin, and David E. Pritchard. High densities of cold atoms in a dark spontaneous-force optical trap. *Phys. Rev. Lett.*, 70:2253–2256, Apr 1993.

[89] David R. Lide (Ed.). *CRC Handbook of CHemistry and Physics*. CRC Press, Boca Raton, 2000.

[90] Paul Siddons, Charles S Adams, Chang Ge, and Ifan G Hughes. Absolute absorption on rubidium d lines: comparison between theory and experiment. *Journal of Physics B: Atomic, Molecular and Optical Physics*, 41(15):155004, jul 2008.

[91] A. N. Nesmeyanov. *Vapor Pressure of the Chemical Elements*. Amsterdam : Elsevier, 1963.

[92] Richard Conroy, Yanhong Xiao, Mukund Vengalattore, W Rooijakkers, and Mara Prentiss. Compact, robust source of cold atoms for efficient loading of a magnetic guide. *Optics Communications*, 226, 09 2003.

[93] Abraham J. Olson, Robert J. Niffenegger, and Yong P. Chen. Optimizing the efficiency of evaporative cooling in optical dipole traps. *Physical Review A*, 87(5), May 2013.

[94] Tino Weber, Jens Herbig, Michael Mark, Hanns-Christoph Nägerl, and Rudolf Grimm. Bose-einstein condensation of cesium. *Science (New York, N.Y.)*, 299:232–5, 02 2003.

[95] Chen-Lung Hung, Xibo Zhang, Nathan Gemelke, and Cheng Chin. Accelerating evaporative cooling of atoms into bose-einstein condensation in optical traps. *Phys. Rev. A*, 78, 07 2008.

[96] F. Damon, G. Condon, P. Cheiney, A. Fortun, B. Georgeot, J. Billy, and D. Guéry-Odelin. Band-gap structures for matter waves. *Physical Review A*, 92(3), Sep 2015.

[97] Luis Santos and Luis Roso. A band-like reflection spectrum of an atomic beam on a periodic laser profile. *Journal of Physics B: Atomic, Molecular and Optical Physics*, 30(22):5169–5184, nov 1997.

[98] Samuel A. Wilkinson, Nicolas Vogt, Dmitry S. Golubev, and Jared H. Cole. Approximate solutions to mathieu's equation. *Physica E: Low-dimensional Systems and Nanostructures*, 100:24–30, Jun 2018.

[99] C. M. Fabre, P. Cheiney, G. L. Gattobigio, F. Vermersch, S. Faure, R. Mathevet, T. Lahaye, and D. Guéry-Odelin. Realization of a distributed bragg reflector for propagating guided matter waves. *Phys. Rev. Lett.*, 107:230401, Nov 2011.

[100] Gadi Afek, Jonathan Coslovsky, Alexander Mil, and Nir Davidson. Revival of raman coherence of trapped atoms. *Phys. Rev. A*, 96:043831, Oct 2017.

[101] R.W. Robinett. Quantum wave packet revivals. *Physics Reports*, 392(1):1 – 119, 2004.

[102] Stefan Schmid, Arne Härter, Albert Frisch, Sascha Hoinka, and Johannes Hecker Denschlag. An apparatus for immersing trapped ions into an ultracold gas of neutral atoms, 2012.

Chapter 10

Appendix

Compact LVIS Chamber Drawings

In this section we provide detailed mechanical drawings of the LVIS chamber designed, built and tested during this project. The performance of the LVIS using this chamber is studied in detail and presented in Chapter 6 alongside comparisons from literature.

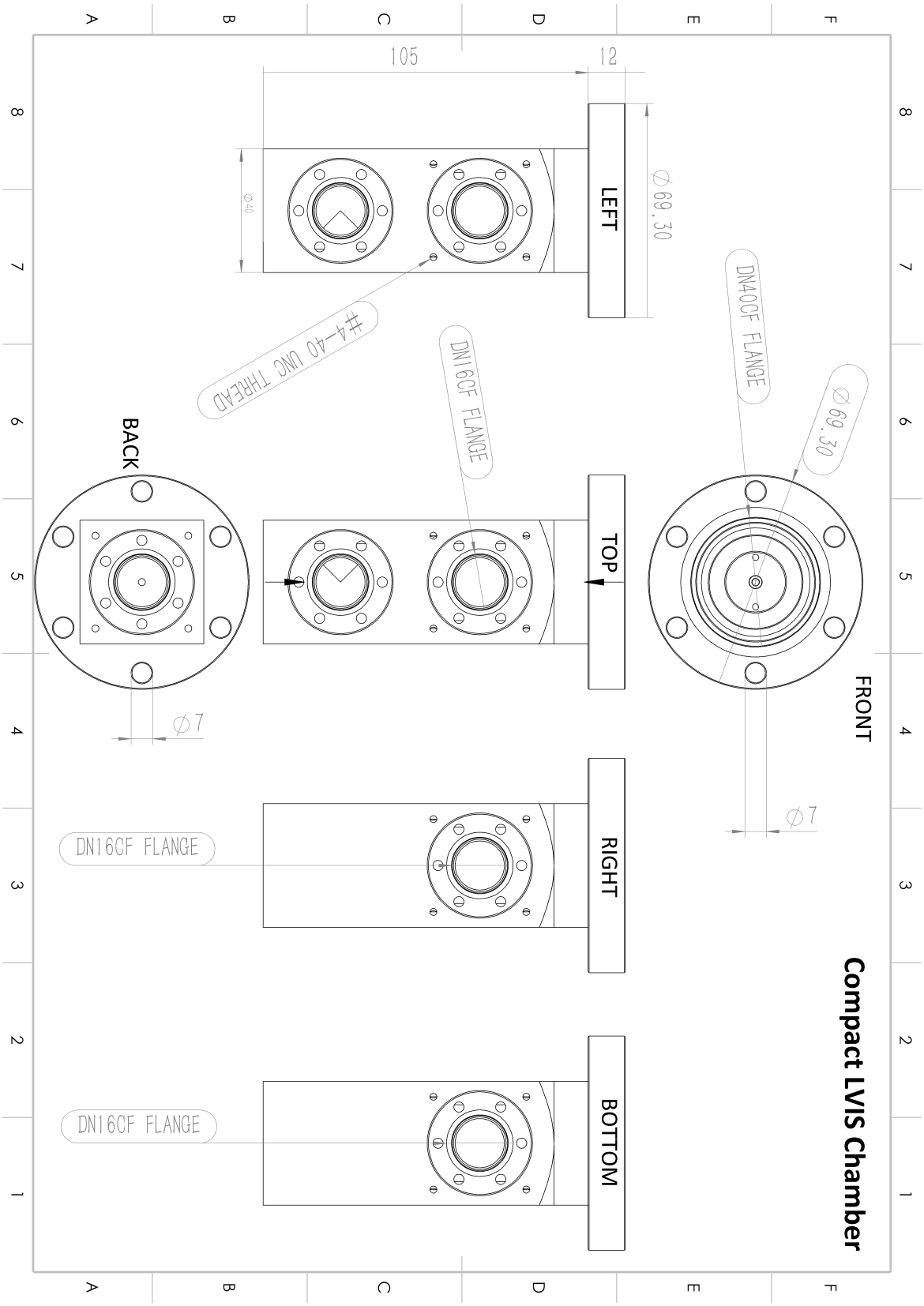

Fig. 10.1 Compact LVIS Technical Drawing 1

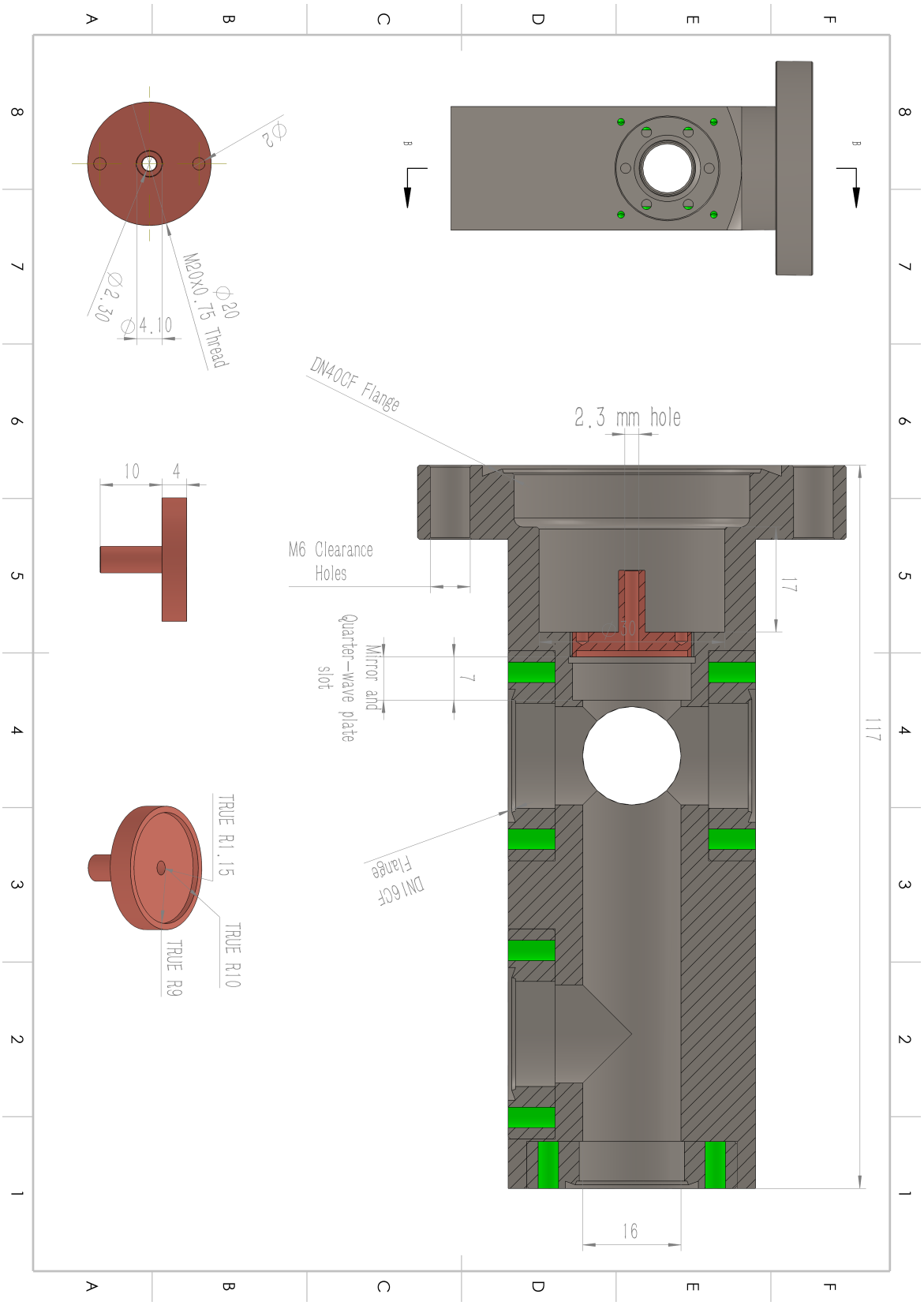

Fig. 10.2 Compact LVIS Technical Drawing 2